University of Alberta

Inverse Design of Turbomachinery Blades

by

Adam Jon Medd ©

A thesis submitted to the Faculty of Graduate Studies and Research in partial fulfillment of the requirements for the degree of Master of Science.

Department of Mechanical Engineering

Edmonton, Alberta
Fall 1998

National Library of Canada
Acquisitions and Bibliographic Services
395 Wellington Street
Ottawa ON K1A 0N4
Canada

Bibliothèque nationale du Canada
Acquisitions et services bibliographiques
395, rue Wellington
Ottawa ON K1A 0N4
Canada

Your file Votre référence

Our file Notre référence

The author has granted a non-exclusive licence allowing the National Library of Canada to reproduce, loan, distribute or sell copies of this thesis in microform, paper or electronic formats.

The author retains ownership of the copyright in this thesis. Neither the thesis nor substantial extracts from it may be printed or otherwise reproduced without the author's permission.

L'auteur a accordé une licence non exclusive permettant à la Bibliothèque nationale du Canada de reproduire, prêter, distribuer ou vendre des copies de cette thèse sous la forme de microfiche/film, de reproduction sur papier ou sur format électronique.

L'auteur conserve la propriété du droit d'auteur qui protège cette thèse. Ni la thèse ni des extraits substantiels de celle-ci ne doivent être imprimés ou autrement reproduits sans son autorisation.

0-612-34391-X

Canada

University of Alberta

Faculty of Graduate Studies and Research

The undersigned certify that they have read, and recommend to the Faculty of Graduate Studies and Research for acceptance, a thesis entitled Inverse Design of Turbomachinery Blades submitted by Adam Jon Medd in partial fulfillment of the requirements for the degree of Master of Science .

Dr. J. W. Yokota (Supervisor)

Dr. Y. S. Wong

Dr. R. W. Toogood

Date 9/10/98

Abstract

With this work, a new Lagrangian based inverse technique for constructing turbomachinery blade geometries is presented. This method, which consists of a 2-D flow field integrator, a camber line generator and a passage averaged momentum/pressure boundary condition, generates a blade geometry in response to a prescribed flow turning distribution.

By describing a blade geometry as a mean camber line with a specified thickness distribution, it is shown how this camber line can be obtained from a Lagrangian analysis that overlays the blade onto a material line that convects from inflow to outflow. This treatment enhances both the global convergence of the calculation and the flow resolution near the leading and trailing edges of the blade. Also, the unsteady form of the pressure boundary condition is derived and is shown to produce convergence acceleration.

Finally, a new unsteady pressure boundary condition is derived from a complex-lamellar decomposition of the flow field, and its passage average flow turning. With this new shock-fitting approach, transonic blades, with strong passage shocks, can be designed that are both geometrically continuous and faithful to the prescribed flow turning distribution.

Dedication

I would like to dedicate this work to my wife Angela and my son Ethan. Thank you for supporting me throughout this work and for enduring the many hours and late nights as well as my anxiety and frustration.

ACKNOWLEDGEMENT

I would like to extend my sincerest thanks to my advisor Dr. Jeffrey W. Yokota. Without his guidance and instruction this work would never have been completed. Over the course of the last two years I've had the pleasure of learning from both his many years of experience as well as his approach to solving new problems. I hope to apply these to all my future endeavors.

I would also like to acknowledge the numerous conversations held throughout the course of this work with Dr. T. Q. Dang and for the use of his inverse design code upon which this work is based.

I would like to thank my parents for giving me the motivation and support to take on such an endeavor. They have always been there when I needed them and were always interested in everything I have done. I would also like to thank the Kenny family for their moral support as well as Sunday dinners that gave me the energy to finish this work.

Special thanks go out to everybody in the CFDAM lab for helping me put this all together. Many technical conversations were held with Seifu Bekele and the atmosphere was always relaxed and informal with Lance Portas, Chris Reaume and Kevin Reid.

Thank you to the faculty and staff of the Mechanical Engineering Department at the University of Alberta for the superb instruction and technical support they have provided me.

I would like to thank Dr. Y. S. Wong and Dr. R. W. Toogood for participating in my defence as committee members.

Finally, I am grateful to the Natural Sciences and Engineering Research Council of Canada for supporting this work under NSERC grant OGP 170377.

CONTENTS

1 Introduction **1**
- 1.1 Background . . . 1
- 1.2 Objectives . . . 3
- 1.3 Outline . . . 3

2 Governing Equations **5**
- 2.1 Camber Line Generator . . . 5
- 2.2 Flow Equations . . . 8
  - 2.2.1 Integral Form . . . 8
  - 2.2.2 Differential Form . . . 9
  - 2.2.3 Cartesian Coordinates . . . 10
- 2.3 System of Equations for Inverse Design . . . 11
- 2.4 Classification of Equations . . . 11
- 2.5 Complex - Lamellar Decomposition . . . 13
- 2.6 Nondimensionalization . . . 16

3 Numerical Approximation **18**
- 3.1 Time Marching Scheme . . . 18
- 3.2 Spatial Discretization . . . 19
  - 3.2.1 Finite Volume Discretization of the Flow Equations . . . 19
  - 3.2.2 Artificial Dissipation . . . 23
  - 3.2.3 Camber Line Generator . . . 24
- 3.3 Numerical Stability Analysis . . . 26
  - 3.3.1 Flow Equations . . . 26
  - 3.3.2 Camber Line Generator . . . 29
- 3.4 Time Stepping . . . 31

3.5 Boundary Conditions 32
3.5.1 Inflow/Outflow Boundaries 32
3.5.2 Periodic Boundaries 34
3.5.3 Blade Surface Boundary Treatment 34
3.5.4 Blade Surface Boundary Treatment: Transonic Flow 54

4 Results **59**
4.1 Effect of Material Camber Line Treatment 59
4.1.1 Subsonic Testcase: Turbine Blade at Mach 0.3 61
4.1.2 Subsonic Testcase: Compressor Blade at Mach 0.5 73
4.1.3 Transonic Testcase: Turbine Blade 84
4.1.4 Supersonic Testcase: Compressor Blade 95
4.2 Unsteady Pressure Treatment 106
4.2.1 Subsonic Testcase: Turbine Blade at Mach 0.5 106
4.3 Transonic Blade Design 118
4.3.1 Original Code 118
4.3.2 Subsonically Designed Blade 125
4.3.3 New Treatment 130

5 Conclusions **136**

List of Figures

2.1 Cascade Notation 6

3.1 Finite Volume Cell 19
3.2 Control Volume Surface 20
3.3 Uniform Square Cell 22
3.4 Growth Factor for Flow Equations with Increasing Courant Number . 28
3.5 Growth Factor for Camber Line Stability 30
3.6 Thickness Distribution Used for Testcases 41
3.7 Turning Distribution Shape for the Leading Edge Loaded Blade . . . 43
3.8 Mach Number and Converged Blade Shape for the Leading Edge Loaded Blade 44
3.9 Turning Distribution Shape for the Symmetrically Loaded Blade . . . 45
3.10 Mach Number and Converged Blade Shape for the Symmetrically Loaded Blade 46
3.11 Turning Distribution Shape for the Trailing Edge Loaded Blade . . . 47
3.12 Mach Number and Converged Blade Shape for the Trailing Edge Loaded Blade 48
3.13 Comparison Between the Turning Distributions Using 121 & 41 Points on the curve 50
3.14 Comparison Between the Thickness Distributions Using 121 & 41 Points on the curve 51
3.15 Comparison of Pressure Side Surface Mach Numbers for 121 & 41 Points of Loading and Thickness Distributions 52
3.16 Detail View of Leading Edge Region 53

4.1 Typical Sheared H-Type Mesh 60
4.2 Specified Turning Distribution for the Mach 0.3 Turbine Blade 63
4.3 Specified Thickness Distribution for the Mach 0.3 Turbine Blade . . . 64
4.4 Converged Blade shape for the Mach 0.3 Turbine Blade 65
4.5 Contours of Mach Number in the Blade Passage 66

4.6 Comparison of the Upstream Grid Lines 67
4.7 Mach Number on Blade Surfaces for the Material Camber Line 68
4.8 Mach Number on Blade Surfaces for the Original Camber Line . . . 69
4.9 Comparison of Surface Mach Number on the Pressure Side 70
4.10 Comparison of Surface Mach Number on the Suction Side 71
4.11 Convergence of Original and Material Camber Line Codes 72
4.12 Specified Turning Distribution for the Mach 0.5 Compressor Blade . . 74
4.13 Specified Thickness Distribution for the Mach 0.5 Compressor Blade . 75
4.14 Converged Blade shape for the Mach 0.5 Compressor Blade 76
4.15 Contours of Mach Number in the Blade Passage 77
4.16 Comparison of the Upstream Grid Lines 78
4.17 Mach Number on Blade Surfaces for the Material Camber Line 79
4.18 Mach Number on Blade Surfaces for the Original Camber Line . . . 80
4.19 Comparison of Surface Mach Number on the Suction Side 81
4.20 Comparison of Surface Mach Number on the Pressure Side 82
4.21 Convergence of Original and Material Camber Line Codes 83
4.22 Specified Turning Distribution for the Transonic Turbine Blade 85
4.23 Specified Thickness Distribution for the Transonic Turbine Blade . . 86
4.24 Converged Blade shape for the Transonic Turbine Blade 87
4.25 Contours of Mach Number in the Blade Passage 88
4.26 Comparison of the Upstream Grid Lines 89
4.27 Mach Number on Blade Surfaces for the Material Camber Line 90
4.28 Mach Number on Blade Surfaces for the Original Camber Line 91
4.29 Comparison of Surface Mach Number on the Pressure Side 92
4.30 Comparison of Surface Mach Number on the Suction Side 93
4.31 Convergence of Original and Material Camber Line Codes 94
4.32 Specified Turning Distribution for the Supersonic Compressor Blade . 96
4.33 Specified Thickness Distribution for the Supersonic Compressor Blade 97
4.34 Converged Blade shape for the Supersonic Compressor Blade 98
4.35 Contours of Mach Number in the Blade Passage 99
4.36 Comparison of the Upstream Grid Lines 100
4.37 Mach Number on Blade Surfaces for the Material Camber Line 101
4.38 Mach Number on Blade Surfaces for the Original Camber Line 102
4.39 Comparison of Surface Mach Number on the Pressure Side 103
4.40 Comparison of Surface Mach Number on the Suction Side 104
4.41 Convergence of Original and Material Camber Line Codes 105
4.42 Specified Turning Distribution for the Mach 0.5 Turbine Blade 108
4.43 Specified Thickness Distribution for the Mach 0.5 Turbine Blade . . . 109
4.44 Converged Blade shape for the Mach 0.5 Turbine Blade 110
4.45 Contours of Mach Number in the Blade Passage 111

4.46 Comparison of the Upstream Grid Lines 112
4.47 Mach Number on Blade Surfaces for the Material Camber Line 113
4.48 Mach Number on Blade Surfaces for the Original Camber Line 114
4.49 Comparison of Surface Mach Number on the Pressure Side 115
4.50 Comparison of Surface Mach Number on the Suction Side 116
4.51 Convergence of Original and Material Camber Line Codes 117
4.52 Specified Turning Distribution for the Transonic Turbine Blade 120
4.53 Converged Blade shape for the Transonic Turbine Blade 121
4.54 Contours of Mach Number in the Blade Passage 122
4.55 Mach Numbers on Blade Surfaces 123
4.56 Actual Turning Distribution Generated by the Transonic Turbine Blade 124
4.57 Converged Blade Generated in Subsonic Flow 126
4.58 Mach Number Contours in the Blade Passage for Transonic Flow . . 127
4.59 Mach Number on Blade Surfaces for the Design in Transonic Flow . . 128
4.60 Actual Turning Distribution Generated from the Blade in Transonic Flow 129
4.61 Turning Distribution Including Model of Shock Velocity Term 131
4.62 Converged Continuous Blade Shape Using Transonic Boundary Condition 132
4.63 Mach Contours in the Blade Passage 133
4.64 Mach Number on Blade Surfaces Using Transonic Boundary Condition 134
4.65 Actual Turning Distribution Generated Using Transonic Boundary Condition 135

CHAPTER 1

INTRODUCTION

1.1 Background

With the increase in the accuracy and efficiency of numerical solutions, they are now being implemented into every aspect of the aerodynamic design process. In fact, while they were once used only for generating postmortem analysis of intermediate designs, numerical methods are now being used for both design optimization and inverse design. With inverse design, the designer specifies the final global result required from the design, and the inverse method can be used to find the blade geometry that produces it.

In Dang's [2] method, upon which this work is based, a compressible finite volume scheme is used to calculate the flow around a blade whose geometry is being inversely designed for a prescribed flow turning. The blade geometry is decomposed into a prescribed thickness distribution and a camber line, whose shape is obtained from a no-flux boundary condition that is updated periodically and applied to the solutions of the finite volume scheme. Finally the flow field obtained from the finite volume scheme, is governed by a pressure boundary condition that uses a passage averaged momentum analysis to couple the pressure distribution to the prescribed flow turning. This method stems from the circulation method developed by Dang [2]

and Hawthorne [1] et. al..

The prescribed flow turning is the important factor that separates this method from other inverse design techniques. This has both physical importance, in that it can be related directly to the work input / extracted in the cascade, as well as ease of specification. The inverse methods used by Tong et.al.[5], Giles et.al.[6], Volpe et.al.[7] and Meauzé [8] require the specification of the blade surface static pressures (or velocity) which limits them to two dimensional flow. The assumption that is made is that the pressure is specified along a streamline. In the case of turbomachinery, there exist complex secondary flows that make it difficult to know the streamline path and hence, the specification of the pressure distributions in 3-D flow becomes a difficult task. In addition to the pressure specification limitation, the Hodograph method used by Sanz[9] is also limited to 2-D because of the transformation to the Hodograph plane. This transformation can not be carried out in 3-D. Due to the nature of this transformation, it is also limited to potential flows and thus cannot be used for strong shock cases. The Hodograph method is very elegant mathematically but the trade off is that it is difficult to implement. The inverse method used by Léonard et.al.[10] requires the specification of the Mach number on the surfaces which limits it to 2-D flow for the same reason as specifying pressure. One other limiting aspect of this method is the compatibility relations that are used. These relations would not be attainable in 3-D. Specification of the flow turning distribution, on the other hand, can be extended to the 3-D case without having to know the path of the streamlines a priori. Another problem associated with the specification of both the upper and lower surface pressure distributions is that the converged blade profile may not be closed at the trailing edge. This closure is guaranteed with Dang's method because the thickness distribution is specified as input.

1.2 Objectives

The objectives of this work are to present a new Lagrangian based inverse design technique for constructing turbomachinery blade geometries. The equations used consist of a 2D flow field integrator, a camber line generator and a passage averaged momentum / pressure boundary condition.

The first main objective is to develop a Lagrangian based unsteady camber line generator. One of the purposes for this is to couple the camber line equation directly to the flow equations so that a similar numerical treatment can be used for the entire system of equations. The other purpose, is to use this technique not only for the camber line of the blade but also for the construction of the upstream and downstream grid boundaries to increase the accuracy at the stagnation points in the flow and also, decrease the calculation time required for the numerical simulation.

The second main objective is to develop a new transonic pressure boundary condition used to impose the prescribed flow turning. The need for this was discovered using Dang's [2] existing inverse technique. The design of a turbine blade in the presence of a strong passage shock, having specified a smooth continuous turning distribution, produces a blade with a discontinuous geometry. A method was needed to include the effects of the shock without knowing the location of the shock a priori.

1.3 Outline

In Chapter 2, a coupled system of inverse design equations is presented. These consist of the unsteady Camber Line Generator and the inviscid, compressible flow equations. Also, a complex-lamellar decomposition is presented to develop a new boundary condition for strong transonic flow.

In Chapter 3, the numerical approximations of the system of inverse equations is discussed. The entire system of equations are discretized, in time, with an explicit

multi-stage time stepping scheme. The flow equations are spatially discretized using a finite volume scheme with blended non-linear second and fourth difference artificial dissipation terms used to capture shocks and prevent odd-even point decoupling. The Camber Line Generator is spatially discretized using central differencing with added, linear dissipation to keep the blade as smooth as possible. The boundary conditions for both the inverse technique and the conventional approach are then presented. For the inverse technique, the equations used to implement the flow turning are the unsteady pressure boundary treatment and the transonic pressure boundary using the complex-lamellar decomposition. Examples of the turning distribution and the converged blade shapes are compared.

In Chapter 4, results are presented to show the advantages of coupling the Camber Line Generator directly to the flow equations, as well as, the material line treatment of the upstream and downstream grid boundaries for all flow regimes. Secondly, a testcase is presented to show the effect of using the unsteady pressure boundary treatment over the steady form. A third set of testcases is presented to show the effect of the transonic pressure boundary condition used on strong passage shock transonic flow.

Finally, conclusions will be drawn in Chapter 5.

CHAPTER 2

GOVERNING EQUATIONS

In the inverse design problem both the flow field and the blade geometry are unknown. A coupled system of equations must be developed to obtain both the blade geometry and the flow field around it. The equations of motion for the fluid, used in this case, are the two dimensional, inviscid compressible flow equations also known as the two dimensional Euler equations. The equation used for the blade geometry is derived by defining the blade to be a material line of the fluid. This ensures satisfying the no - flux boundary condition on a solid surface in a fluid flow.

2.1 Camber Line Generator

The camber line generator is the equation used to solve for the shape of the blade. An airfoil shape can be characterized by two things: the camber line and the thickness. Having specified the blade thickness distribution along the axial chord of the blade (set by structural and manufacturing constraints), the camber line is the single characteristic remaining in completely defining the blade shape.

For axial turbomachinery, the notation chosen to describe the blade geometry is that of Fig. (2.1). The blade surface equations then become

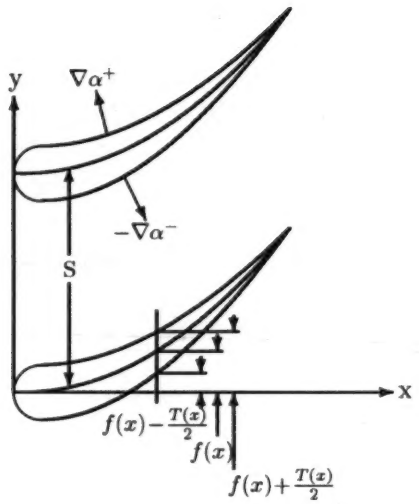

Figure 2.1: Cascade Notation

$$\alpha^+ \equiv y - \left(f(x,t) + \frac{T(x)}{2}\right) \tag{2.1}$$

$$\alpha^- \equiv y - \left(f(x,t) - \frac{T(x)}{2}\right) \tag{2.2}$$

Where α^+ and α^- denote the blade upper and lower surfaces respectively, S is the blade spacing, $f(x,t)$ is the camber line of the blade, $T(x)$ is the specified thickness distribution, x denotes the axial direction and t is time.

The material derivative is used to describe the blade surface as a material surface in the fluid, such that

$$\frac{D\alpha^+}{Dt} = \frac{D\alpha^-}{Dt} = 0$$

The material surface that overlays the upper blade surface takes the following form

$$\frac{D\alpha^+}{Dt} = \frac{\partial \alpha^+}{\partial t} + \vec{V}^+ \cdot \nabla \alpha^+ = 0 \tag{2.3}$$

and similarly for the lower blade surface,

$$\frac{D\alpha^-}{Dt} = \frac{\partial \alpha^-}{\partial t} + \vec{V}^- \cdot \nabla \alpha^- = 0 \tag{2.4}$$

The velocity vector $\vec{V}^+ = \langle u^+, v^+ \rangle$ where u and v are the cartesian velocity components, in the two dimensional case, on the upper blade surface and similarly for $\vec{V}^-$ on the lower blade surface. This differs from the analysis of Dang [2], whereby, only the no-flux condition was satisfied

$$\vec{V}^+ \cdot \nabla \alpha^+ = 0$$

$$\vec{V}^- \cdot \nabla \alpha^- = 0$$

The remainder of the derivation follows the steady analysis of Dang except that the unsteady term is maintained.

By combining the blade surface geometry and the material derivative, the camber line generator can be obtained.

For the upper surface, substitution of Eqn.(2.1) into Eqn.(2.3) yields

$$\frac{\partial}{\partial t}\left[y - \left(f + \frac{T}{2}\right)\right] + \vec{V}^+ \cdot \nabla \left[y - \left(f + \frac{T}{2}\right)\right] = 0$$

$$\frac{\partial}{\partial t}\left[y - \left(f + \frac{T}{2}\right)\right] + u^+ \frac{\partial}{\partial x}\left[y - \left(f + \frac{T}{2}\right)\right] + v^+ \frac{\partial}{\partial y}\left[y - \left(f + \frac{T}{2}\right)\right] = 0$$

Since f and T are functions of only x spatially, this equation becomes

$$-\frac{\partial f}{\partial t} + u^+\left(-\frac{\partial f}{\partial x} - \frac{1}{2}\frac{dT}{dx}\right) + v^+\frac{\partial y}{\partial y} = 0$$

or

$$-\frac{\partial f}{\partial t} - u^+\frac{\partial f}{\partial x} - u^+\frac{1}{2}\frac{dT}{dx} + v^+ = 0$$

The equation for the upper blade surface now takes the form

$$\frac{\partial f}{\partial t} + u^+\frac{\partial f}{\partial x} = -\frac{1}{2}\,u^+\frac{dT}{dx} + v^+ \tag{2.5}$$

Following a similar procedure for the lower blade surface

$$\frac{\partial f}{\partial t} + u^-\frac{\partial f}{\partial x} = +\frac{1}{2}\,u^-\frac{dT}{dx} + v^- \tag{2.6}$$

By adding Eqns.(2.5) and (2.6) the camber line generator is obtained

$$\frac{\partial f}{\partial t} + \frac{(u^+ + u^-)}{2}\frac{\partial f}{\partial x} = -\frac{(u^+ - u^-)}{4}\frac{dT}{dx} + \frac{(v^+ + v^-)}{2} \tag{2.7}$$

One of the advantages that this form of the equation has over Dang's steady form is, that this can now be coupled directly to the flow equations. With this direct coupling, all of the equations can be solved in a similar manner. The details of the differences in numerical implementation, between the two methods, will be made clear in Chapter 3, Section 3.2.3. The advantages in using this formulation will be shown and discussed in Chapter 4.

2.2 Flow Equations

2.2.1 Integral Form

The conservation of mass, momentum and energy are the equations that govern an inviscid, compressible fluid and are written, respectively, in integral form for a control

volume $\forall$ as follows:

$$\frac{\partial}{\partial t}\iiint_{\forall} \rho \, d\forall + \int_{\sigma} \rho \, \vec{V} \cdot \vec{n} \, d\sigma = 0$$

$$\frac{\partial}{\partial t}\iiint_{\forall} \vec{V} \, \rho \, d\forall + \int_{\sigma} \vec{V} \, \rho \, \vec{V} \cdot \vec{n} \, d\sigma + \int_{\sigma} P \, \vec{n} \, d\sigma = 0 \tag{2.8}$$

$$\frac{\partial}{\partial t}\iiint_{\forall} e_t \, d\forall + \int_{\sigma} e_t \, \vec{V} \cdot \vec{n} \, d\sigma + \int_{\sigma} P \, \vec{V} \cdot \vec{n} \, d\sigma = 0$$

These equations are integrated over the control volume $\forall$ bounded by the surface σ. The unit vector $\vec{n}$ acts outward normal to $d\sigma$ which is a small element of the surface σ. The variable ρ is the density, $\vec{V}$ is the velocity vector of the fluid, P is the pressure and $e_t = \rho\Upsilon + \rho\frac{\vec{V}.\vec{V}}{2}$ is the total energy of the fluid, with Υ as the internal energy.

2.2.2 Differential Form

Making use of the divergence theorem on the integral form of the equations (Eqn. 2.8), the surface integrals can be transformed to volume integrals and the differential form of the equations can be obtained.

$$\frac{\partial \rho}{\partial t} + \nabla \cdot (\rho \, \vec{V}) = 0$$

$$\frac{D\vec{V}}{Dt} = -\frac{1}{\rho}\nabla P \tag{2.9}$$

$$\frac{\partial}{\partial t}(e_t) + \nabla \cdot (e_t \vec{V}) = -P\nabla \cdot \vec{V}$$

An alternate form of the equations can be obtained from the Reynolds Transport Theorem and is expressed using index notation

$$\frac{D}{Dt}(\rho J) = 0$$

$$\frac{D}{Dt}(\rho u_i J) = -J\frac{\partial P}{\partial x_i} \tag{2.10}$$

$$\frac{D}{Dt}(e_t J) = -J\frac{\partial}{\partial x_i}(P u_i)$$

where J is the Jacobian matrix of transformation between Eulerian and Lagrangian coordinate systems.

2.2.3 Cartesian Coordinates

The differential forms of the equations of motion Eqn.(2.9) can be expressed in the two dimensional cartesian coordinate system. The following system of first order partial differential equations is the result,

$$\frac{\partial \vec{w}}{\partial t} + \frac{\partial \vec{E}}{\partial x} + \frac{\partial \vec{F}}{\partial y} = 0 \tag{2.11}$$

Where:

$$\vec{w} = \begin{Bmatrix} \rho \\ \rho u \\ \rho v \\ e_t \end{Bmatrix} \qquad \vec{E} = \begin{Bmatrix} \rho u \\ \rho u^2 + P \\ \rho uv \\ (e_t + P)u \end{Bmatrix} \qquad \vec{F} = \begin{Bmatrix} \rho v \\ \rho uv \\ \rho v^2 + P \\ (e_t + P)v \end{Bmatrix}$$

The vector $\vec{w}$ is the conservative variable vector, the vectors $\vec{E}$ and $\vec{F}$ are the flux vectors, ρ is the density, u and v are the cartesian components of velocity in the x and y directions respectively, P is the pressure and e_t is the total energy of the fluid.

2.3 System of Equations for Inverse Design

The integral form of the equations Eqn.(2.8) can be represented in the two dimensional cartesian coordinate system as

$$\int_{\forall} \frac{\partial \vec{w}}{\partial t} d\forall + \oint_{\sigma} \left(\vec{E} n_x + \vec{F} n_y \right) \, d\sigma = 0 \tag{2.12}$$

Where n_x and n_y denote the x and y components of the unit vector normal to the surface and

$$\vec{w} = \begin{Bmatrix} \rho \\ \rho u \\ \rho v \\ e_t \end{Bmatrix} \qquad \vec{E} = \begin{Bmatrix} \rho u \\ \rho u^2 + P \\ \rho uv \\ (e_t + P)u \end{Bmatrix} \qquad \vec{F} = \begin{Bmatrix} \rho v \\ \rho uv \\ \rho v^2 + P \\ (e_t + P)v \end{Bmatrix}$$

For closure, the pressure and total energy of a calorically perfect gas are related through the equation of state:

$$P = (\gamma - 1) \left(e_t - \rho \frac{\vec{V} \cdot \vec{V}}{2} \right) \tag{2.13}$$

where $\gamma = 1.4$ is the ratio of specific heat capacities for air.

These equations, coupled directly to the camber line generator (Eqn. 2.7 of Section 2.1), combine to make the system of equations needed for the solution of the inverse problem.

2.4 Classification of Equations

By rewriting the equations of motion in quasi - linear form as follows

$$\frac{\partial \vec{w}}{\partial t} + \overline{\overline{A}}_x \frac{\partial \vec{w}}{\partial x} + \overline{\overline{A}}_y \frac{\partial \vec{w}}{\partial y} = 0 \tag{2.14}$$

Where:

$$\overline{\overline{A}}_x \equiv \frac{\partial \vec{E}}{\partial \vec{w}} = \begin{bmatrix} 0 & 1 & 0 & 0 \\ \frac{\gamma-3}{2}u^2 + \frac{\gamma-1}{2}v^2 & (3-\gamma)u & -(\gamma-1)v & \gamma-1 \\ -uv & v & u & 0 \\ -\gamma u\frac{e_t}{\rho} + (\gamma-1)u|\vec{V}|^2 & \gamma\frac{e_t}{\rho} - \frac{\gamma-1}{2}(v^2+3u^2) & -(\gamma-1)uv & \gamma u \end{bmatrix}$$

$$\overline{\overline{A}}_y \equiv \frac{\partial \vec{F}}{\partial \vec{w}} = \begin{bmatrix} 0 & 0 & 1 & 0 \\ -uv & v & u & 0 \\ \frac{\gamma-3}{2}v^2 + \frac{\gamma-1}{2}u^2 & -(\gamma-1)u & (3-\gamma)v & \gamma-1 \\ -\gamma v\frac{e_t}{\rho} + (\gamma-1)v|\vec{V}|^2 & -(\gamma-1)uv & \gamma\frac{e_t}{\rho} - \frac{\gamma-1}{2}(u^2+3v^2) & \gamma v \end{bmatrix}$$

it is possible to classify this system of equations.

The eigenvalues of the two matrices $\overline{\overline{A}}_x$ and $\overline{\overline{A}}_y$ define the behavior of the solution to the Euler equations. If the eigenvalues of the matrices are all real, the system of equations is said to be hyperbolic. The eigenvalues are obtained as solutions of the equations

$$det\left|\lambda_x\overline{\overline{I}} - \overline{\overline{A}}_x\right| = 0 \quad , \quad det\left|\lambda_y\overline{\overline{I}} - \overline{\overline{A}}_y\right| = 0 \tag{2.15}$$

Where λ_x and λ_y are the eigenvalues of $\overline{\overline{A}}_x$ and $\overline{\overline{A}}_y$ respectively and $\overline{\overline{I}}$ is the identity matrix.

The eigenvalues of the matrices $\overline{\overline{A}}_x$ and $\overline{\overline{A}}_y$ can be shown to be

$$\begin{aligned} \lambda_{x_1} = \lambda_{x_2} = u \qquad & \lambda_{y_1} = \lambda_{y_2} = v \\ \lambda_{x_3} = u + c \qquad & \lambda_{y_3} = v + c \\ \lambda_{x_4} = u - c \qquad & \lambda_{y_4} = v - c \end{aligned}$$

where c is the speed of sound and is defined by $c = \sqrt{\gamma RT}$.

Advantage is taken of the hyperbolic nature of these equations when constructing the camber line of the blade. Restating the camber line generator (Eqn. 2.7)

$$\frac{\partial f}{\partial t} + \frac{(u^+ + u^-)}{2}\frac{\partial f}{\partial x} = -\frac{(u^+ - u^-)}{4}\frac{dT}{dx} + \frac{(v^+ + v^-)}{2}$$

In the upstream and downstream regions from the blade, the thickness $T = 0$ so the above equation takes the form

$$\frac{\partial f}{\partial t} + \frac{(u^+ + u^-)}{2}\frac{\partial f}{\partial x} = \frac{(v^+ + v^-)}{2} \qquad (2.16)$$

This equation can now be used to construct a material surface in the upstream and downstream regions of the flow field. In essence, a massless particle is allowed to convect from the inlet of the domain to the leading edge of the blade, its path then defines the material surface in that region. The blade is then constructed using Eqn.(2.7) until the trailing edge of the blade is reached, then Eqn.(2.16) can be used to convect the particle from the trailing edge to the outflow boundary and its path defines the material surface in the downstream region of the flow. This entire surface, from inflow to outflow is used as the upper and lower boundary of the domain.

2.5 Complex - Lamellar Decomposition

The derivation of this decomposition is needed in order to develop a modified boundary condition in a later section. This decomposition is similar to the one by Goldstein [13].

Restating the linear momentum equation of Eqn.(2.10)

$$\frac{D}{Dt}(\rho u_i J) = -J\frac{\partial P}{\partial x_i} \qquad (2.17)$$

and following the analysis of Yokota [14],[15] by multiplying it by the Cartesian/Lagrangian transformation matrix $\frac{\partial x_i}{\partial X_j}$ the equation becomes

$$\frac{\partial x_i}{\partial X_j}\frac{D}{Dt}\{\rho u_i J\} = -J\frac{\partial x_i}{\partial X_j}\frac{\partial P}{\partial x_i} \qquad (2.18)$$

Which can be manipulated using the chain rule to obtain

$$\frac{D}{Dt}\left\{\rho u_i J \frac{\partial x_i}{\partial X_j}\right\} - \rho u_i J \frac{D}{Dt}\left\{\frac{\partial x_i}{\partial X_j}\right\} = -J\frac{\partial P}{\partial X_j} \tag{2.19}$$

The order of differentiation in the second term can be changed to give

$$\frac{D}{Dt}\left\{\rho u_i J \frac{\partial x_i}{\partial X_j}\right\} - \rho u_i J \frac{\partial}{\partial X_j}\left\{\frac{Dx_i}{Dt}\right\} = -J\frac{\partial P}{\partial X_j} \tag{2.20}$$

Since $\frac{Dx_i}{Dt} = u_i$ and using the chain rule again, the equation becomes

$$\frac{D}{Dt}\left\{\rho u_i J \frac{\partial x_i}{\partial X_j}\right\} - \rho J \frac{\partial}{\partial X_j}\left\{\frac{u_i u_i}{2}\right\} = -J\frac{\partial P}{\partial X_j} \tag{2.21}$$

As the next step in isolating u_i, this can then be integrated in time

$$\int \frac{D}{Dt}\left\{\rho u_i J \frac{\partial x_i}{\partial X_j}\right\} dt - \int \rho J \frac{\partial}{\partial X_j}\left\{\frac{u_i u_i}{2}\right\} dt = -\int J\frac{\partial P}{\partial X_j}\, dt \tag{2.22}$$

and expanding the second term using integration by parts and incorporating the continuity equation of Eqn.(2.10)

$$\rho u_i J \frac{\partial x_i}{\partial X_j} - a_j - \rho J \int \frac{\partial}{\partial X_j}\left\{\frac{u_i u_i}{2}\right\} dt = -\int J\frac{\partial P}{\partial X_j}\, dt \tag{2.23}$$

where a_j is a vector constant of integration dependent on the material coordinates (X, Y). The derivative can be pulled out of the integral in the third term to give

$$\rho u_i J \frac{\partial x_i}{\partial X_j} - a_j - \rho J \frac{\partial}{\partial X_j}\left\{\int \frac{u_i u_i}{2} dt\right\} = -\int J\frac{\partial P}{\partial X_j}\, dt \tag{2.24}$$

The equation can now be divided by ρJ

$$u_i \frac{\partial x_i}{\partial X_j} - A_j = \frac{\partial}{\partial X_j}\left\{\int \frac{u_i u_i}{2} dt\right\} - \frac{1}{\rho J}\int J\frac{\partial P}{\partial X_j}\, dt \tag{2.25}$$

where A_j, is again, a constant of integration such that $\frac{D}{Dt}(A_j) = 0$. Since the combination, ρJ, is a material quantity, the equation becomes

$$u_i \frac{\partial x_i}{\partial X_j} - A_j = \frac{\partial}{\partial X_j}\left\{\int \frac{u_i u_i}{2} dt\right\} - \int \frac{J}{\rho J}\frac{\partial P}{\partial X_j}\, dt \tag{2.26}$$

leading to

$$u_i \frac{\partial x_i}{\partial X_j} - A_j = \frac{\partial}{\partial X_j} \left\{ \int \frac{u_i u_i}{2} dt \right\} - \int \frac{1}{\rho} \frac{\partial P}{\partial X_j} \, dt \tag{2.27}$$

An expression is now needed for $\frac{1}{\rho}\frac{\partial P}{\partial X_j}$. By combining the first and second laws of thermodynamics

First Law

$$de = \partial q - P \, d\left(\frac{1}{\rho}\right) \tag{2.28}$$

where e is the total energy of the fluid, q is the heat of the system, P is pressure and ρ is density.

Second Law

$$\Theta ds = \partial q \tag{2.29}$$

where Θ is temperature and s is entropy.

Also from the definition of enthalpy $h = \Upsilon + \frac{P}{\rho}$ the expression can be found as

$$\frac{1}{\rho} dP = dh - \Theta ds \tag{2.30}$$

Substitution of this equation into Eqn.(2.27) gives the form

$$u_i \frac{\partial x_i}{\partial X_j} - A_j = \frac{\partial}{\partial X_j} \int \frac{u_i u_i}{2} \, dt - \int \left\{ \frac{\partial h}{\partial X_j} - \Theta \frac{\partial s}{\partial X_j} \right\} dt \tag{2.31}$$

The terms can be collected and represented as

$$u_i \frac{\partial x_i}{\partial X_j} - A_j = \frac{\partial}{\partial X_j} \int \left\{ \frac{u_i u_i}{2} - h \right\} \, dt + \int \Theta \frac{\partial s}{\partial X_j} dt \tag{2.32}$$

By defining the following Weber Transformations

$$\frac{D\phi}{Dt} = \frac{u_i u_i}{2} - h$$

$$\frac{D\eta}{Dt} = \Theta$$

Eqn.(2.32) can be rewritten as

$$u_i \frac{\partial x_i}{\partial X_j} = A_j + \frac{\partial \phi}{\partial X_j} + \int \frac{D\eta}{Dt} \frac{\partial s}{\partial X_j} dt \tag{2.33}$$

The last term can be expanded using the chain rule to give

$$u_i \frac{\partial x_i}{\partial X_j} = A_j + \frac{\partial \phi}{\partial X_j} + \int \left\{ \frac{D}{Dt}\left(\eta \frac{\partial s}{\partial X_j}\right) - \eta \frac{D}{Dt}\left(\frac{\partial s}{\partial X_j}\right) \right\} dt \tag{2.34}$$

which can be represented, by exchanging the order of differentiation on the last term, as

$$u_i \frac{\partial x_i}{\partial X_j} = A_j + \frac{\partial \phi}{\partial X_j} + \int \frac{D}{Dt}\left(\eta \frac{\partial s}{\partial X_j}\right) dt - \int \eta \frac{\partial}{\partial X_j}\left(\frac{Ds}{Dt}\right) dt \tag{2.35}$$

Then Eqn.(2.35), which, when multiplied by $\frac{\partial x_i}{\partial X_j}$ to isolate u_i and given that an inviscid, nonconducting fluid implies

$$\frac{Ds}{Dt} = 0$$

becomes the complex-lamellar decomposition

$$u_i = \frac{\partial \phi}{\partial x_i} + A_j \frac{\partial X_j}{\partial x_i} + \eta \frac{\partial s}{\partial x_i} \tag{2.36}$$

It is this form of the equation that will be used to construct a new boundary condition for transonic turbine blades. The reason this is needed will be discussed in a later section.

2.6 Nondimensionalization

The non-dimensional form of the equations can be obtained by using the dimensional variables

P_o = upstream stagnation pressure
T_o = upstream stagnation temperature
R = universal gas constant
C = axial chord length

to non-dimensionalize the variables

$$\overline{x} = \frac{x}{C} \qquad \overline{y} = \frac{y}{C}$$

$$\overline{u} = \frac{u}{\sqrt{RT_o}} \qquad \overline{v} = \frac{v}{\sqrt{RT_o}}$$

$$\overline{P} = \frac{P}{P_o} \qquad \overline{\rho} = \frac{\rho RT_o}{P_o}$$

Substitution of these nondimensional variables into the inverse design equations results in a set of equations that look identical to the dimensional form of the equations (Eqn.(2.12) and Eqn.(2.7)) .

CHAPTER 3

NUMERICAL APPROXIMATION

3.1 Time Marching Scheme

The multi-stage scheme of Jameson et.al. [11] is used to converge the solution to steady state. Being an explicit scheme, the solution is known at the current time level N, and is used to advance the solution by Δt to give the solution at time $N+1$. Defining the vector

$$\vec{W} = \left\{ \begin{array}{c} \forall\, \vec{w} \\ f \end{array} \right\} \tag{3.1}$$

Where $\forall$ is the cell volume, $\vec{w}$ is the conservative variable vector and f the camber line. The following 4 - stage scheme is used to advance the inverse design equations in time with time step Δt

$$\begin{aligned} \vec{W}^{(0)} &= \vec{W}^{N} \\ \vec{W}^{(1)} &= \vec{W}^{N} - \alpha_1\, \Delta t\, \vec{R}(\vec{W}^{(0)}) \\ \vec{W}^{(2)} &= \vec{W}^{N} - \alpha_2\, \Delta t\, \vec{R}(\vec{W}^{(1)}) \\ \vec{W}^{(3)} &= \vec{W}^{N} - \alpha_3\, \Delta t\, \vec{R}(\vec{W}^{(2)}) \\ \vec{W}^{(4)} &= \vec{W}^{N} - \alpha_4\, \Delta t\, \vec{R}(\vec{W}^{(3)}) \\ \vec{W}^{N+1} &= \vec{W}^{(4)} \end{aligned} \tag{3.2}$$

Where the residual is defined as

$$\vec{R} = \begin{pmatrix} \forall \frac{\partial \vec{w}}{\partial t} \\ \frac{\partial f}{\partial t} \end{pmatrix} = \begin{pmatrix} -\oint (E\vec{n}_x + F\vec{n}_y) \\ -\frac{(u^+ + u^-)}{2}\frac{\partial f}{\partial x} - \frac{(u^+ - u^-)}{4}\frac{\partial T}{\partial x} + \frac{(v^+ + v^-)}{2} \end{pmatrix} \tag{3.3}$$

The stage coefficients (α) are set for both time accuracy and convergence acceleration. The stage coefficients $\alpha_3 = \frac{1}{2}$ and $\alpha_4 = 1$ are used to maintain second order time accuracy and the remaining two coefficients, $\alpha_1 = \frac{1}{4}$ and $\alpha_2 = \frac{1}{3}$, are used for convergence acceleration.

3.2 Spatial Discretization

3.2.1 Finite Volume Discretization of the Flow Equations

The spatial discretization formulation used for the flow equations is the finite volume scheme. In using this scheme the entire domain is divided up into small control volumes (or cells) and the integral equations are applied to each cell. Both the volume integral and the surface integral of Eqn. 2.12 contain spatial terms and require attention here. Consider the following quadrilateral control volume (i, j)

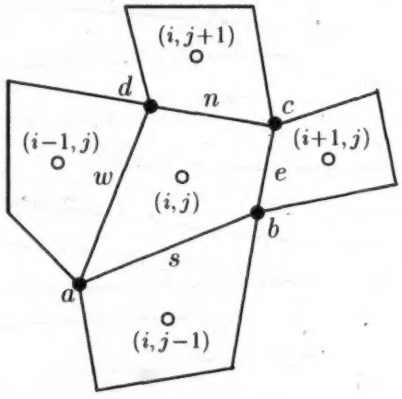

Figure 3.1: Finite Volume Cell

Where the indices i and j label the cell centers of the neighbouring cells, n, w, s, e are the faces of the cell (i, j) and a, b, c, d are the cell vertex. The mean value theorem is used to approximate the value of the solution at the cell center (i, j). Since the variable is approximated to have no variation within the cell, the volume integral of Eqn.(2.12) becomes

$$\int_{\forall} \frac{\partial \vec{w}}{\partial t}\, d\forall \approx \frac{\partial \vec{w}}{\partial t}\, \Delta\forall$$

Where $\forall$ is the volume of a cell with unit depth and is calculated as follows

$$\Delta\forall = \frac{1}{2}|\Delta x_{ac}\, \Delta y_{bd} - \Delta x_{bd}\, \Delta y_{ac}|$$

Consider the following control surface element s from Fig.(3.1)

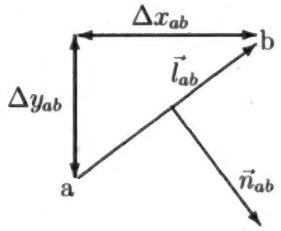

Figure 3.2: Control Volume Surface

Where:

$$\Delta x_{ab} \equiv x_b - x_a$$
$$\Delta y_{ab} \equiv y_b - y_a$$

and $\vec{l}_{ab}$ is the length vector of the control volume face ab defined as

$$\vec{l}_{ab} = (\Delta x_{ab})\vec{e}_x + (\Delta y_{ab})\vec{e}_y$$

By satisfying the conditions $\vec{n}_{ab} \cdot \vec{l}_{ab} = 0$ and $|\vec{n}_{ab}| = |\vec{l}_{ab}|$, the outward normal vector

$\vec{n}_{ab}$ can be shown to be

$$\vec{n}_{ab} = (\Delta y_{ab})\vec{e}_x + (-\Delta x_{ab})\vec{e}_y$$

The values of E and F are now required on each face of the cell in order to evaluate the surface integral. There are two approximations made to obtain these surface fluxes. First the mean value theorem is used to approximate the variation of the fluxes, along the faces, as the average value at the center of the face. Second, since only the cell centered values are known, the mean value on the face must be approximated by an interpolation scheme using the cell centered values in the neighbouring cells.

This approximation states that the face values are constant along the length of the face and the integral can be written as

$$\oint_{\sigma} (E\vec{n}_x + F\vec{n}_y)\, d\sigma \approx \sum_{m=1}^{M} (E_m\, \Delta y_m - F_m\, \Delta x_m)$$

with M as the number of faces on the cell.

For a quadrilateral element

$$\begin{aligned} \sum_{faces} (E_m\, \Delta y_m - F_m\, \Delta x_m) &= (E_s\, \Delta y_s - F_s\, \Delta x_s) \\ &+ (E_e\, \Delta y_e - F_e\, \Delta x_e) \\ &+ (E_n\, \Delta y_n - F_n\, \Delta x_n) \\ &+ (E_w\, \Delta y_w - F_w\, \Delta x_w) \end{aligned} \tag{3.4}$$

Using linear interpolation of the cell - centered solution to approximate the face values as follows:

$$E_e = E_{i+\frac{1}{2},j} = \frac{1}{2}(E_{i+1,j} + E_{i,j}) \tag{3.5}$$

$$F_e = F_{i+\frac{1}{2},j} = \frac{1}{2}(F_{i+1,j} + F_{i,j}) \tag{3.6}$$

for the east face of the cell, and similarly for the remaining faces.

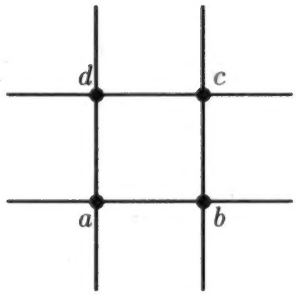

Figure 3.3: Uniform Square Cell

Applying Eqn.(3.4) to the uniform square grid of Fig.(3.3), the finite volume discretization can be reduced to

$$\vec{R} = \frac{(E_e - E_w)\Delta y}{\Delta x \Delta y} + \frac{(F_n - F_s)\Delta x}{\Delta x \Delta y} \tag{3.7}$$

since,

$$\Delta x = x_b - x_a = -(x_d - x_c)$$

$$\Delta y = y_c - y_b = -(y_a - y_d)$$

Substitution of Eqns.(3.5) and (3.6) into Eqn.(3.7) reduces the equation to the following central finite difference approximation

$$\vec{R} = \frac{E_{i+1,j} - E_{i-1,j}}{2\Delta x} + \frac{F_{i,j+1} - F_{i,j-1}}{2\Delta y} \tag{3.8}$$

Substitution of the following Taylor series expansions for $E_{i+1,j}$ and $E_{i-1,j}$

$$E_{i+1,j} = E_{i,j} + \Delta x \frac{\partial E}{\partial x} + \frac{\Delta x^2}{2}\frac{\partial^2 E}{\partial x^2} + \frac{\Delta x^3}{6}\frac{\partial^3 E}{\partial x^3}$$

$$E_{i-1,j} = E_{i,j} - \Delta x \frac{\partial E}{\partial x} + \frac{\Delta x^2}{2}\frac{\partial^2 E}{\partial x^2} - \frac{\Delta x^3}{6}\frac{\partial^3 E}{\partial x^3}$$

and similar equations for $F_{i,j+1}$ and $F_{i,j-1}$, into Eqn.(3.8) gives the residual of the exact equation plus truncation terms

$$\vec{R} = \frac{\partial E}{\partial x} + \frac{\partial F}{\partial y} + \frac{\Delta x^2}{6}\frac{\partial^3 E}{\partial x^3} + \frac{\Delta y^2}{6}\frac{\partial^3 F}{\partial y^3} \tag{3.9}$$

The leading truncation terms are shown and are of order $O(\Delta x^2, \Delta y^2)$. Therefore, the finite volume discretization reduces to a central finite difference approximation on a uniform square grid, which gives second order accuracy spatially.

3.2.2 Artificial Dissipation

Since the finite volume scheme reduces to central differences on a uniform grid, the addition of artificial dissipation is required to prevent odd - even point decoupling and shock overshoots. To maintain the conservative form of the equations, the dissipation is added as follows, suggested by Jameson et. al. [11]

$$\int \frac{\partial \vec{w}}{\partial t} + \oint (Q\vec{w} + D\vec{w}) = 0 \tag{3.10}$$

Where Q is the spatial operator of the original equation and $D = d_\xi + d_\eta$ is the artificial dissipation. A combination of non-linear second and fourth differences are added in the grid directions (ξ, η), for convenience, and are used as follows

$$d_\xi = \left(\varepsilon_\xi^{(2)} \, |\lambda_\xi|_{max} \, \Delta\xi \, \frac{\partial \vec{w}}{\partial \xi} - \varepsilon_\xi^{(4)} \, |\lambda_\xi|_{max} \, \Delta\xi^3 \, \frac{\partial^3 \vec{w}}{\partial \xi^3} \right) \tag{3.11}$$

$$d_\eta = \left(\varepsilon_\eta^{(2)} \, |\lambda_\eta|_{max} \, \Delta\eta \, \frac{\partial \vec{w}}{\partial \eta} - \varepsilon_\eta^{(4)} \, |\lambda_\eta|_{max} \, \Delta\eta^3 \, \frac{\partial^3 \vec{w}}{\partial \eta^3} \right) \tag{3.12}$$

where $|\lambda|_{max}$ is taken to be the maximum eigenvalue of the Euler equations in that cell

$$|\lambda_\xi|_{max} = |V_\xi| + |c_1| \, , \quad |\lambda_\eta|_{max} = |V_\eta| + |c_2| \tag{3.13}$$

The velocities V_ξ and V_η are the velocities normal to the cell faces and c_1 and c_2 are the local speed of sound on the faces. The terms $\varepsilon_\xi^{(2)}$ and $\varepsilon_\xi^{(4)}$ are now defined as

$$\left(\varepsilon_\xi^{(2)}\right)_{i+\frac{1}{2},j} = \kappa^{(2)} \, max \, \left[(\nu_\xi)_{i,j} \, , \, (\nu_\xi)_{i+1,j}\right] \, , \quad \left(\varepsilon_\xi^{(4)}\right)_{i+\frac{1}{2},j} = max \left[0 \, , \, \kappa^{(4)} - \left(\varepsilon_\xi^{(2)}\right)_{i+\frac{1}{2},j} \right] \tag{3.14}$$

and are used to add the second difference term near shocks to prevent shock overshoots and remove the fourth difference terms that can be destabilizing in that region. The values for $\kappa^{(2)}, \kappa^{(4)}$, as recommended by Dang [2] , are

$$\kappa^{(2)} = \frac{1}{2} \ , \ \kappa^{(4)} = \frac{1}{128}$$

The shocked region is found using the following switching function ν_ξ

$$(\nu_\xi)_{i,j} = \frac{|P_{i+1,j} - 2P_{i,j} + P_{i-1,j}|}{|P_{i+1,j}| + 2|P_{i,j}| + |P_{i-1,j}|} \tag{3.15}$$

which is based on the local pressure gradient.

In the region of low pressure gradient, only the fourth difference term will be used to prevent odd - even point decoupling which will maintain the second order accuracy of the finite volume scheme. In a region of high pressure gradient (a shock wave for example) the fourth difference is turned off and only the lower order second difference is used to capture the shock by preventing overshoots.

3.2.3 Camber Line Generator

Since the equation is marched in time using the 4-stage Runge-Kutta method of Section 3.1 only the discussion of discretizing the remaining residual of Eqn.(3.3) remains. With the spatial operator δ_x, the camber line generator becomes

$$\frac{df}{dt} = -\frac{(u_i^+ + u_i^-)}{2}\frac{\delta_x f}{\Delta x} - \frac{(u_i^+ - u_i^-)}{4}\frac{\delta_x T}{\Delta x} + \frac{(v_i^+ + v_i^-)}{2} \tag{3.16}$$

Using the central difference formulation the camber line and the thickness terms are represented by

$$\frac{\delta_x f}{\Delta x} = \frac{f_{i+1} - f_{i-1}}{x_{i+1} - x_{i-1}}$$

$$\frac{\delta_x T}{\Delta x} = \frac{T_{i+1} - T_{i-1}}{x_{i+1} - x_{i-1}}$$

This discretization along with the addition of a linear, second difference artificial dissipation term, reduces the method to a first order upwind scheme which keeps the camber line as smooth as possible.

Discretization of the surface velocities is done in the following manner

$$u_i^+ = \frac{1}{2}\left(u^i_{camb} + u_{i,j=2}\right) \tag{3.17}$$

$$u_i^- = \frac{1}{2}\left(u^i_{camb} + u_{i,j=my}\right) \tag{3.18}$$

$$u^i_{camb} = \frac{1}{2}\left(u_{i,j=2} + u_{i,j=my}\right) \tag{3.19}$$

and similarly for v^+ and v^-. The velocities $u_{i,j=2}$ and $u_{i,j=my}$ refer to the cell centered value in the cells adjacent to the upper and lower blade surfaces respectively.

There are several differences between this new formulation of the camber line generator and the original formulation proposed by Dang. The first of these, being the treatment of the camber line generator in the transient portion of the calculation. The original approach was to update the camber line every 2 - 5 iterations of the flow field. A relaxation factor of between 0.2 and 0.5 was used to damp the predicted values for stability. With this new approach, the camber line generator is coupled directly to the flow equations eliminating the need to specify how often the camber line is updated. Also, the relaxation method is no longer used, instead, stability is governed by the Courant number limit obtained using Von Neumann stability analysis.

The last major difference is the spatial discretization technique. The original approach used a zeroth order extrapolation of the cell centered velocities to the blade surfaces. Using this approximation the steady form of the camber line generator from Eqn.(3.16) took on the form

$$\frac{(u_{i,j=2} + u_{i,j=my})}{2}\frac{\delta_x f}{\Delta x} = -\frac{(u_{i,j=2} - u_{i,j=my})}{4}\frac{\delta_x T}{\Delta x} + \frac{(v_{i,j=2} + v_{i,j=my})}{2} \tag{3.20}$$

The current method is to use Eqns.(3.17), (3.18) and (3.19) for the blade surface velocities. For comparison purposes only, these can be substituted into the steady

form of Eqn.(3.16) to give

$$\frac{(u_{i,j=2} + u_{i,j=my})}{2} \frac{\delta_x f}{\Delta x} = -\frac{(u_{i,j=2} - u_{i,j=my})}{8} \frac{\delta_x T}{\Delta x} + \frac{(v_{i,j=2} + v_{i,j=my})}{2} \tag{3.21}$$

Using this method, the approximation maintains the second order accuracy of the finite volume scheme on a uniform grid.

3.3 Numerical Stability Analysis

3.3.1 Flow Equations

The method chosen for the stability analysis of the flow equations is the Von Neumann method. This method is used for linear, constant coefficient equations so, the following model hyperbolic equation, representative of the flow equations, will be used

$$u_t + c u_x = k\,\Delta x^3\, u_{xxxx} \tag{3.22}$$

The model equation is spatially discretized using central differences and $k = k_4\, c$ to give

$$\frac{\partial \overline{u}_i}{\partial t} = -\frac{c}{2\Delta x}\left(\overline{u}^N_{i+1} - \overline{u}^N_{i-1}\right) + \frac{k_4\, c\, \Delta x^3}{\Delta x^4}\left(\overline{u}^N_{i+2} - 4\,\overline{u}^N_{i+1} + 6\,\overline{u}^N_i - 4\,\overline{u}^N_{i-1} + \overline{u}^N_{i-2}\right) \tag{3.23}$$

If the exact solution of the equation is u^N_i and the numerical solution is represented as $\overline{u}^N_i$ then the difference between these values is the error ε^N_i. This can be stated as

$$\overline{u}^N_i = u^N_i - \varepsilon^N_i \tag{3.24}$$

By substituting Eqn.(3.24) into Eqn.(3.23) the equation can be separated into two parts. The first is a function of the exact solution u^N_i which is equal to zero and can be removed, leaving an equation that is only a function of the error ε^N_i

$$\frac{\partial u}{\partial t} + c\frac{\partial u}{\partial x} + k\,\Delta x^3 \frac{\partial^4 u}{\partial x^4} = 0$$

$$0 = \frac{d\varepsilon_i}{dt} + \frac{c}{2\Delta x}\left(\varepsilon_{i+1}^N - \varepsilon_{i-1}^N\right) + \frac{k_4\, c\, \Delta x^3}{\Delta x^4}\left(\varepsilon_{i+2}^N - 4\,\varepsilon_{i+1}^N + 6\,\varepsilon_i^N - 4\,\varepsilon_{i-1}^N + \varepsilon_{i-2}^N\right) \quad (3.25)$$

The error term can now be decomposed using Fourier modes

$$\varepsilon^N = A^N e^{Ikx}$$

$$\varepsilon_{i+1}^{N+1} = A^{N+1} e^{Ik(i+1)\Delta x}$$

The amplification factor G is the ratio of error amplitudes at two consecutive time levels and is written as

$$G^{(m)} = \frac{A^m}{A^{m-1}}$$

By applying the temporal discretization of the 4-stage Runge-Kutta scheme and the Fourier decomposition, setting the phase angle $\theta = k\Delta x$, to Eqn.(3.25) the growth factor can be found using

$$G^{(1)} = 1 - \alpha_1 C_n \left[I sin\theta + k_4\left(2cos(2\theta) - 8cos\theta + 6\right)\right] \quad (3.26)$$

Where $C_n = \frac{c\Delta t}{\Delta x}$ is the Courant number. The second stage then becomes

$$G^{(2)} = 1 - \alpha_1 G^{(1)} C_n \left[I sin\theta + k_4\left(2cos(2\theta) - 8cos\theta + 6\right)\right] \quad (3.27)$$

In general, the stage growth factor can be defined by

$$G^{(m)} = 1 - \alpha_m G^{(m-1)} C_n \left[I sin\theta + k_4\left(2cos(2\theta) - 8cos\theta + 6\right)\right] \quad (3.28)$$

where $m = 4$ for a 4-stage scheme. Upon completion of the evaluation of Eqn.(3.28), the condition for stability becomes

$$\left|G^{(4)}\right| = |G| \leq 1$$

which states that, for a stable scheme, the error decays with time. The scheme is said to be unstable if the amplitude of the error grows with time at any phase angle θ.

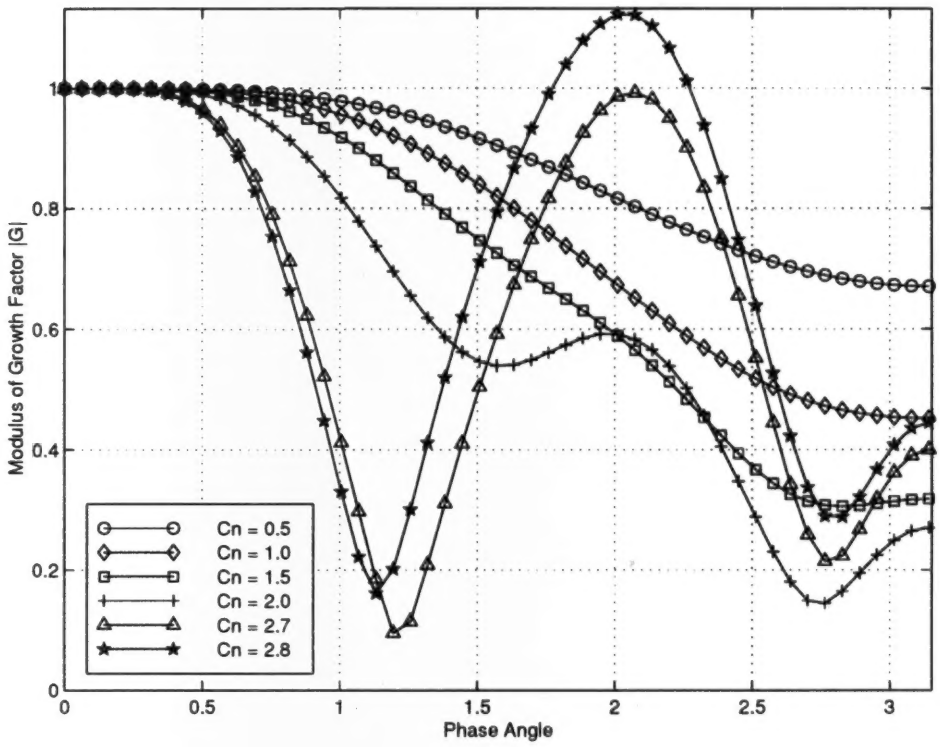

Figure 3.4: Growth Factor for Flow Equations with Increasing Courant Number

The stability limit for the Courant number is determined graphically by varying the Courant number and using $\alpha_1 = \frac{1}{4}, \alpha_2 = \frac{1}{3}, \alpha_3 = \frac{1}{2}, \alpha_4 = 1$ and $k_4 = \frac{1}{20}$.

It can be seen from Fig.(3.4) that the limiting Courant Number is $C_n = 2.7$. At any Courant number below this limit the growth factor $|G| \leq 1$ and at $C_n = 2.8$ the amplitude of $|G|$ goes above one, indicating that this scheme would be unstable at this Courant number.

To insure the fastest convergence possible, a Courant number that produces the

smallest area under the growth factor curve is required. Upon inspection of Fig.(3.4) it can be seen that at $C_n = 2.0$ the area is minimum, therefore the error is reduced for all phase angles at each time step. This will ensure faster convergence than any other C_n and it is this number which is used for all calculations.

3.3.2 Camber Line Generator

Von Neumann stability analysis was also performed on a linear, constant coefficient hyperbolic equation of the form

$$u_t + cu_x = 0 \tag{3.29}$$

to obtain a stability condition for the camber line generator.

Using the method of analysis of the previous section (Sec.3.3.1) along with the upwind spatial and 4-stage temporal discretization on the model equation the growth factor can be represented by

$$\begin{aligned} G \;=\; & \left(1 - C_n + \tfrac{1}{2}C_n^2 - \tfrac{1}{6}C_n^3 + \tfrac{1}{24}C_n^4\right) \\ & + \left(C_n - C_n^2 + \tfrac{1}{2}C_n^3 - \tfrac{1}{6}C_n^4\right)(cos(\theta) - I sin(\theta)) \\ & + \left(\tfrac{1}{2}C_n^2 - \tfrac{1}{2}C_n^3 + \tfrac{1}{4}C_n^4\right)(cos(2\theta) - I sin(2\theta)) \\ & + \left(\tfrac{1}{6}C_n^3 - \tfrac{1}{6}C_n^4\right)(cos(3\theta) - I sin(3\theta)) \\ & + \tfrac{1}{24}C_n^4\,(cos(4\theta) - I sin(4\theta)) \end{aligned} \tag{3.30}$$

Since both the phase angle and the Courant number for the limiting case are unknown, one of them must be found graphically. By varying the Courant number for all phase angles $0 \leq \theta \leq \pi$ it is determined from Fig.(3.5) that the limiting phase angle is π. Substitution of $\theta = \pi$ into Eqn.(3.30) yields

$$G = \frac{2}{3}C_n^4 - \frac{3}{4}C_n^3 + 2C_n^2 - 2C_n + 1 \tag{3.31}$$

Using the stability condition, $|G| \leq 1$, Eqn.(3.31) can be reduced to the following third order polynomial

$$C_n^3 - 2C_n^2 + 3C_n - 3 \leq 0$$

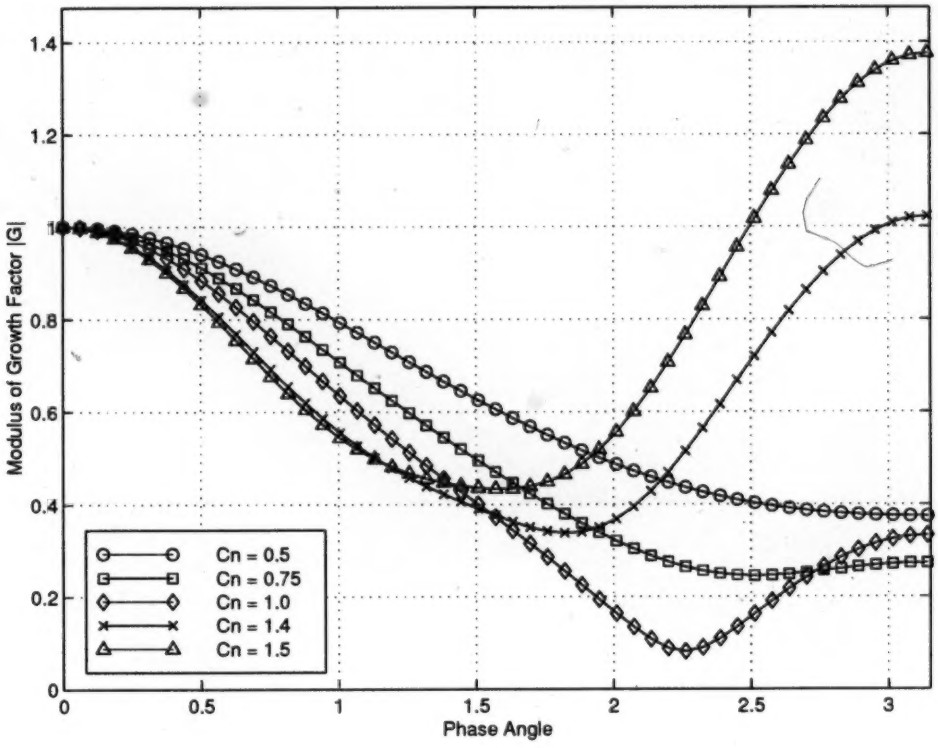

Figure 3.5: Growth Factor for Camber Line Stability

The roots of this equation can then be found using the cubic formula combined with the quadratic formula. Only one real root exists and it is this root that is taken to be the stability limit for the scheme. This root is the limiting Courant number which is

$$C_n = \sqrt[3]{\frac{43+9\sqrt{29}}{54}} - \sqrt[3]{\frac{-43+9\sqrt{29}}{54}} + \frac{2}{3} = 1.3926$$

3.4 Time Stepping

For a time accurate calculation the time step $\Delta t_{i,j}$ is calculated for each cell of the flow field, the minimum time step is then found and the entire domain is advanced by this minimum time step. For stability reasons, this ensures that all of the cells are advanced by a time step not exceeding the maximum time step for that cell. The theoretical wave speed of the flow equations should be the maximum eigenvalue obtained from the quasi - linear form along a streamline. This is

$$c_w = |\vec{V_s}| + |c|$$

This is difficult to achieve in practice, so the time step suggested by Jameson is used and is

$$q_i = u\,\Delta y_\xi - v\,\Delta x_\xi \quad c_i = c\sqrt{\Delta x_\xi^2 + \Delta y_\xi^2} \quad \Delta t_i = \frac{A_{cell}}{|q_i| + |c_i|}$$

$$q_j = -u\,\Delta y_\eta + v\,\Delta x_\eta \quad c_j = c\sqrt{\Delta x_\eta^2 + \Delta y_\eta^2} \quad \Delta t_j = \frac{A_{cell}}{|q_j| + |c_j|}$$

$$\Delta t_{i,j} = C_n \frac{\Delta t_i \Delta t_j}{\Delta t_i + \Delta t_j}$$

Where c is the local speed of sound and A_{cell} is the area of the 2-D cell.

The time step for the camber line generator is obtained using the definition of the Courant number

$$C_n = \frac{c_f \Delta t}{\Delta x}$$

for a 1D equation such as the camber line generator. The wave speed on the camber line , from theory, is defined as

$$c_f = \left|\frac{1}{2}(u^+ + u^-)\right|$$

where u^+ is the axial velocity on the upper surface of the blade and u^- the lower surface axial velocity. To keep the time step size closer to that of the flow equations,

the time step used numerically is

$$c_f = \left|\frac{1}{2}(u^+ + u^-)\right| + |c_{camb}|$$

where c_{camb} is the speed of sound on the camber line which can be approximated as

$$c_{camb} = \frac{1}{2}(c^+ + c^-)$$

This corresponds to a conservative time step for the camber line but by using this, the flow field will not be advanced in time with a large difference between the camber line and the flow field. The other advantage to using this method is that near the stagnation point at the leading edge the velocity would go to zero resulting in an infinite time step using the definition of the time step from theory.

When only the steady state solution is required, a method known as local time stepping can be used. With this method the time step calculated for each cell is used to advance the solution on a cell by cell basis. This produces a warped time integration whereby each cell is advanced by a different time step governed by the local stability requirement. Significant convergence acceleration is a result of using local time stepping.

3.5 Boundary Conditions

3.5.1 Inflow/Outflow Boundaries

The method used to specify the inlet and outlet boundary conditions is based on the method of characteristics. The signs of the eigenvalues from Eqn.(2.15) determine whether information propagates in to or out of the computational domain. If the sign is positive, information travels left to right and travels in the opposite direction if the sign is negative. Two possibilities exist for each of the boundary conditions:

Subsonic inflow

For a subsonic inflow condition, three of the eigenvalues are positive so three physical

conditions must be specified upstream of the domain. The physical conditions chosen are the stagnation pressure P_0, the stagnation temperature T_0 and the inlet flow angle β. The fourth boundary condition is obtained using a second order extrapolation to obtain the static pressure P. The primitive variables ρ, u, v, e_t can now be found using isentropic relations as well as the definition of the Mach number

$$\frac{P_0}{P} = \left(1 + \frac{\gamma - 1}{2} M^2\right)^{\frac{\gamma}{\gamma - 1}} \tag{3.32}$$

$$\frac{T_0}{T} = 1 + \frac{\gamma - 1}{2} M^2 \tag{3.33}$$

$$M = \frac{|V|}{\sqrt{\gamma RT}} \tag{3.34}$$

and the following geometric relations using the specified flow angle

$$u = \frac{|V|}{\sqrt{1 + tan^2\beta}} \qquad v = u\, tan\beta$$

By using the perfect gas law and the equation of state, the remaining primitive variables can be calculated as follows

$$\rho = \frac{P}{T}$$

$$e_t = \frac{P}{\gamma - 1} + \frac{1}{2}\rho\left(u^2 + v^2\right)$$

Once these variables have been found the conservative variables of Eqn.(2.12) are easily calculated.

Supersonic inflow

For supersonic inflow, all of the eigenvalues are positive which means that four physical conditions must be specified. In addition to P_0, T_0 and β the inlet Mach number M is chosen as the fourth condition. The above equations can then be rearranged to give the flow variables on the inflow boundary.

Subsonic outflow

With the subsonic outflow boundary only one physical condition and three extrapolated quantities are required. The physical condition chosen is the back pressure P_{back}

and ρ, u and v are obtained from inside the domain using a second order accurate extrapolation. The one remaining variable e_t can be calculated using the equation of state.

Supersonic outflow

Since all the eigenvalues are positive with supersonic flow, all the variables are extrapolated using a second order accurate method from the interior of the domain to the outflow boundary.

3.5.2 Periodic Boundaries

The calculation of an entire row of blades can be done by calculating the flow through two of the blades while enforcing periodicity in the regions upstream and downstream of the blade since the flow in the passages above and below are also flows through identical blades. The solution along the bottom edge of the domain is put into the boundary above the top edge. Similarly, the solution along the top of the domain is used as the boundary values on the bottom.

3.5.3 Blade Surface Boundary Treatment

In a conventional calculation, where the solution around a fixed geometry is required, the boundary condition enforced on the solid surfaces is the no - flux condition. This can be stated as

$$\vec{V} \cdot \vec{n} = 0$$

where $\vec{V}$ is the velocity on the surface of the blade and $\vec{n}$ is the unit vector normal to the surface. Thus, pressure is the only value that is required on the surface of the blade. All other surface flux values are set to zero to enforce the no-flux boundary condition and pressure is obtained from the equation of state using a zeroth order extrapolation of the primitive variables from the adjacent cell center.

For the inverse problem, the blade is required to produce a specified amount of work. Flow turning can be related to work through the Euler Turbine Equation

$$\dot{W} = \dot{m}\,\omega\, r\,\Delta\overline{v} = \dot{m}\Delta h_0 \tag{3.35}$$

for an axial turbomachine. The variables are: $\dot{W}$ is the work from the blade row, $\dot{m}$ is the mass flow, ω is the angular velocity of the blades, r the radial position from the center of the engine, $\Delta\overline{v}$ the overall change in velocity across the blade row in the tangential direction and Δh_0 the change in stagnation enthalpy across the blade row.

An equation is now needed to impose this flow turning condition on the blade. Following the steady analysis of Dang [2], but maintaining the unsteady term, the tangential component of the momentum equation of Eqn.(2.9) can be integrated in the pitchwise direction. Integrating from the top surface of the blade (+), through the passage to the bottom surface of the neighbouring blade (−)

$$\int_+^- \rho\frac{Dv}{Dt}dy = -\int_+^- \frac{\partial P}{\partial y}\,dy \tag{3.36}$$

the equation becomes a pressure difference, or jump, across the blade

$$P^+ - P^- = \Delta P = \int_+^- \rho\frac{Dv}{Dt}dy \tag{3.37}$$

By defining the massflux averaged pitchwise velocity, $\overline{v}$

$$\overline{v} = \overline{v}(x) = \frac{\int_+^- \rho u v dy}{\dot{m}} \tag{3.38}$$

and differentiating with respect to x, assuming $\dot{m}$ is constant

$$\dot{m}\frac{d\overline{v}}{dx} = \frac{\partial}{\partial x}\int_+^- \rho u v dy \tag{3.39}$$

Then using Leibnitz's theorem on the right hand side of the equation

$$\dot{m}\frac{d\overline{v}}{dx} = \int_+^- \frac{\partial}{\partial x}\left(\rho u v\right) dy + \left[(\rho u v)^-\right]\frac{dy^-}{dx} - \left[(\rho u v)^+\right]\frac{dy^+}{dx} \tag{3.40}$$

and expanding using the product rule, the equation becomes

$$\dot{m}\frac{d\overline{v}}{dx} = \int_{+}^{-}\left[\rho u\frac{\partial v}{\partial x} + v\frac{\partial}{\partial x}(\rho u)\right]dy + \rho uv\frac{dy^{-}}{dx} - \rho uv\frac{dy^{+}}{dx} \tag{3.41}$$

By adding and subtracting both, $\rho\frac{\partial v}{\partial t}$ and $\rho v\frac{\partial v}{\partial y}$ and using continuity

$$\dot{m}\frac{d\overline{v}}{dx} = \int_{+}^{-}\left\{\rho\left[\frac{\partial v}{\partial t} + u\frac{\partial v}{\partial x} + v\frac{\partial v}{\partial y}\right] - \rho\frac{\partial v}{\partial t} - \rho v\frac{\partial v}{\partial y} + v\left[-\frac{\partial \rho}{\partial t} - \frac{\partial}{\partial y}(\rho v)\right]\right\}dy \tag{3.42}$$

$$+\left[(\rho uv)^{-}\right]\frac{dy^{-}}{dx} - \left[(\rho uv)^{+}\right]\frac{dy^{+}}{dx}$$

then collecting terms

$$\dot{m}\frac{d\overline{v}}{dx} = \int_{+}^{-}\left[\rho\frac{Dv}{Dt} - \frac{\partial}{\partial t}(\rho v) - \frac{\partial}{\partial y}(\rho v^2)\right]dy + \left[(\rho uv)^{-}\right]\frac{dy^{-}}{dx} - \left[(\rho uv)^{+}\right]\frac{dy^{+}}{dx} \tag{3.43}$$

and then expanding this, the equation takes on the form

$$\dot{m}\frac{d\overline{v}}{dx} = \int_{+}^{-}\rho\frac{Dv}{Dt}dy - \int_{+}^{-}\frac{\partial}{\partial t}(\rho v)dy - \left(\rho v^2\right)^{-} + \left(\rho v^2\right)^{+} + \left[(\rho uv)^{-}\right]\frac{dy^{-}}{\partial x} - \left[(\rho uv)^{+}\right]\frac{dy^{+}}{\partial x} \tag{3.44}$$

the derivatives $\frac{dy^{+}}{dx}$ and $\frac{dy^{-}}{dx}$ can be obtained from Eqn.(2.1) and Eqn.(2.2) as

$$\frac{dy^{+}}{dx} = \frac{\partial}{\partial x}\left(f + \frac{T}{2}\right), \qquad \frac{dy^{-}}{dx} = \frac{\partial}{\partial x}\left(f - \frac{T}{2}\right) \tag{3.45}$$

Which, when substituted into Eqn.(2.5) and Eqn.(2.6), assuming steady state, become

$$\frac{dy^{+}}{dx} = \frac{v^{+}}{u^{+}}, \qquad \frac{dy^{-}}{dx} = \frac{v^{-}}{u^{-}} \tag{3.46}$$

Substitution of these equations into Eqn.(3.44) and rearranging yields

$$\int_{+}^{-}\rho\frac{Dv}{Dt}dy = \dot{m}\frac{d\overline{v}}{dx} + \int_{+}^{-}\frac{\partial}{\partial t}(\rho v)dy \tag{3.47}$$

By substituting Eqn.(3.47) into Eqn.(3.37) the final form of the blade loading equation becomes

$$\Delta P = \dot{m}\frac{d\overline{v}}{dx} + \int_{+}^{-}\frac{\partial}{\partial t}(\rho v)dy \tag{3.48}$$

which, at steady state, is the same form that Dang has long advocated. This equation is then used on the boundary of the blade to impose the pressure jump condition. Using a first order Taylor series expansion, the pressure on the upper and lower blade surfaces can be obtained

$$P^{+} = P_{camb} + \frac{\Delta P}{2} \tag{3.49}$$

$$P^{-} = P_{camb} - \frac{\Delta P}{2} \tag{3.50}$$

where

$$P_{camb} = \frac{1}{2}\left(P_{i,j=2} + P_{i,j=my}\right)$$

The unsteady term of Eqn.(3.48) will help prevent applying a discontinuous boundary condition in time. By adding this term, very little computational time is added because the unsteady term can be obtained by integrating the residual of the y-momentum equation which is already known from the previous cycle as follows

$$\int_{+}^{-} \frac{\partial}{\partial t}(\rho v)dy = \sum_{y} \frac{Residual\ y\text{–}mom\ eqn}{\Delta x \Delta y}\Delta y \tag{3.51}$$

Therefore, no additional calculation is needed to obtain this term. The advantages of using this boundary condition over the steady form used by Dang will be shown in Chapter 4.

The objective of this inverse design method is to design a blade that produces a specified amount of flow turning $\Delta\overline{v}$ that follows the shape of the input turning distribution. These values are required input from the designer. The total turning $\Delta\overline{v}$ is chosen from the work requirement of that row of blades and the shape of the distribution is chosen based primarily on designer experience. One family of turning distribution shapes suggested by Dang [2] are

$$\frac{d\overline{v}}{dx} = K\, x^{m}\,(1-x)^{n} \tag{3.52}$$

With this, the kutta condition is satisfied at both the leading and trailing edges and m and n are used to adjust the general shape of the curve as well as moving the location of the maximum value. The constant K is defined as

$$K = \frac{\Delta\overline{v}}{\int_{le}^{te} x^m(1-x)^n dx} \tag{3.53}$$

where

$$\Delta\overline{v} = \int_{le}^{te} \frac{d\overline{v}}{dx} dx$$

The value of $\frac{d\overline{v}}{dx}$ must be adaptive to the flow field such that, the total turning requirement is satisfied. This is done by generating the average swirl velocity distribution $\overline{v}(x)$ in the bladed region

$$\overline{v}(x) = \overline{v}(le) + \int_{le}^{x} \frac{d\overline{v}}{dx} dx \tag{3.54}$$

This equation states that the average swirl velocity starts at $\overline{v}(le)$ at the leading edge, which is obtained from the solution of the flow field, and is incremented along the axial chord of the blade by the partial area under the turning curve until the trailing edge value is obtained, which is $\overline{v}(te) = \overline{v}(le) + \Delta\overline{v}$.

The turning distribution that satisfies both the total turning and the turning shape can then be obtained by differentiating $\overline{v}(x)$ with respect to x

$$\frac{d\overline{v}}{dx} = \frac{d}{dx}\{\overline{v}(x)\}$$

It is this equation that is used in Eqn.(3.48) to generate the blade pressure boundary condition.

For the inverse method, the blade surface is permeable during the iteration process. The blade geometry is updated by aligning it with the flow during the transient time marching process. When the calculation has converged the blade is a material line

in the flow hence, satisfying the no-flux boundary condition of a solid surface. Since the blade is permeable, all of the primitive variables must be given as boundary conditions on the blade surface. The first variable is the pressure which enforces the turning requirement and is obtained from Eqn.(3.49) and Eqn.(3.50). The second variable is the y-component of velocity v, this can be calculated using a modified camber line generator. Instead of adding the equations together, Eqn.(2.6) can be subtracted from Eqn.(2.5) to produce

$$\Delta v = v^+ - v^- = \left(u^+ - u^-\right) \frac{\partial f}{\partial x} - \frac{(u^+ + u^-)}{2} \frac{dT}{dx} \tag{3.55}$$

this can then be used to construct the v velocity on the upper and lower blade surfaces using a first order Taylor series expansion as follows

$$v^+ = v_{camb} + \frac{\Delta v}{2}$$

$$v^- = v_{camb} - \frac{\Delta v}{2}$$

where

$$v_{camb} = \frac{1}{2}\left(v_{i,j=2} + v_{i,j=my}\right)$$

This velocity jump condition is similar to the treatment for the pressure jump condition. The third value is obtained from interpolation of the u velocity as follows

define the camber value as

$$u_{camb} = \frac{1}{2}\left(u_{i,j=2} + u_{i,j=my}\right)$$

and then the blade values can be obtained from

$$u^+ = \frac{1}{2}\left(u_{i,j=2} + u_{camb}\right)$$

$$u^- = \frac{1}{2}\left(u_{i,j=my} + u_{camb}\right)$$

The fourth and final boundary condition comes from a zeroth order extrapolation of density, ρ, from the adjacent cell center value. To find the last primitive variable, the equation of state is used to calculate e_t on both the upper and lower blade surfaces. With all of these values defined, all of the boundary conditions are specified for the inverse problem.

To demonstrate the versatility of this method and to further explain the pressure boundary condition, three cases are shown using Eqn.(3.52) with different values for m and n. All three cases have the same total turning specified $\Delta\overline{v} = -0.2$ hence, produce the same amount of work. This value, along with the chosen thickness distribution of Fig.(3.6) leaves only the specification of the turning shape distribution to define the inverse problem.

This thickness distribution was chosen based primarily on structural and manufacturing constraints. It has a rounded leading edge which, for subsonic inflow, allows for a wider operating range of incidence angles. These cases all have an inlet Mach number of 0.342, spacing to chord ratio $\frac{S}{C} = 1$ and an inlet flow angle $\beta = 0°$.

Case 1: Leading edge loaded blade.

Using Eqn.(3.52) with $m = \frac{3}{5}$ and $n = 2$ the turning shape distribution that corresponds to a leading edge loaded blade is shown in Fig.(3.7). By using this shape, most of the flow turning is accomplished in the first 50 % of the chord. The Mach number on the top surface of the blade is the critical value in determining whether the flow will separate in these cases. A steep gradient is more likely to cause separation. For this case, the flow is accelerated quickly and reaches its maximum at about 23 % chord as shown in Fig(3.8). The remainder of the blade is used to bring this value down slowly to avoid high pressure gradients.

Case 2: Symmetrically loaded blade.

Using Eqn.(3.52) with $m = 1$ and $n = 1$ the turning distribution that corresponds to a symmetrically loaded blade is shown in Fig.(3.9). This shape has an equal weighting

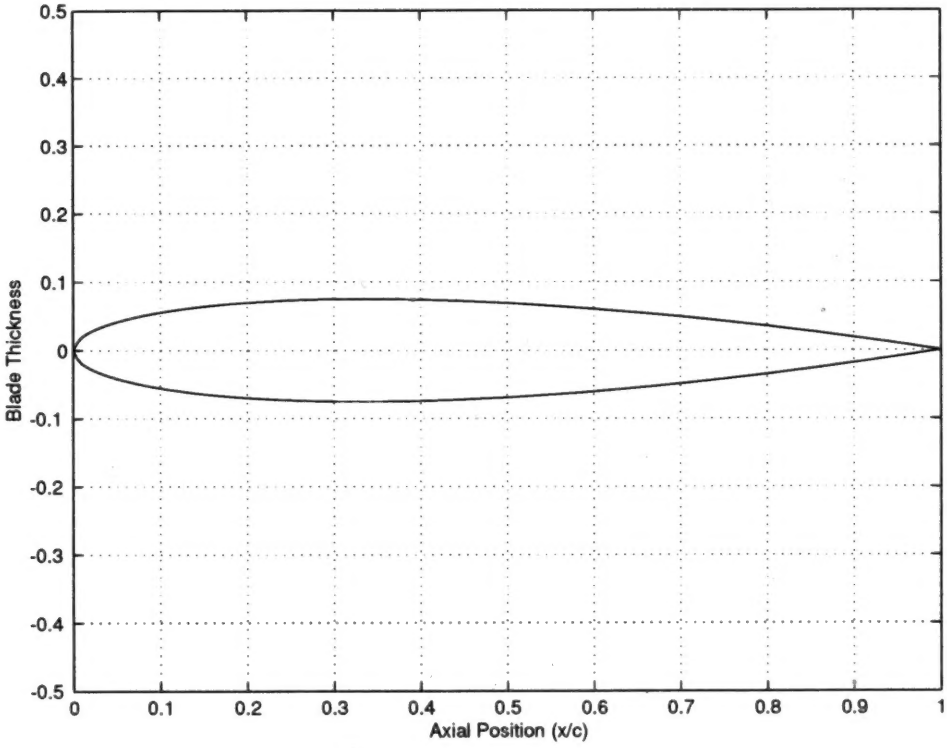

Figure 3.6: Thickness Distribution Used for Testcases

of flow turning on the first and last 50 % of the chord. The gradient on the top surface in Fig.(3.10) is steeper than that of the leading edge loaded blade which would cause it to separate sooner.

Case 3: Trailing edge loaded blade.

Using Eqn.(3.52) with $m = 2$ and $n = \frac{3}{5}$ the turning distribution that corresponds to a trailing edge loaded blade is shown in Fig.(3.11). Looking at the top surface Mach number in Fig.(3.12) this blade, in a viscous flow, would most assuredly cause

separation and would not produce the required turning.

By comparing the results from these three cases it is clear that this inverse method produces blade geometries that allow control of the acceleration and deceleration of the fluid. With experience, the designer can design a blade that produces the specified amount of turning while controlling the adverse pressure gradient to avoid separation.

Text resumes on page 49

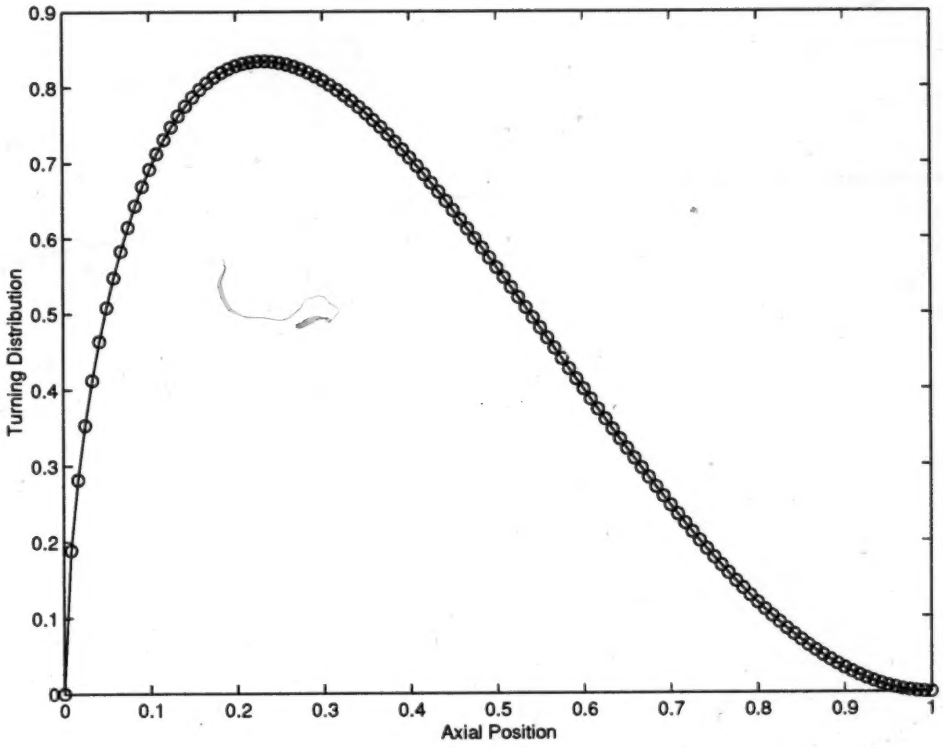

Figure 3.7: Turning Distribution Shape for the Leading Edge Loaded Blade

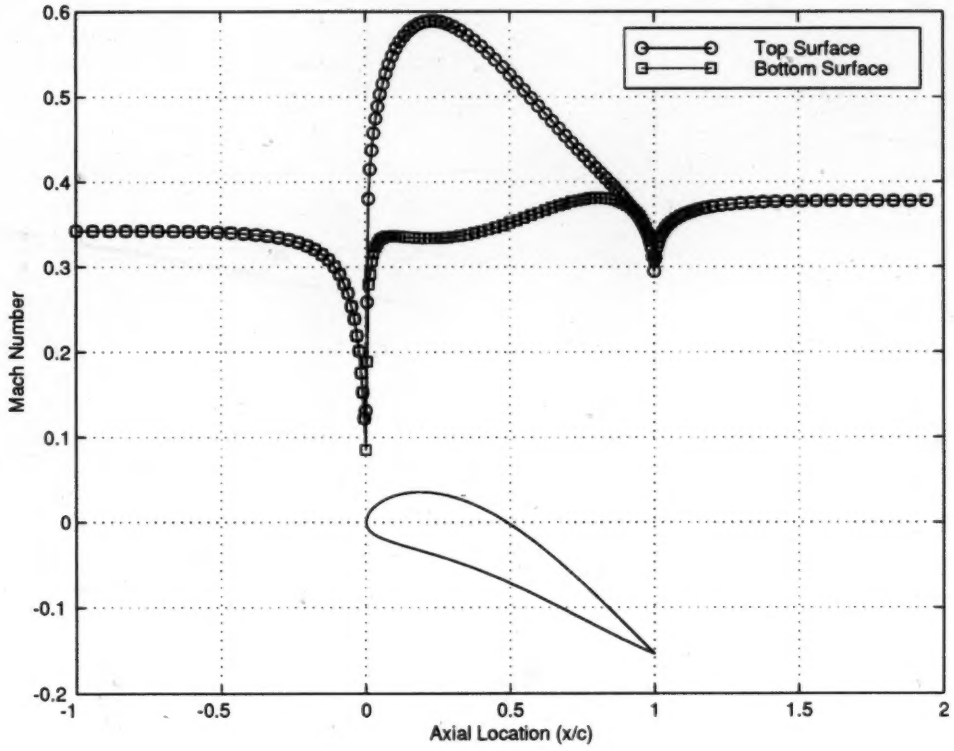

Figure 3.8: Mach Number and Converged Blade Shape for the Leading Edge Loaded Blade

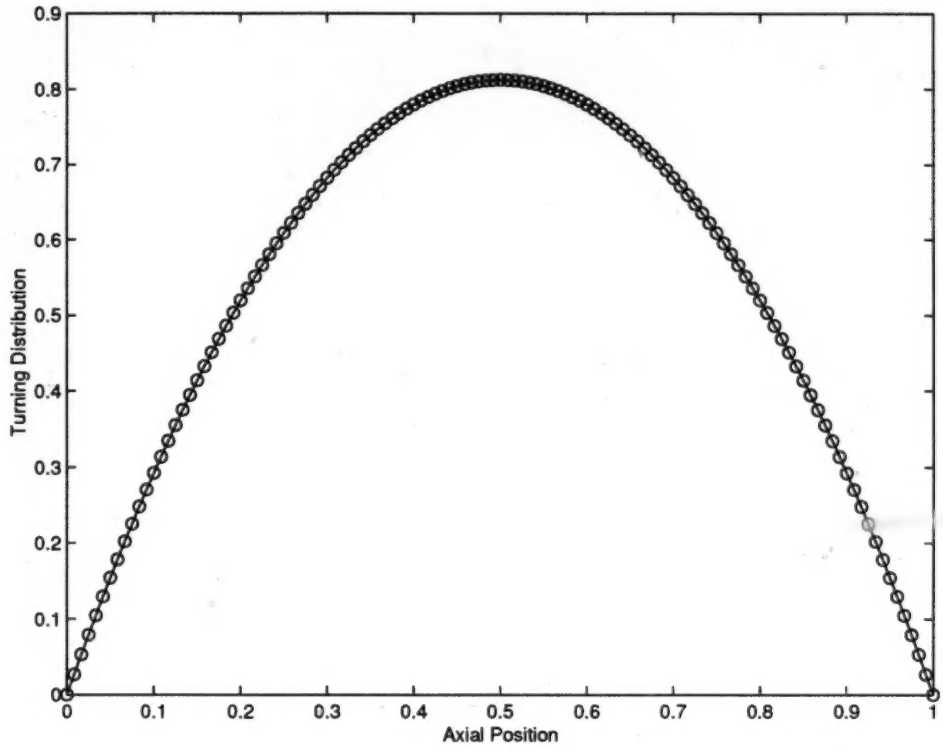

Figure 3.9: Turning Distribution Shape for the Symmetrically Loaded Blade

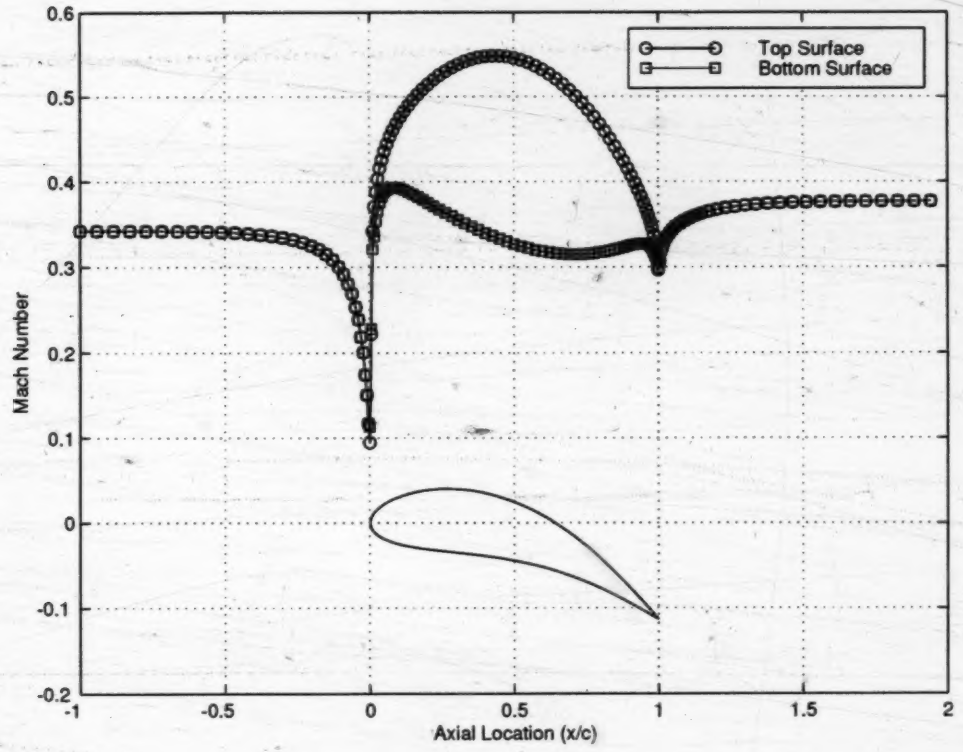

Figure 3.10: Mach Number and Converged Blade Shape for the Symmetrically Loaded Blade

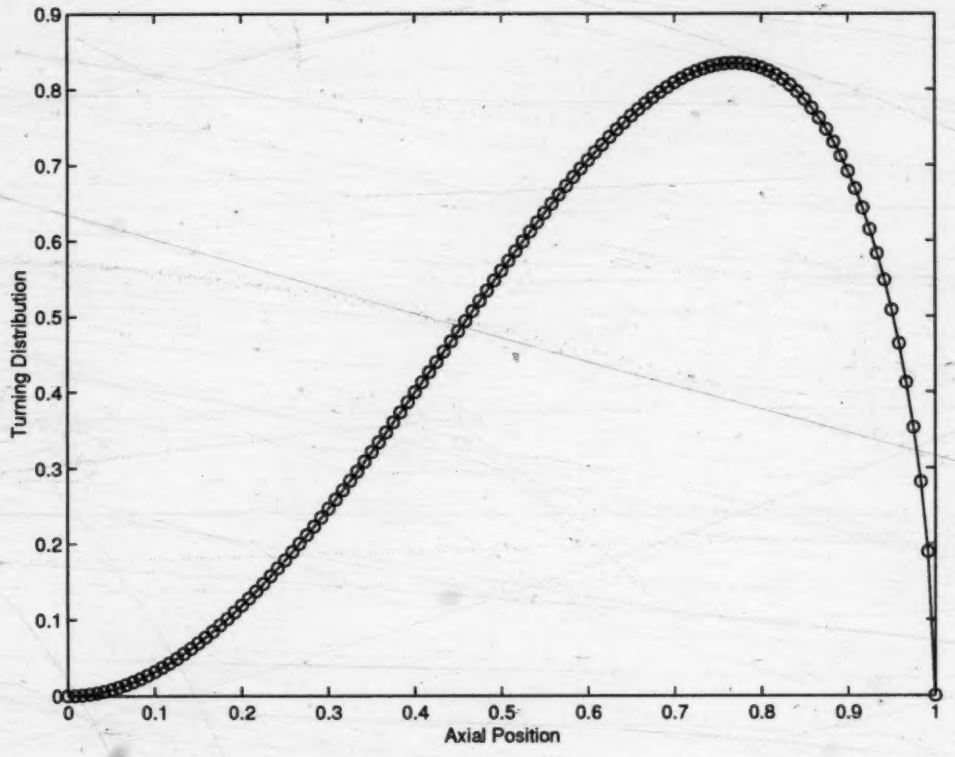

Figure 3.11: Turning Distribution Shape for the Trailing Edge Loaded Blade

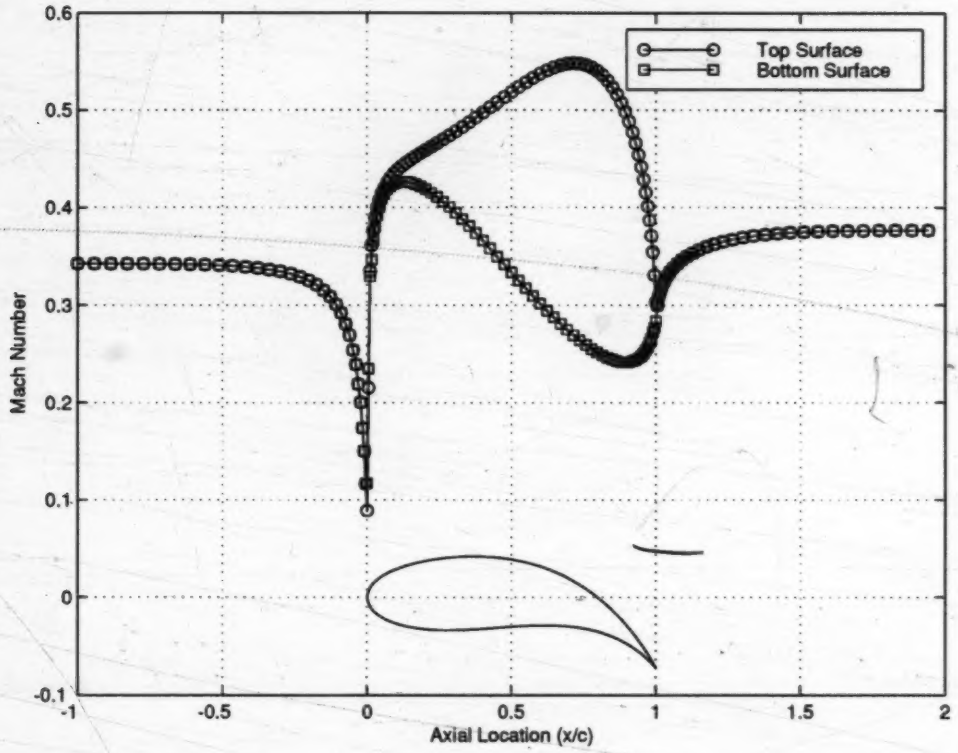

Figure 3.12: Mach Number and Converged Blade Shape for the Trailing Edge Loaded Blade

When the turning and thickness distributions are specified, resolution of the input becomes an important factor. Since the x locations of the grid are not known until the grid has been generated with the code, the distributions must be specified using designer chosen x locations. The data is then interpolated onto the grid locations using a Taylor series as follows

$$f_g = f_a + (x_g - x_a)\frac{df_a}{dx} + \frac{(x_g - x_a)^2}{2}\frac{d^2 f_a}{dx^2} + \frac{(x_g - x_a)^3}{6}\frac{d^3 f_a}{dx^3}$$

where f_g is the value of the function on the grid points x_g, f_a is the value of the function on the input points x_a.

If too few points are specified on the distributions, the turning and thickness will not be transferred accurately from the arbitrary x locations to the grid locations resulting in a loss of accuracy in the entire flow field. To show this effect, two cases are presented, one with 41 and the other with 121 points on the turning and thickness distributions. Both cases have 64 grid points in the bladed region. Both cases have exactly the same input specified for the flow field, the only difference is the resolution of the two distributions. The two turning distributions are shown superimposed in Fig.(3.13). The differences between these two plots looks to be negligible except at the leading edge region where there is some difference. The two thickness distributions are shown in Fig.(3.14). Again the only difference appears to be at the leading edge. The Mach number distribution comparison of the pressure side of the blade is shown in Fig.(3.15). This plot shows a significant difference in the entire flow field. The flow field is affected so severely that both the upstream and downstream Mach numbers are different. A detail view of the leading edge region is shown in Fig.(3.16) where, the 41 point distribution has produced a large overshoot of the Mach number. By increasing the resolution of the distributions, the blade can be more accurately transferred to the grid locations resulting in a more accurate simulation.

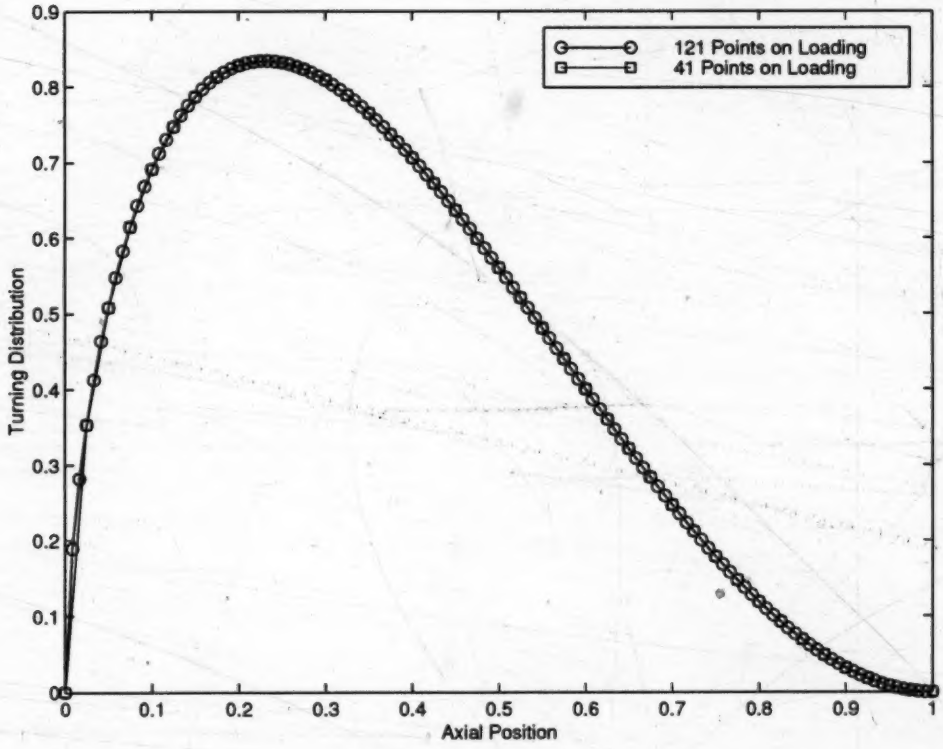

Figure 3.13: Comparison Between the Turning Distributions Using 121 & 41 Points on the curve

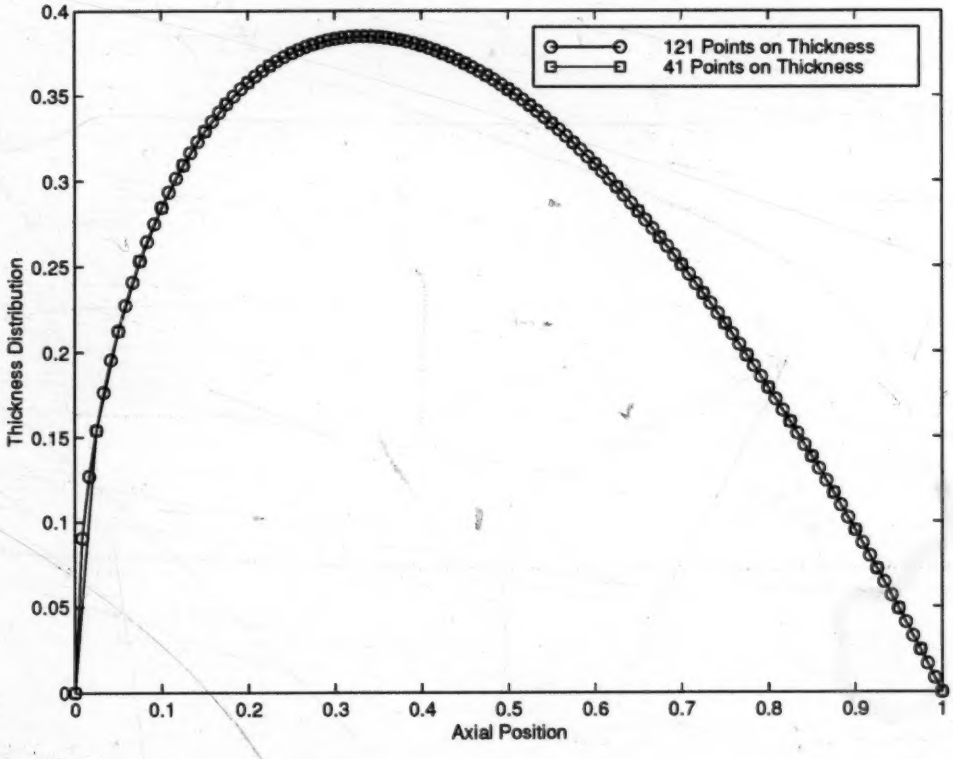

Figure 3.14: Comparison Between the Thickness Distributions Using 121 & 41 Points on the curve

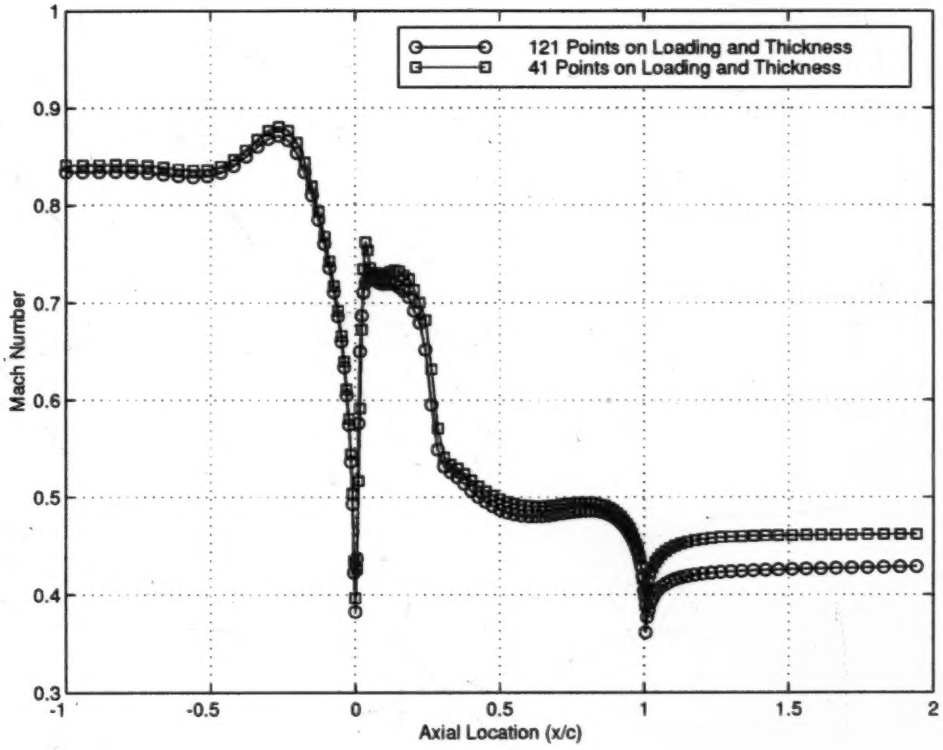

Figure 3.15: Comparison of Pressure Side Surface Mach Numbers for 121 & 41 Points of Loading and Thickness Distributions

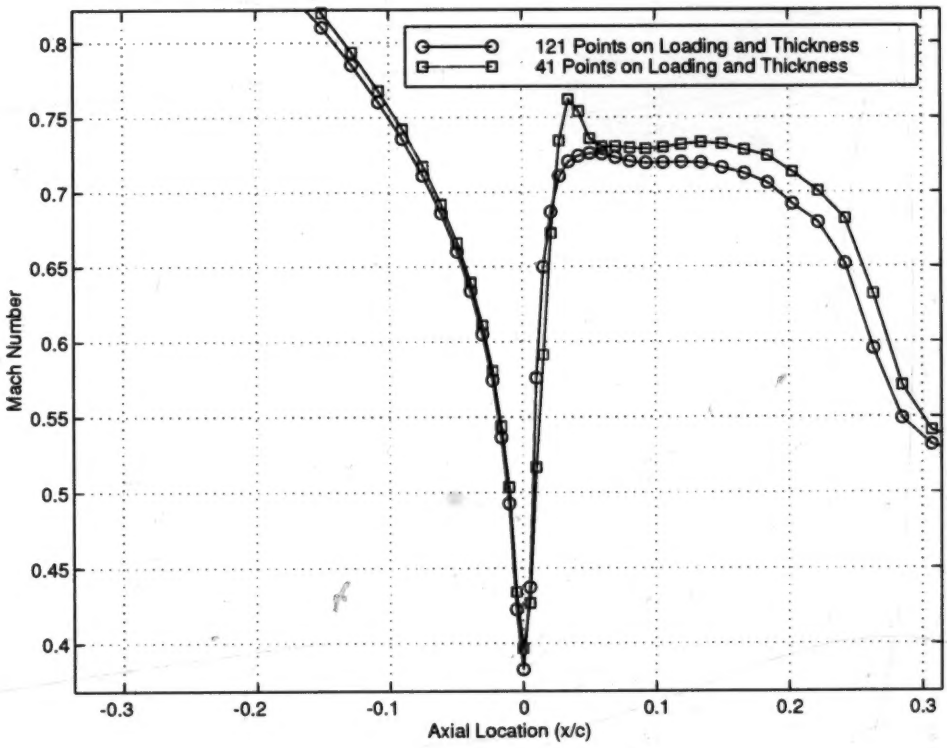

Figure 3.16: Detail View of Leading Edge Region

3.5.4 Blade Surface Boundary Treatment: Transonic Flow

In principle, both the steady and unsteady forms of the pressure boundary condition are applicable to all flow, but the resulting transonic blade designs are often impractical to use. Since these conditions are based on specifying a given turning distribution, a continuous blade geometry can only be obtained from a discontinuous turning distribution. Thus, without knowing the effects of the shock a priori, there is little chance of designing a smooth blade shape. While these designs are interesting, they result in flows that are unlikely to be achieved in practice. So instead, the pressure boundary condition is modified for transonic flows.

From the complex-lamellar velocity decomposition of Sec.(2.5), a new treatment for transonic blades can be obtained.

Restating the decomposition of Eqn.(2.36)

$$u_i = \frac{\partial \phi}{\partial x_i} + A_j \frac{\partial X_j}{\partial x_i} + \eta \frac{\partial s}{\partial x_i} \tag{3.56}$$

Since the last term can only exist downstream of a shock, in inviscid flow, this equation can be reinterpreted as

$$u_i = u_i^\circ + \eta \frac{\partial s}{\partial x_i} \tag{3.57}$$

where u_i° is the velocity field that would otherwise exist in a shockless flow. Following Yokota [16] and substituting Eqn.(3.57) into the linear momentum equation of Eqn.(2.9) the equation becomes

$$\frac{Du_i^\circ}{Dt} + \frac{D}{Dt}\left\{\eta \frac{\partial s}{\partial x_i}\right\} = -\frac{1}{\rho}\frac{\partial P}{\partial x_i} \tag{3.58}$$

which can be expanded to

$$\rho \frac{Du_i^\circ}{Dt} + \rho \frac{D\eta}{Dt}\frac{\partial s}{\partial x_i} + \rho\eta \frac{D}{Dt}\left\{\frac{\partial s}{\partial x_i}\right\} = -\frac{\partial P}{\partial x_i} \tag{3.59}$$

Since x_i are the coordinates in the Eulerian sense and $\frac{D}{Dt}$ is a material derivative, the

third term must be expanded as follows

$$\begin{aligned}
\rho\eta\frac{D}{Dt}\left\{\frac{\partial s}{\partial x_i}\right\} &= \rho\eta\frac{\partial}{\partial t}\left(\frac{\partial s}{\partial x_i}\right) + \rho\eta u_j\frac{\partial}{\partial x_j}\left(\frac{\partial s}{\partial x_i}\right) \\
&= \rho\eta\frac{\partial}{\partial t}\left(\frac{\partial s}{\partial x_i}\right) + \rho\eta u_j\frac{\partial}{\partial x_i}\left(\frac{\partial s}{\partial x_j}\right) \\
&= \rho\eta\frac{\partial}{\partial t}\left(\frac{\partial s}{\partial x_i}\right) + \rho\eta\frac{\partial}{\partial x_i}\left(u_j\frac{\partial s}{\partial x_j}\right) - \rho\eta\frac{\partial u_j}{\partial x_i}\frac{\partial s}{\partial x_j} \\
&= \rho\eta\frac{\partial}{\partial x_i}\left\{\frac{\partial s}{\partial t} + \rho\eta u_j\frac{\partial s}{\partial x_j}\right\} - \rho\eta\frac{\partial u_j}{\partial x_i}\frac{\partial s}{\partial x_j} \qquad (3.60)
\end{aligned}$$

Which results in Eqn.(3.59) taking on the form

$$\rho\frac{Du_i^\circ}{Dt} + \rho\frac{D\eta}{Dt}\frac{\partial s}{\partial x_i} + \rho\eta\frac{\partial}{\partial x_i}\left\{\frac{Ds}{Dt}\right\} - \rho\frac{\partial u_j}{\partial x_i}\left\{\eta\frac{\partial s}{\partial x_j}\right\} = -\frac{\partial P}{\partial x_i} \qquad (3.61)$$

Using the Weber transformation from Sec.(2.5)

$$\frac{D\eta}{Dt} = \Theta$$

where Θ is temperature and for an inviscid fluid

$$\frac{Ds}{Dt} = 0$$

the linear momentum equation becomes

$$\rho\frac{Du_i^\circ}{Dt} + \rho\Theta\frac{\partial s}{\partial x_i} - \rho\frac{\partial u_j}{\partial x_i}\left\{\eta\frac{\partial s}{\partial x_j}\right\} = -\frac{\partial P}{\partial x_i} \qquad (3.62)$$

Integrating the y-component of this equation in the pitchwise direction gives

$$\Delta P = \int_+^- \rho\frac{Dv_i^\circ}{Dt}dy + \int_+^- \rho\Theta\frac{\partial s}{\partial x_i}dy - \int_+^- \rho\frac{\partial u_j}{\partial x_i}\left\{\eta\frac{\partial s}{\partial x_j}\right\}dy \qquad (3.63)$$

Following a similar procedure from Sec.(3.5.3) starting at Eqn.(3.36) a modified boundary condition for transonic flow is obtained

$$\Delta P = \dot{m}\frac{d\overline{v}^\circ}{dx} + \int_+^- \frac{\partial}{\partial t}\left(\rho v_\circ\right)dy + \int_+^- \rho\Theta\frac{\partial s}{\partial y}dy - \int_+^- \rho\frac{\partial u_j}{\partial y}\left\{\eta\frac{\partial s}{\partial x_j}\right\}dy \qquad (3.64)$$

An expression for $\frac{\partial s}{\partial y}$ must now be found. Using Eqn.(2.30) the differential element ds can be found as

$$ds = \frac{dh}{\Theta} - \nu \frac{dP}{\Theta}$$

Using the following relations for a perfect gas

$$dh = C_p \, d\Theta$$

$$\nu = \frac{R\Theta}{P}$$

where C_p is the specific heat capacity of the fluid in a constant pressure process, the equation becomes

$$ds = C_p \frac{d\Theta}{\Theta} - R \frac{dP}{P}$$

Integrating this from state 1 to state 2 assuming C_p is constant

$$s_2 - s_1 = C_p \, ln \left(\frac{\Theta_2}{\Theta_1} \right) - R \, ln \left(\frac{P_2}{P_1} \right) \tag{3.65}$$

Also,

$$R = C_p - C_v$$

$$\gamma = \frac{C_p}{C_v}$$

where R is the gas constant, C_v is the specific heat capacity of the fluid in a constant volume process and γ is the ratio of specific heats. Substitution of these relations into Eqn.(3.65) gives the entropy change of a perfect gas

$$\Delta s = R \, ln \left\{ \left(\frac{\Theta_2}{\Theta_1} \right)^{\frac{\gamma}{\gamma - 1}} \left(\frac{P_1}{P_2} \right) \right\} \tag{3.66}$$

The entropy term of the boundary condition, Eqn.(3.64), can now be approximated by

$$\int_{+}^{-} \rho \Theta \frac{\partial s}{\partial y} dy \approx \sum_{+}^{-} \rho \Theta \frac{\Delta s}{\Delta y} \Delta y \tag{3.67}$$

Since

$$P = \rho R \Theta$$

and substitution of the equation for Δs the term can be approximated numerically as

$$\int_{+}^{-} \rho \Theta \frac{\partial s}{\partial y} dy \approx \sum_{+}^{-} P \, ln \left\{ \left(\frac{\Theta_{i,j+\frac{1}{2}}}{\Theta_{i,j-\frac{1}{2}}} \right)^{\frac{\gamma}{\gamma-1}} \left(\frac{P_{i,j-\frac{1}{2}}}{P_{i,j+\frac{1}{2}}} \right) \right\} \tag{3.68}$$

where the subscripts $(i, j+\frac{1}{2})$ and $(i, j-\frac{1}{2})$ refer to the cells upper and lower surface respectively.

Only the last term of Eqn.(3.64) still requires attention. The integrated shock velocity term can be expressed as

$$\int_{+}^{-} \rho \frac{\partial u_j}{\partial y} \left\{ \eta \frac{\partial s}{\partial x_j} \right\} dy = \int_{+}^{-} \rho \frac{\partial u_\tau}{\partial y} \left\{ \eta \frac{\partial s}{\partial \tau} \right\} dy \tag{3.69}$$

where τ is the direction tangent to the flow. Given that the velocity component generated downstream of a weak normal shock is likely to be constant, the following expression is obtained

$$\eta \frac{\partial s}{\partial x_j} = u^s \approx c \, H(x - x_s) \tag{3.70}$$

where c is a scalar constant and $H(x - x_s)$ is a Heaviside step function triggered at the shock location x_s. Therefore, the integrated shock velocity term can be modeled as

$$\int_{+}^{-} \rho \frac{\partial u_j}{\partial y} \left\{ \eta \frac{\partial s}{\partial x_j} \right\} dy \approx c \, H(x - x_s) \int_{+}^{-} \rho \frac{\partial u_\tau}{\partial y} dy \tag{3.71}$$

For a weak transonic flow, whose shock is nearly aligned in the pitchwise direction this model can be further reduced to

$$\int_{+}^{-} \rho \frac{\partial u_j}{\partial y} \left\{ \eta \frac{\partial s}{\partial x_j} \right\} dy \approx k \, H(x - x_s) \tag{3.72}$$

where k is scalar constant chosen to keep the blade geometrically continuous. Thus, for a transonic flow, the pressure boundary condition becomes

$$\Delta P = \dot{m}\frac{d\overline{v^{\circ}}}{dx} + \int_{+}^{-} \frac{\partial}{\partial t}(\rho v_{\circ})\, dy + \int_{+}^{-} \frac{P}{y_{i,j+\frac{1}{2}} - y_{i,j-\frac{1}{2}}}\, ln\left\{\left(\frac{\Theta_{i,j+\frac{1}{2}}}{\Theta_{i,j-\frac{1}{2}}}\right)^{\frac{\gamma}{\gamma-1}}\left(\frac{P_{i,j-\frac{1}{2}}}{P_{i,j+\frac{1}{2}}}\right)\right\} dy \tag{3.73}$$

$$-k\ H(x - x_s)$$

This new treatment allows the inverse design of a blade whose geometry is both continuous and faithful to the prescribed flow turning distribution upstream of the shock.

CHAPTER 4

RESULTS

4.1 Effect of Material Camber Line Treatment

The new treatment of the camber line as a material line in the fluid is compared to the original approach, whereby, the upstream grid line was generated using a straight line extrapolation based on the inlet flow angle. Four different test cases are presented: two in subsonic flow and one in each of the transonic and supersonic flow regimes. When there is any upstream influence from the blade, the accuracy of the calculation can be improved and the time for convergence can be decreased. This can be attributed to the fact that the grid line is a material line, essentially making the calculation 1-D along the periodic boundary. All of the design calculations presented here were performed on sheared H-type meshes. A typical sheared H-type mesh is shown in Fig.(4.1). The numerical domain consists of 128 X 32 cells with 64 cells in the bladed region. The domain was extended one chord upstream and downstream of the leading and trailing edges, respectively. Grid lines were clustered near the leading and trailing edges in the x-direction and near the blade surfaces in the y-direction.

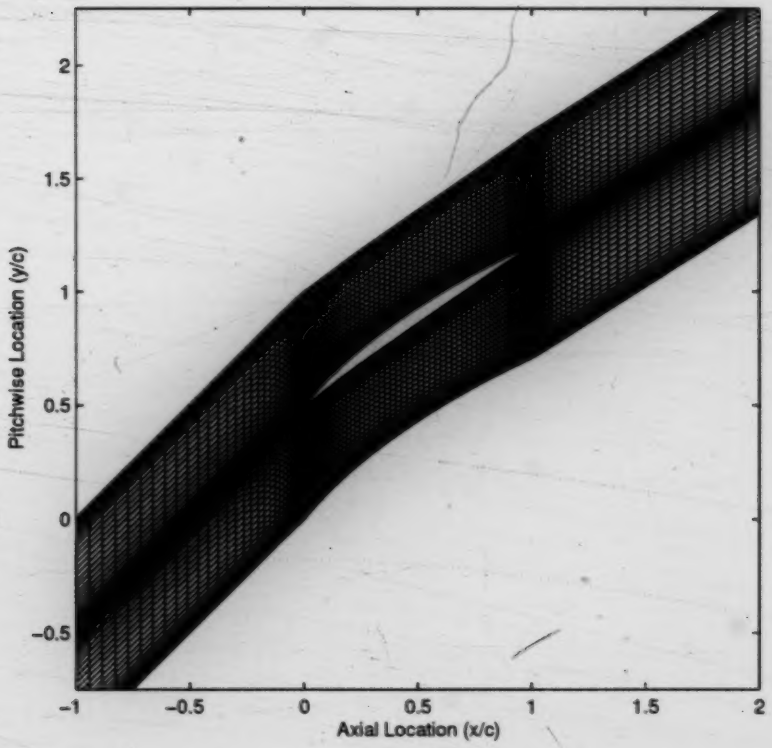

Figure 4.1: Typical Sheared H-Type Mesh

4.1.1 Subsonic Testcase: Turbine Blade at Mach 0.3

The first subsonic case is a low mach number turbine blade designed to produce a mass flow of $\dot{m} = .352\frac{P_o C}{\sqrt{RT_o}}$ for a specified back pressure of $P = 0.9P_o$. The spacing to chord ratio is set at unity and the inlet flow angle at $\beta = 0°$. The turning distribution used is generated from $\frac{d\overline{v}}{dx} = Kx^m(1-x)^n$ where $m = \frac{1}{4}$ and $n = \frac{7}{4}$, with the total turning specified as $\Delta\overline{v} = 0.25\sqrt{RT_o}$ and is shown in Fig.(4.2). The thickness distribution used is shown in Fig.(4.3) with a maximum thickness to spacing ratio of $\frac{T_{max}}{S} = 0.25$, this blade has a rounded leading edge and a sharp trailing edge. This turning distribution produces the converged blade shown in Fig.(4.4) which corresponds to a total turning of 33°. The converged flow field is shown in Fig.(4.5). The stagnation point near the leading edge of this blade is slightly closer to the pressure side of the blade, not directly on the leading edge.

This calculation was done using both the original treatment of Dang and the new material camber line. The differences between the two upstream grid lines is shown in Fig.(4.6). With the upstream influence this blade generates, the flow starts to turn before it reaches the blade, moving the stagnation point off the leading edge. With the material camber line, the grid line follows the flow to the stagnation point. The original treatment used a straight line extrapolation based on the inflow angle. Accuracy is one of the advantages in using this new method over the straight line method. This can be seen from the surface Mach Numbers for the two camber treatments shown in Figs.(4.7) and (4.8). The primary difference in these plots is near the leading edge. A detail view of the comparisons at the leading edge are shown in Figs.(4.9) and (4.10). Globally, these two methods produce a flow field that has an inlet Mach number of 0.31 and an exit Mach number of 0.39, but, the leading edge is captured much better with the material camber line. The original method produces an overshoot at the leading edge which introduces an error into the calculation. Due

to this overshoot the difference between the Mach numbers at the leading edge is 0.08. The effect this has on the convergence to steady state is shown in Fig.(4.11). The error is reduced much more rapidly with the material camber line generator,30000 iterations instead of 60000, because the leading edge is captured

more accurately. This case produced the largest difference between the upstream grid lines which corresponds to the biggest difference in surface Mach number plots and the convergence acceleration.

Text resumes on page 73

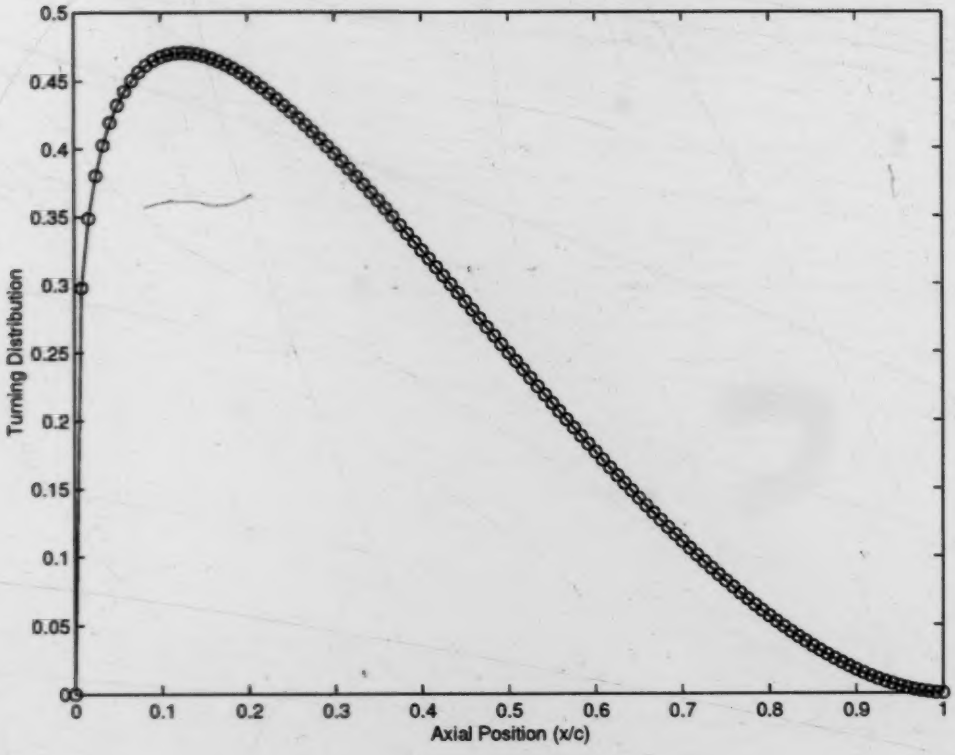

Figure 4.2: Specified Turning Distribution for the Mach 0.3 Turbine Blade

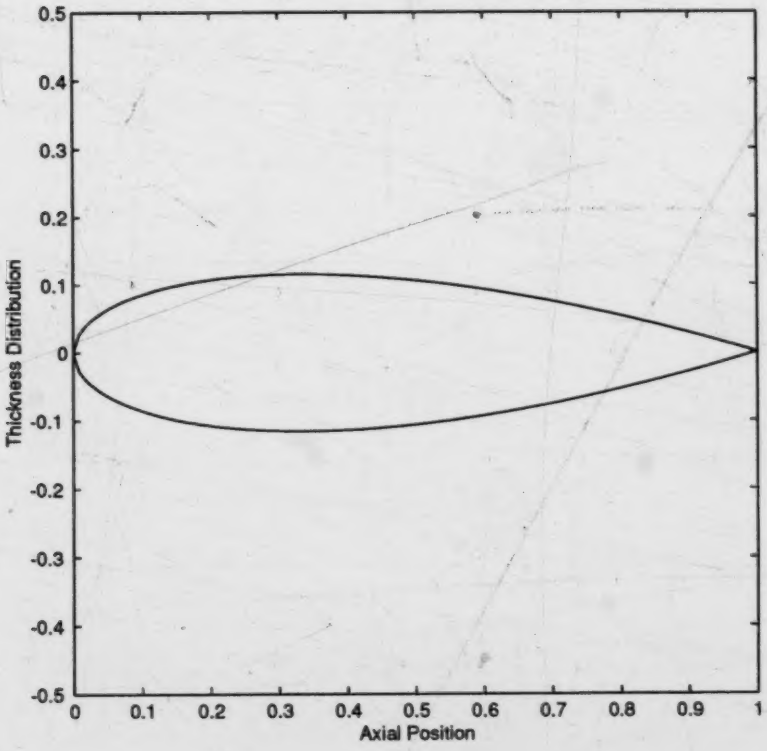

Figure 4.3: Specified Thickness Distribution for the Mach 0.3 Turbine Blade

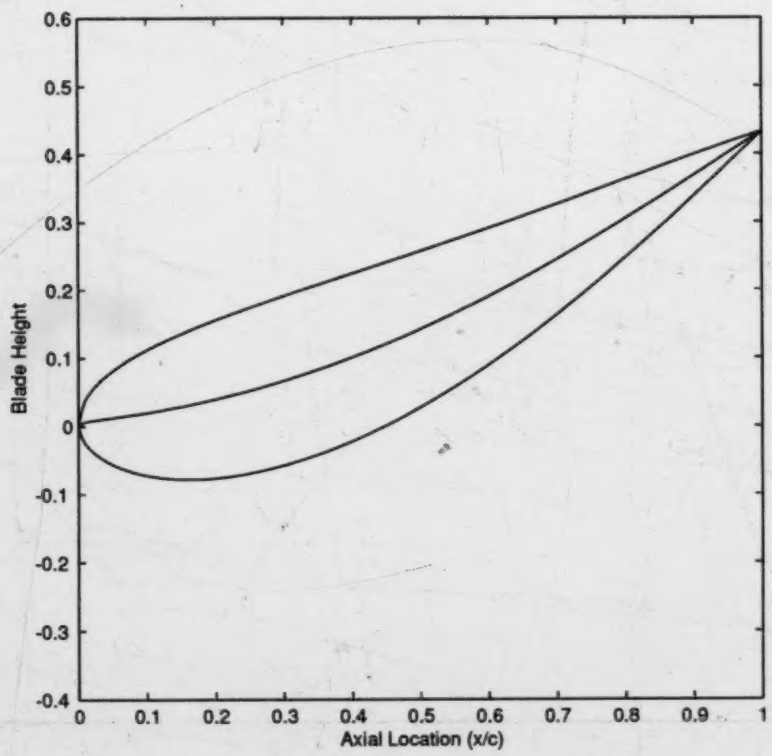

Figure 4.4: Converged Blade shape for the Mach 0.3 Turbine Blade

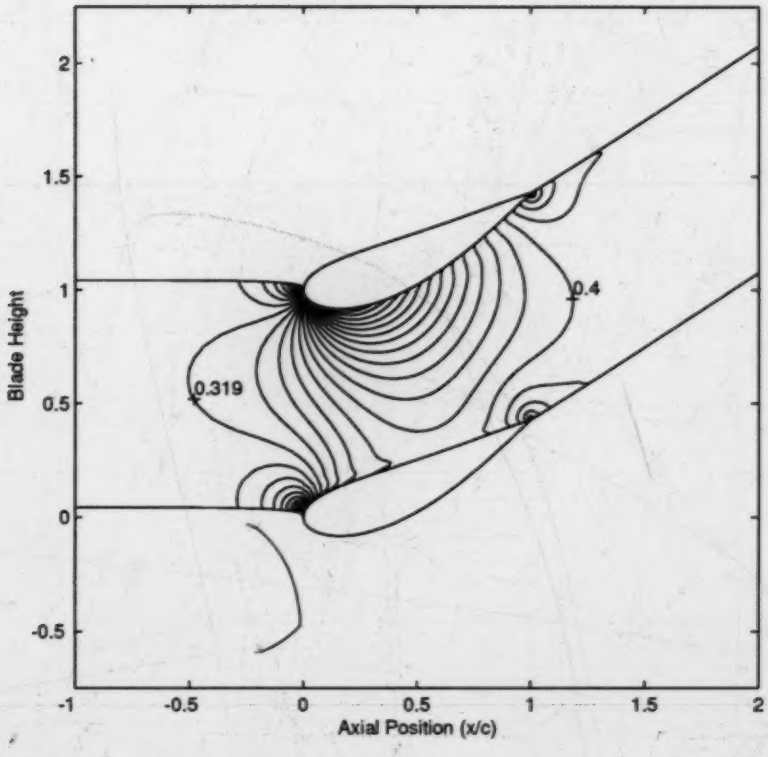

Figure 4.5: Contours of Mach Number in the Blade Passage

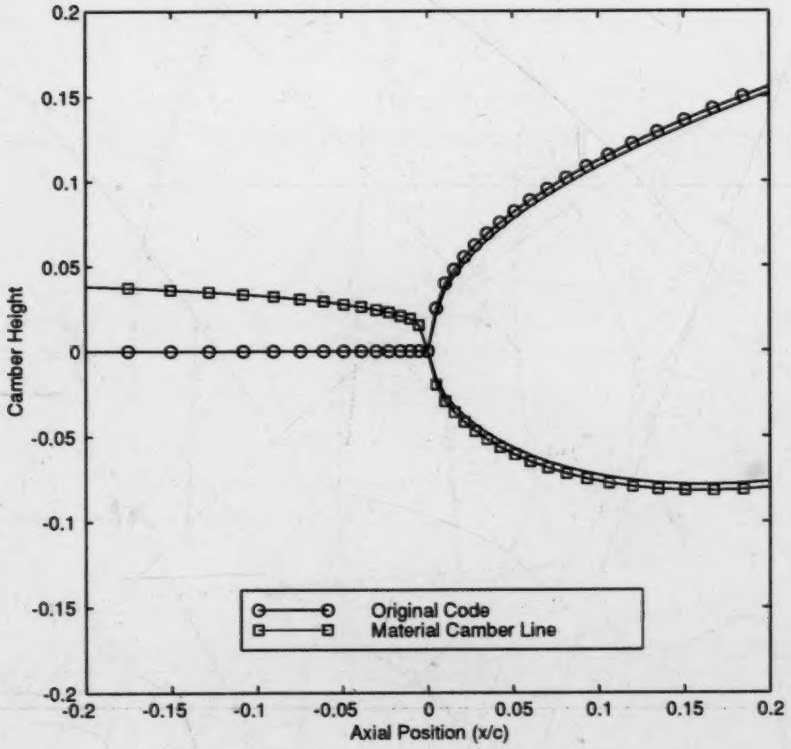

Figure 4.6: Comparison of the Upstream Grid Lines

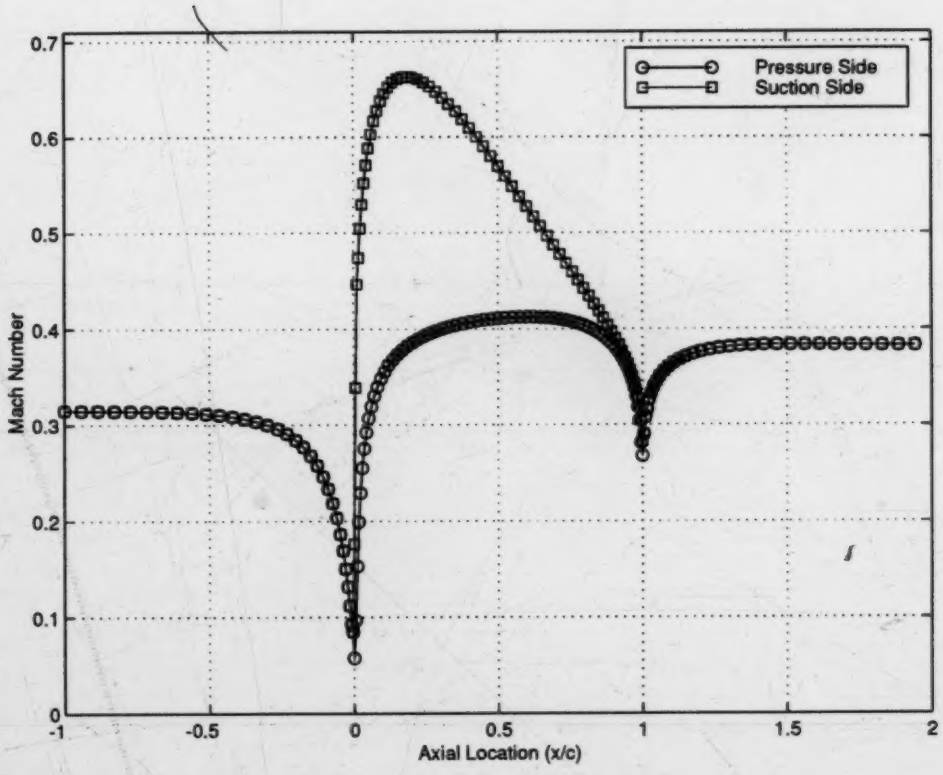

Figure 4.7: Mach Number on Blade Surfaces for the Material Camber Line

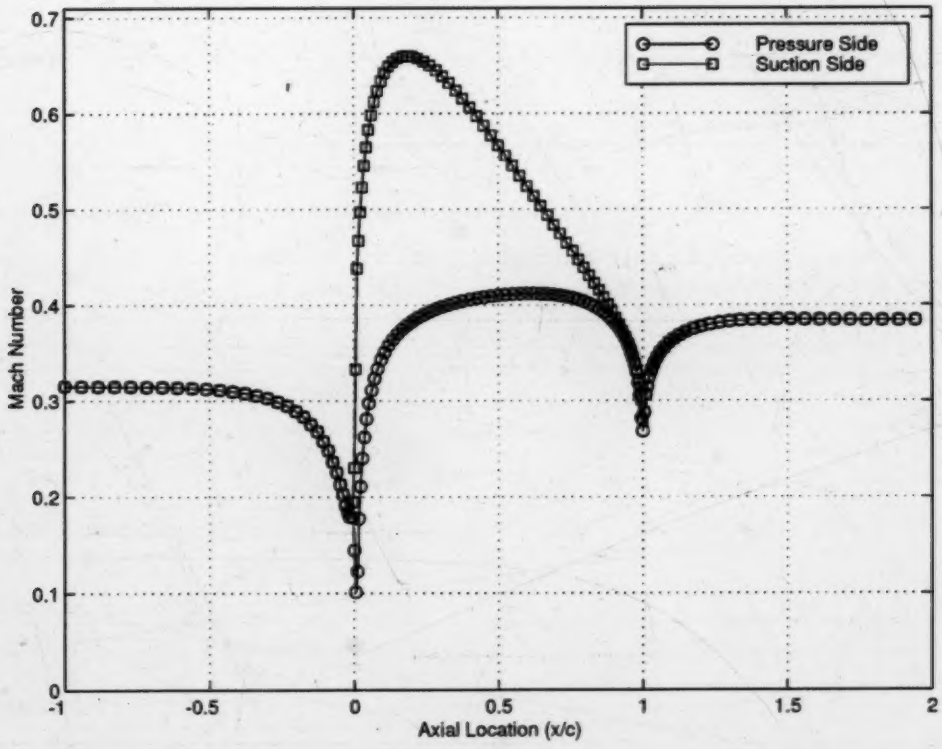

Figure 4.8: Mach Number on Blade Surfaces for the Original Camber Line

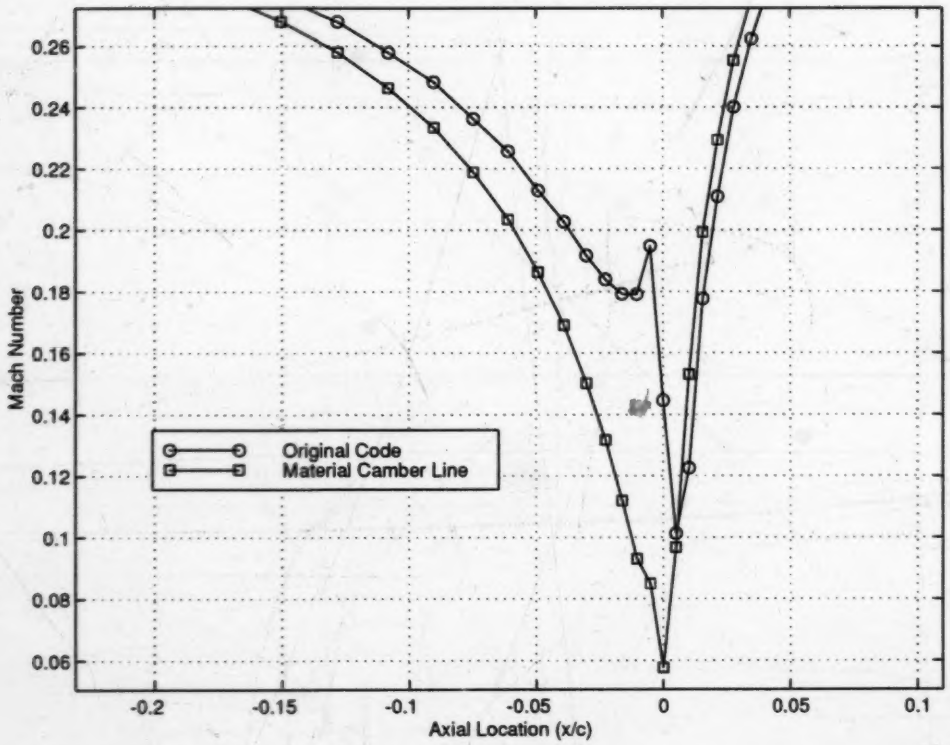

Figure 4.9: Comparison of Surface Mach Number on the Pressure Side

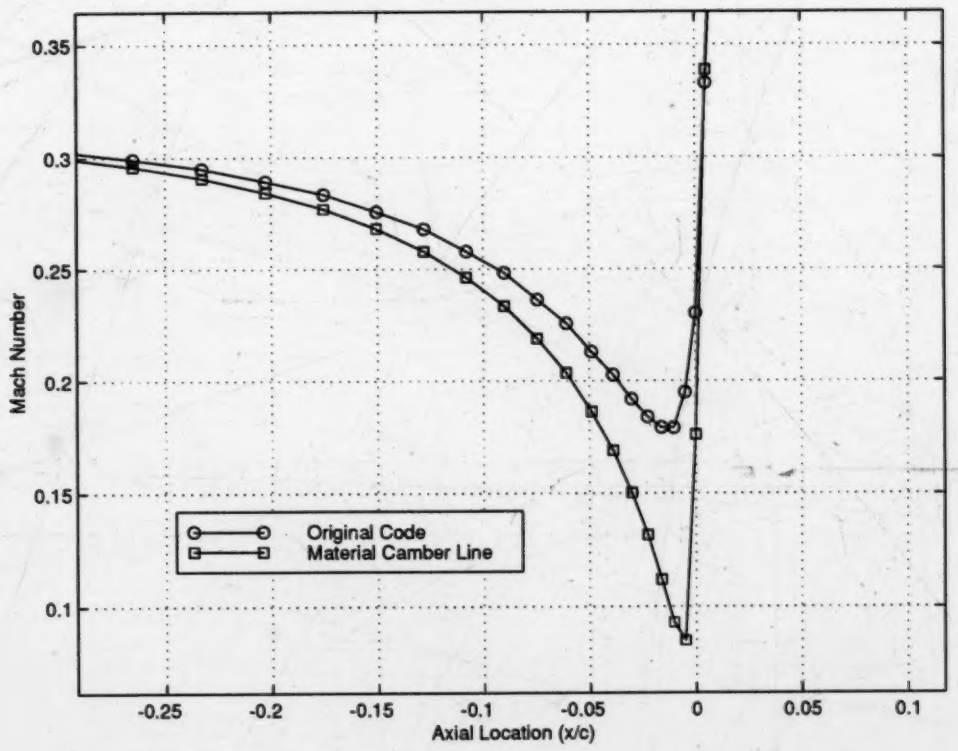

Figure 4.10: Comparison of Surface Mach Number on the Suction Side

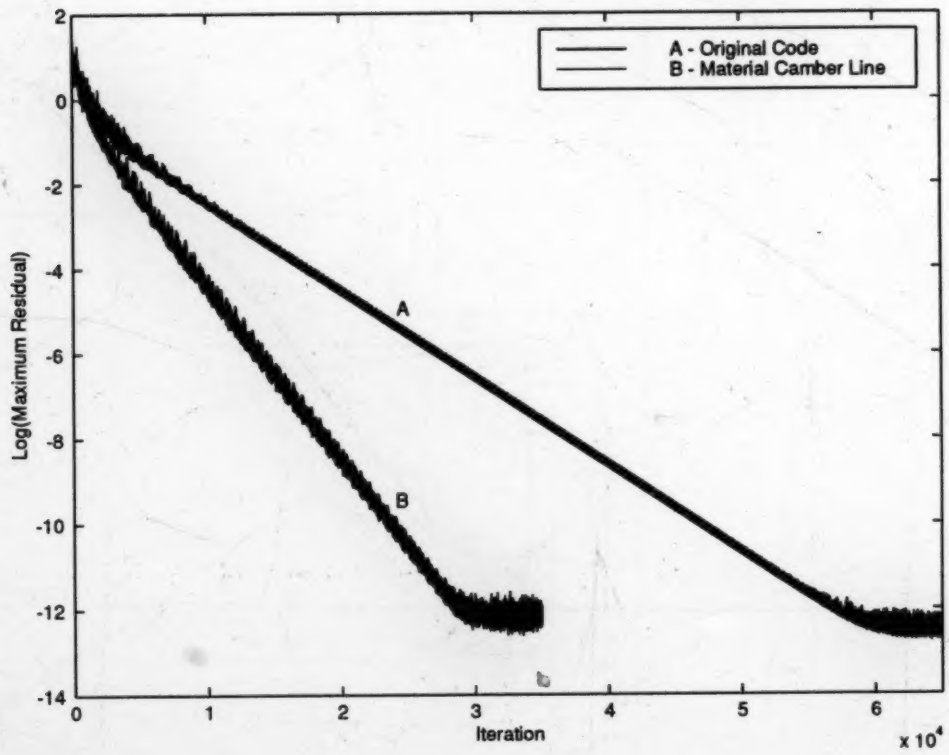

Figure 4.11: Convergence of Original and Material Camber Line Codes

4.1.2 Subsonic Testcase: Compressor Blade at Mach 0.5

The next subsonic case is a compressor blade designed to produce a mass flow of $\dot{m} = .443\frac{P_o C}{\sqrt{RT_o}}$ for a specified back pressure of $P = 0.85P_o$. The spacing to chord ratio is set $\frac{S}{C} = 0.9$ and the inlet flow angle at $\beta = 20°$. The turning distribution used is generated from $\frac{d\overline{v}}{dx} = Kx^m(1-x)^n$ where $m = \frac{1}{4}$ and $n = \frac{7}{4}$, with the total turning specified as $\Delta\overline{v} = -0.1\sqrt{RT_o}$ and is shown in Fig.(4.12). The thickness distribution used is shown in Fig.(4.13) with a maximum thickness to spacing ratio of $\frac{T_{max}}{S} = 0.15$, this blade has a rounded leading edge and a sharp trailing edge. This turning distribution produces the converged blade shown in Fig.(4.14) which corresponds to a total turning of 10°. The converged flow field is shown in Fig.(4.15).

The stagnation point is very close to the leading edge of this blade so that there is little difference between the two camber lines generated as seen in Fig.(4.16). The surface Mach numbers shown in Figs.(4.17) and (4.18) show that the two flow fields are very similar. Upon closer inspection of the leading edge, Figs.(4.19) and (4.20), there is very little difference between them. Since the straight line method happens to coincide with the material line, the leading edge Mach numbers are already well captured. Meaning, there are no overshoots or oscillations as in the previous case which caused errors in the leading edge region. Therefore the convergence associated with this blade is affected only slightly with the use of the material camber generator as seen in Fig.(4.21).

Text resumes on page 84

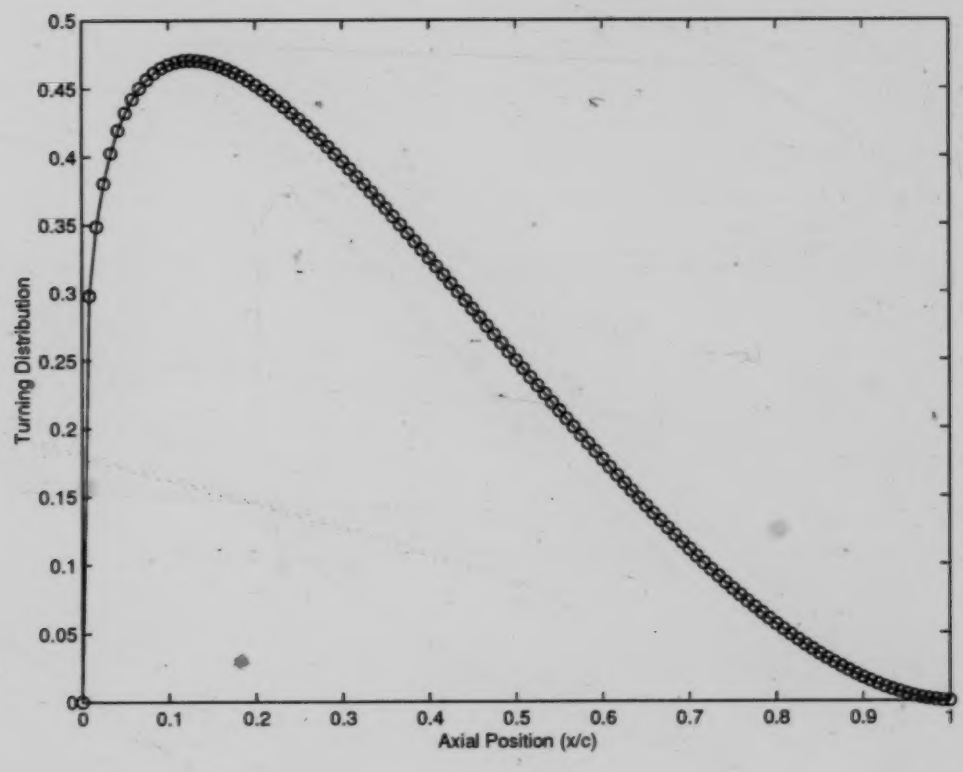

Figure 4.12: Specified Turning Distribution for the Mach 0.5 Compressor Blade

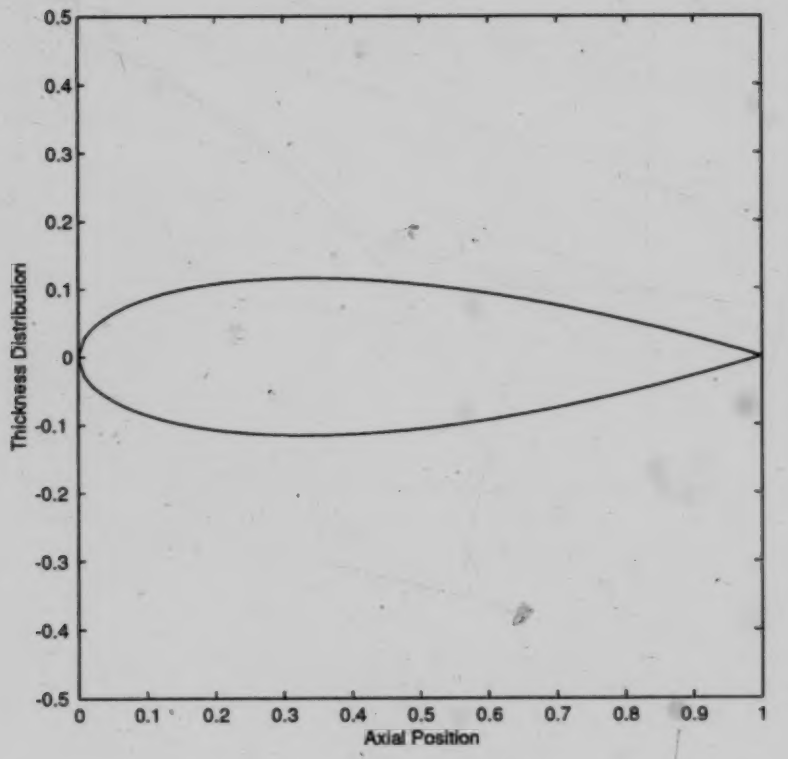

Figure 4.13: Specified Thickness Distribution for the Mach 0.5 Compressor Blade

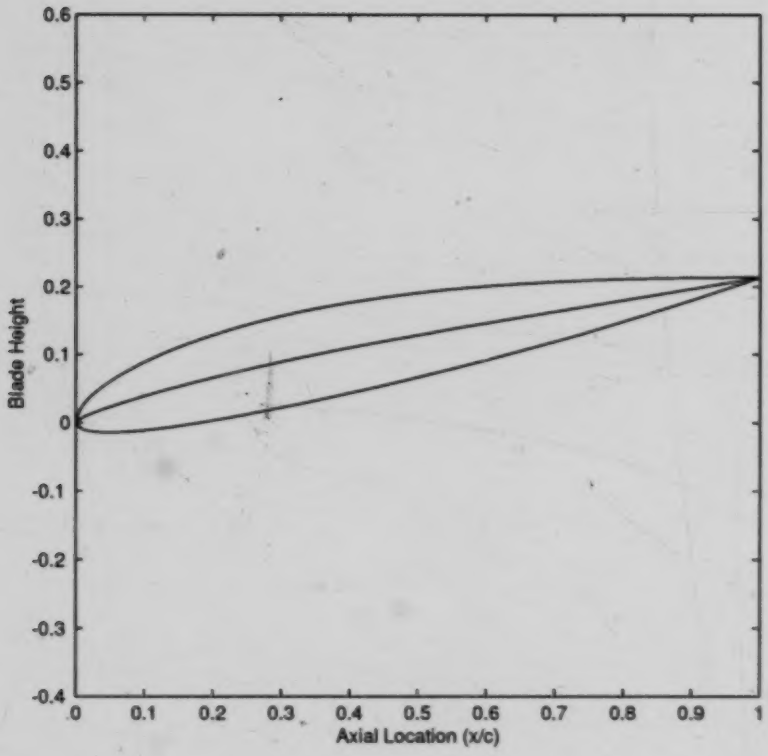

Figure 4.14: Converged Blade shape for the Mach 0.5 Compressor Blade

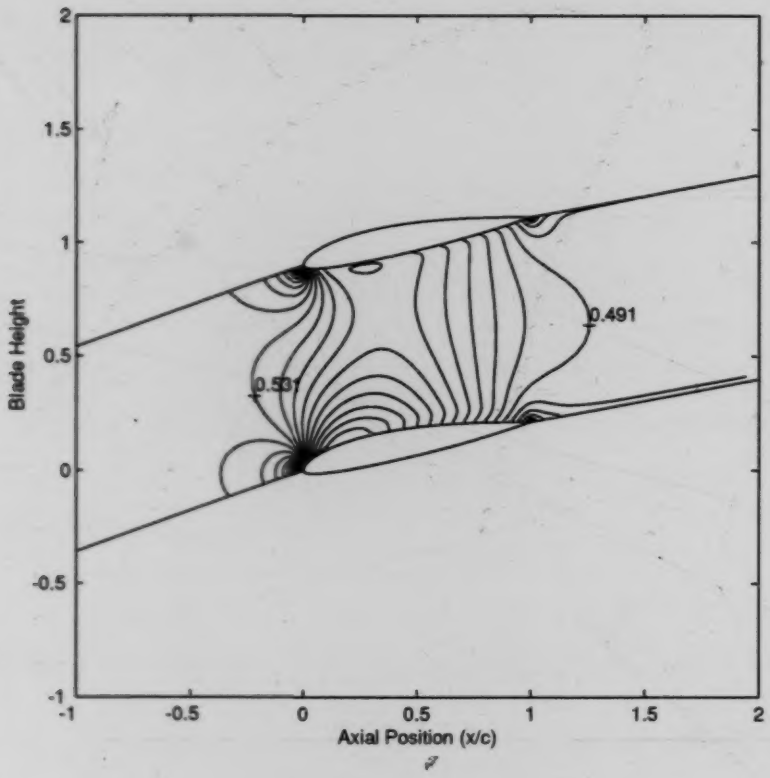

Figure 4.15: Contours of Mach Number in the Blade Passage

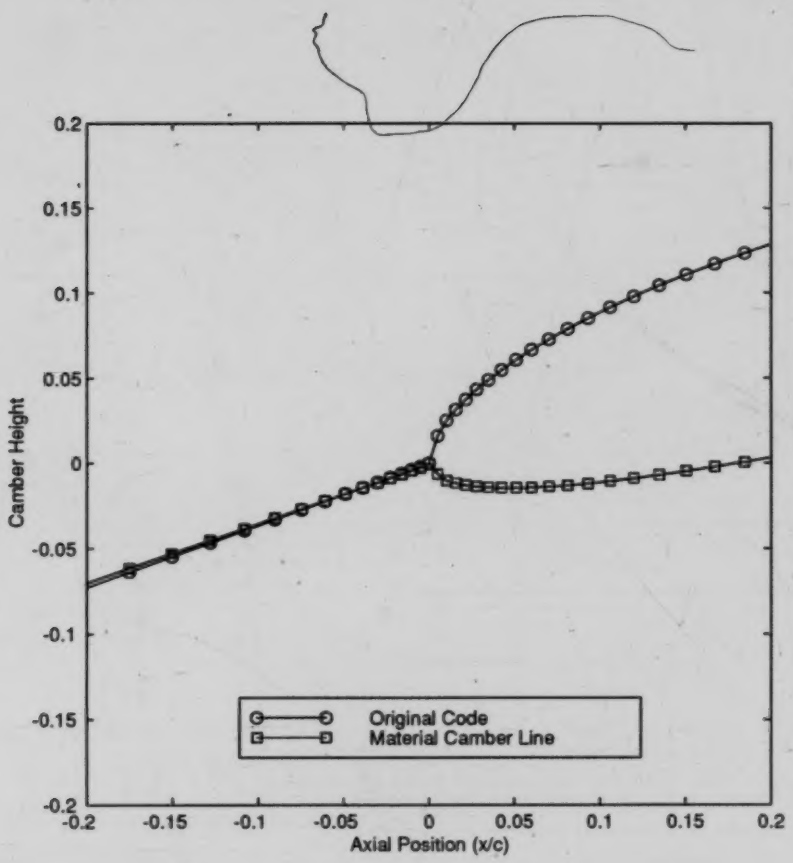

Figure 4.16: Comparison of the Upstream Grid Lines

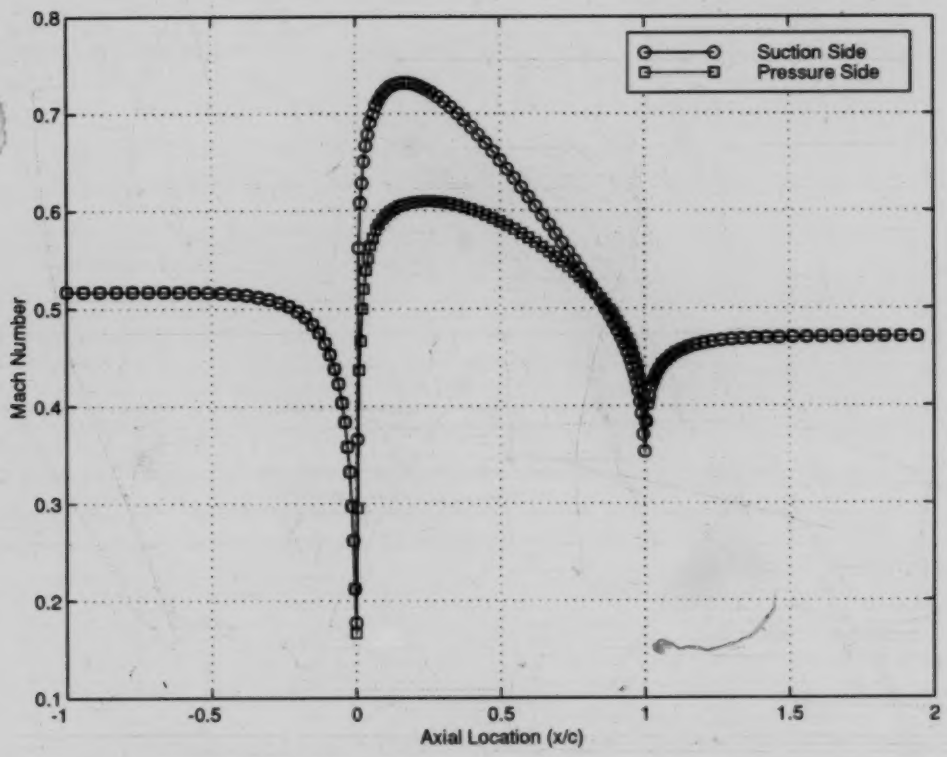

Figure 4.17: Mach Number on Blade Surfaces for the Material Camber Line

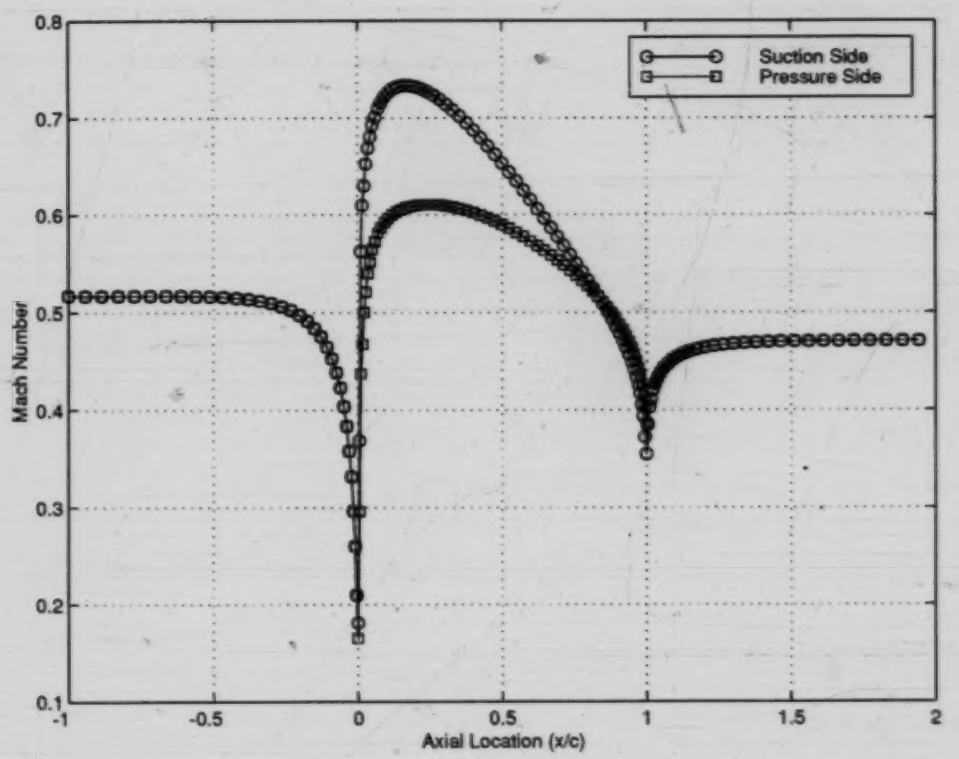

Figure 4.18: Mach Number on Blade Surfaces for the Original Camber Line

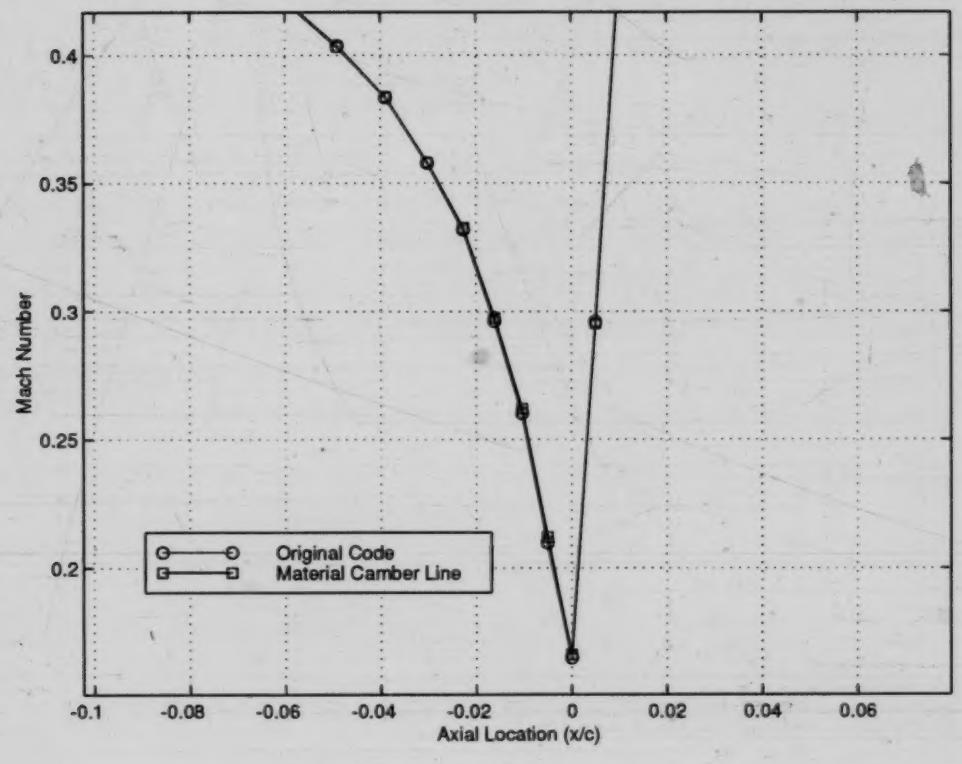

Figure 4.19: Comparison of Surface Mach Number on the Suction Side

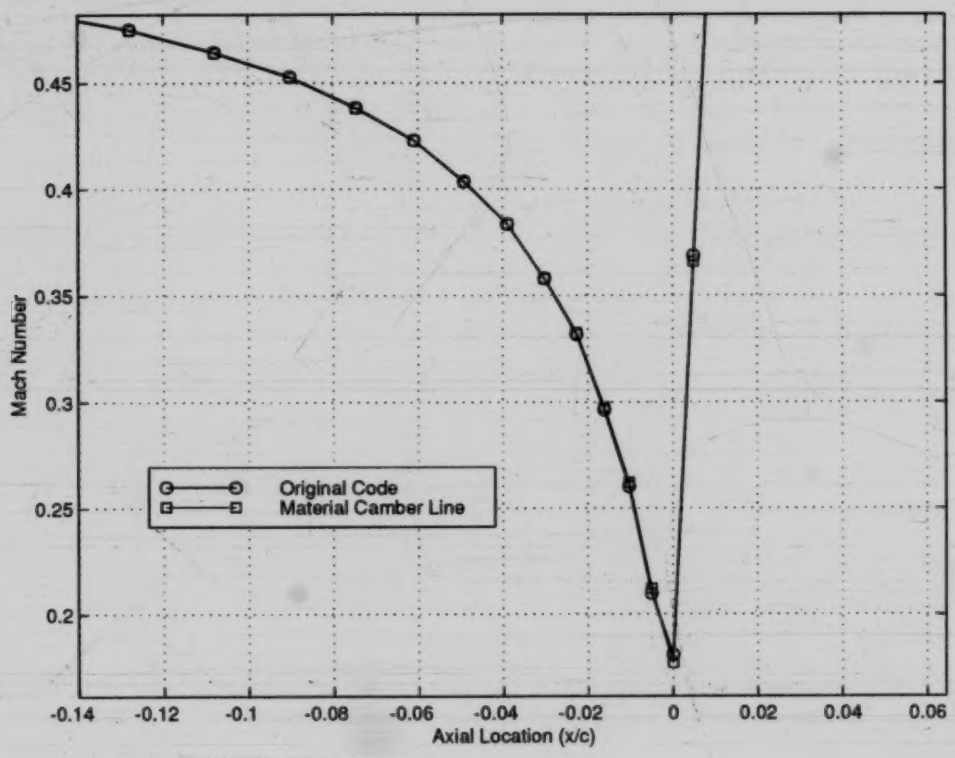

Figure 4.20: Comparison of Surface Mach Number on the Pressure Side

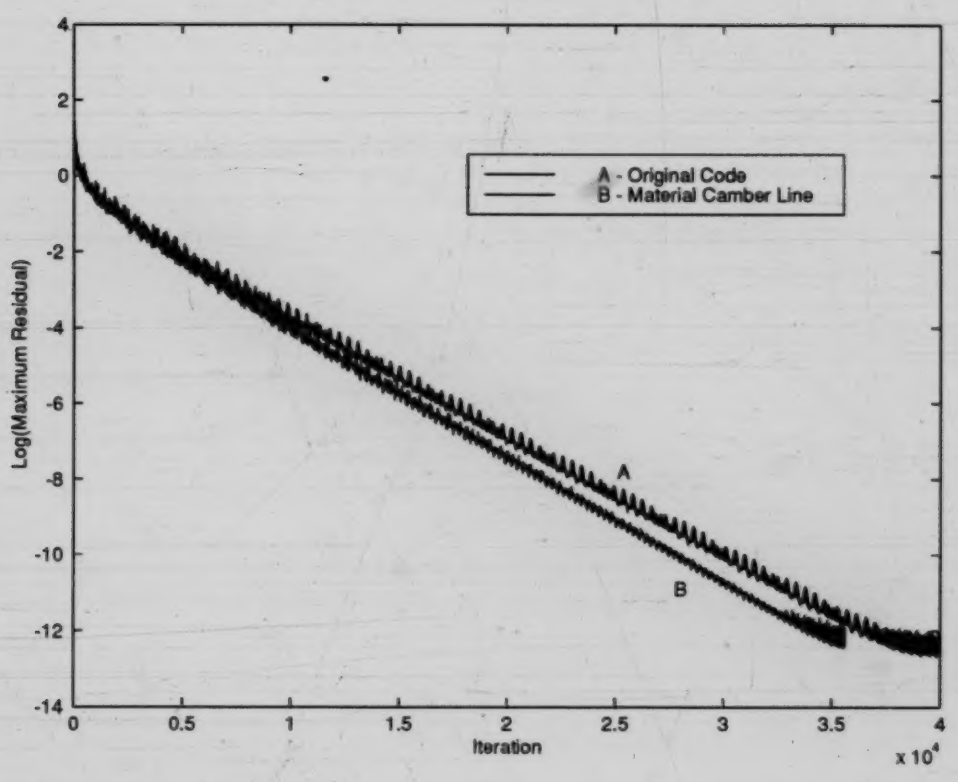

Figure 4.21: Convergence of Original and Material Camber Line Codes

4.1.3 Transonic Testcase: Turbine Blade

The next case is a transonic turbine blade designed to produce a mass flow of $\dot{m} = .228\frac{P_o C}{\sqrt{RT_o}}$ for a specified back pressure of $P = 0.53P_o$. The spacing to chord ratio is set $\frac{S}{C} = 0.5$ and the inlet flow angle at $\beta = 15°$. The turning distribution used is generated from $\frac{d\overline{v}}{dx} = Kcos(\frac{\pi x}{2})$, with the total turning specified as $\Delta\overline{v} = -0.933\sqrt{RT_o}$ and is shown in Fig.(4.22). The thickness distribution used is shown in Fig.(4.23) with a maximum thickness to spacing ratio of $\frac{T_{max}}{S} = 0.25$. This turning distribution produces the converged blade shown in Fig.(4.24) which corresponds to a total turning of 61°. The converged flow field is shown in Fig.(4.25).

The effect that the material camber line has on the flow field accuracy and convergence acceleration is not restricted to subsonic flows. In this transonic case, the material line is significantly different than the straight line method as shown in Fig.(4.26). The difference is smaller than that of the first subsonic case so, the effect will be smaller but still present. Upon inspection of Figs.(4.27) and (4.28), it can be seen that a similar problem exists at the leading edge. Looking at the detail views of the comparisons between the two methods, Figs.(4.29) and (4.30), the same overshoot is present on the original blade, where as, the Mach numbers on the material line case come into the leading edge smoothly. Again, as expected, the convergence of the new treatment cuts the time to converge from 55000 iterations to 32000, which is a significant reduction in computational time.

Text resumes on page 95

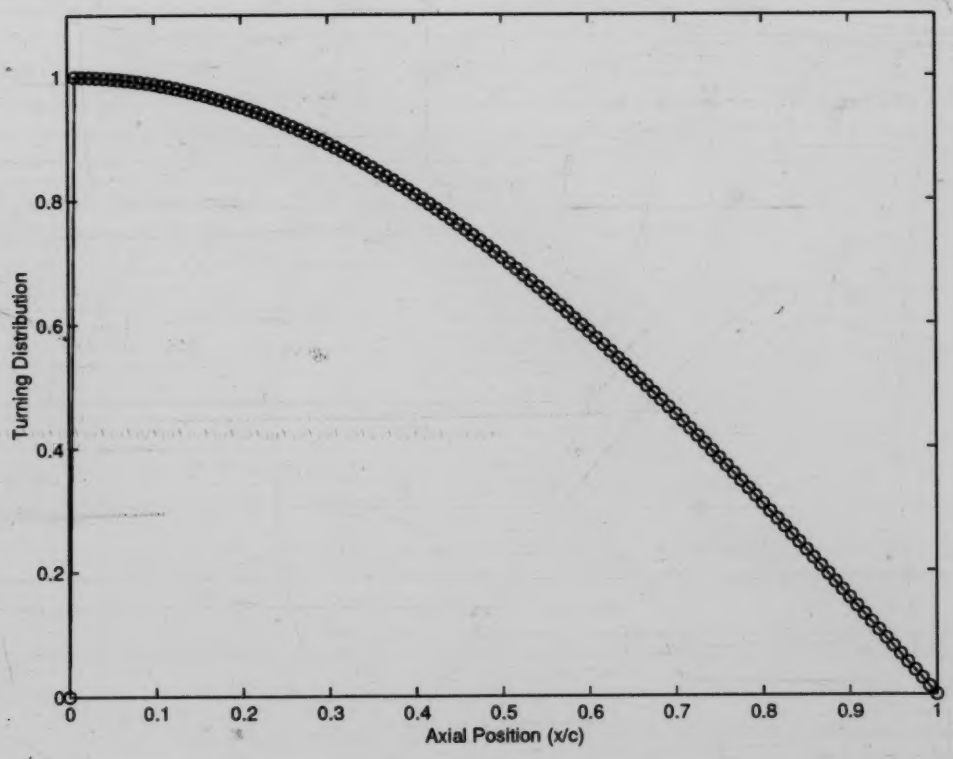

Figure 4.22: Specified Turning Distribution for the Transonic Turbine Blade

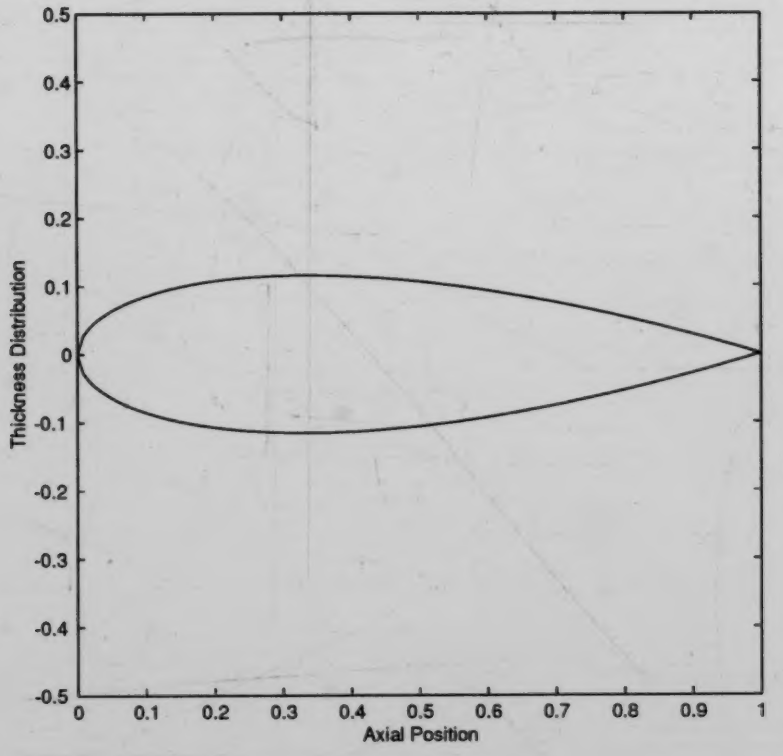

Figure 4.23: Specified Thickness Distribution for the Transonic Turbine Blade

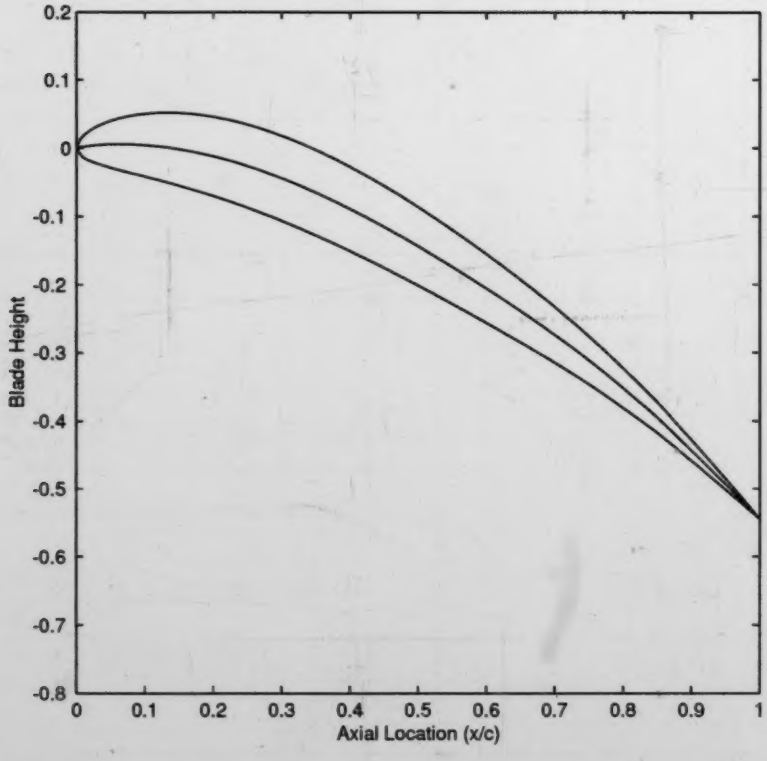

Figure 4.24: Converged Blade shape for the Transonic Turbine Blade

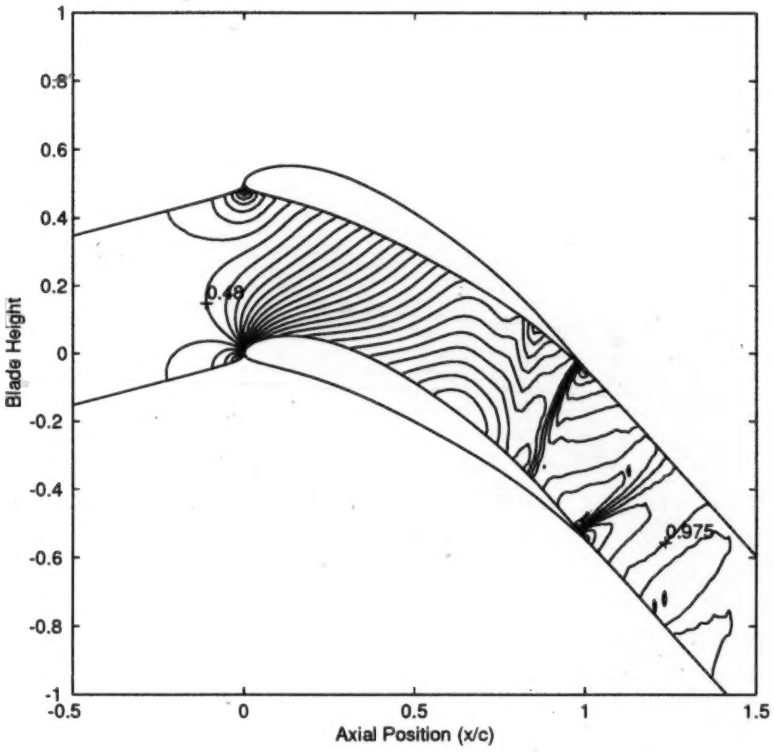

Figure 4.25: Contours of Mach Number in the Blade Passage

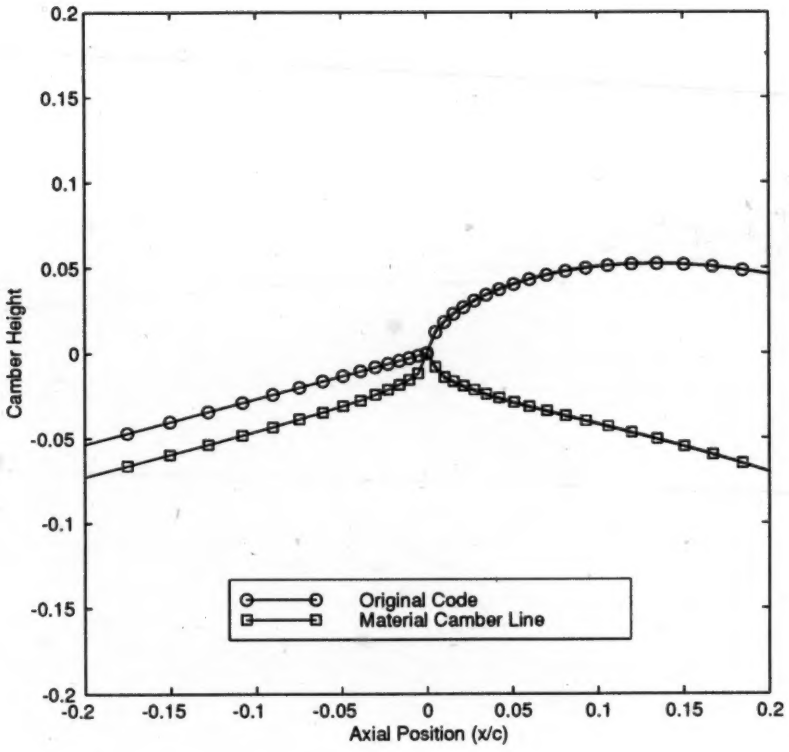

Figure 4.26: Comparison of the Upstream Grid Lines

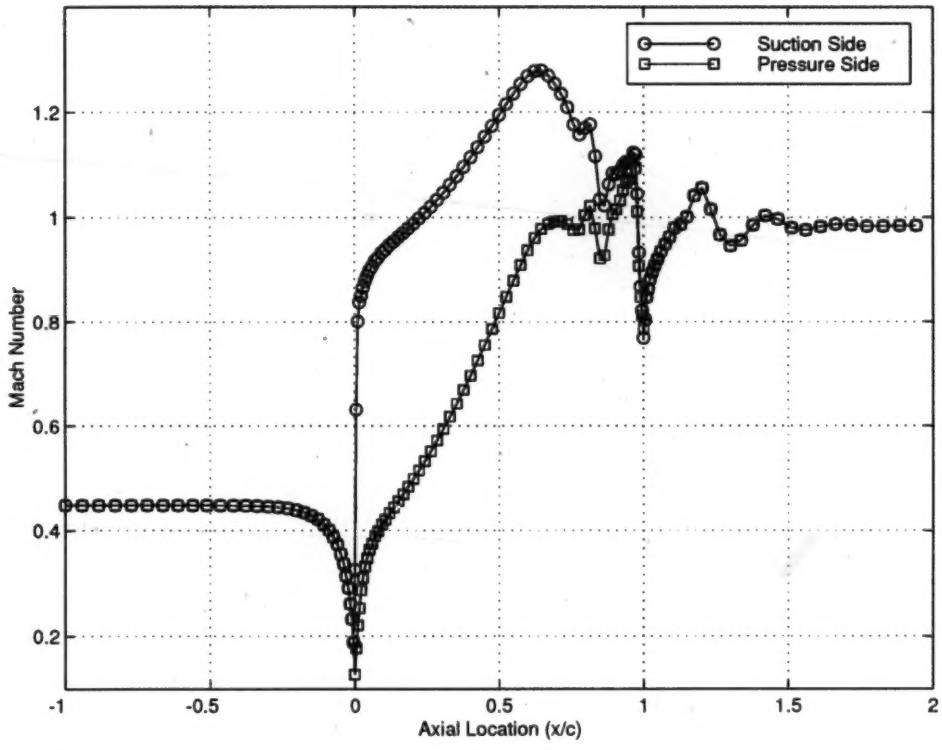

Figure 4.27: Mach Number on Blade Surfaces for the Material Camber Line

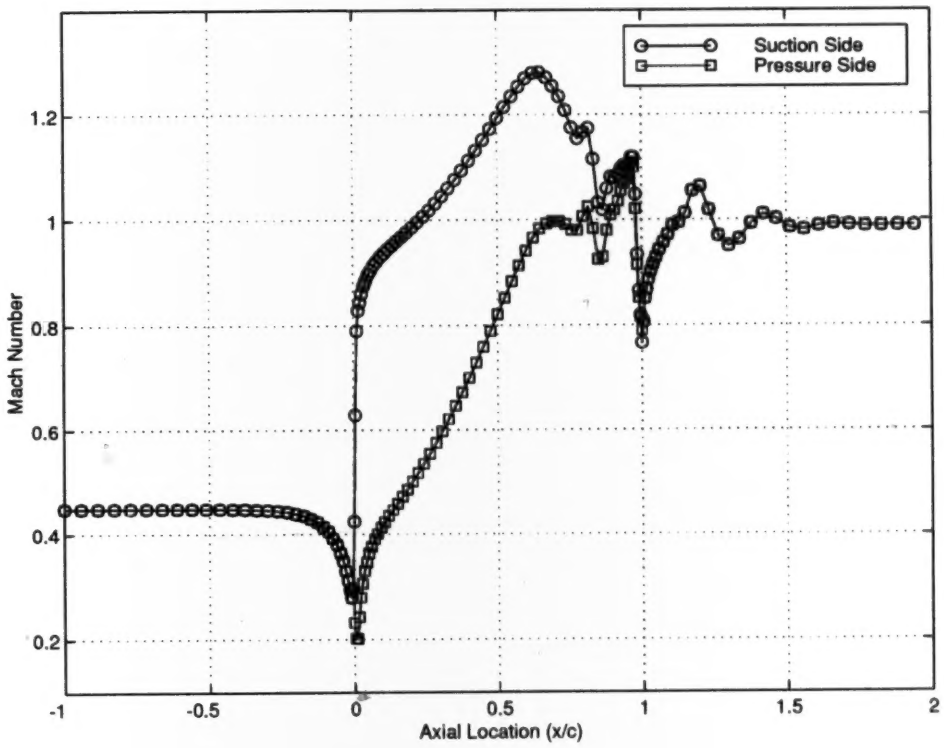

Figure 4.28: Mach Number on Blade Surfaces for the Original Camber Line

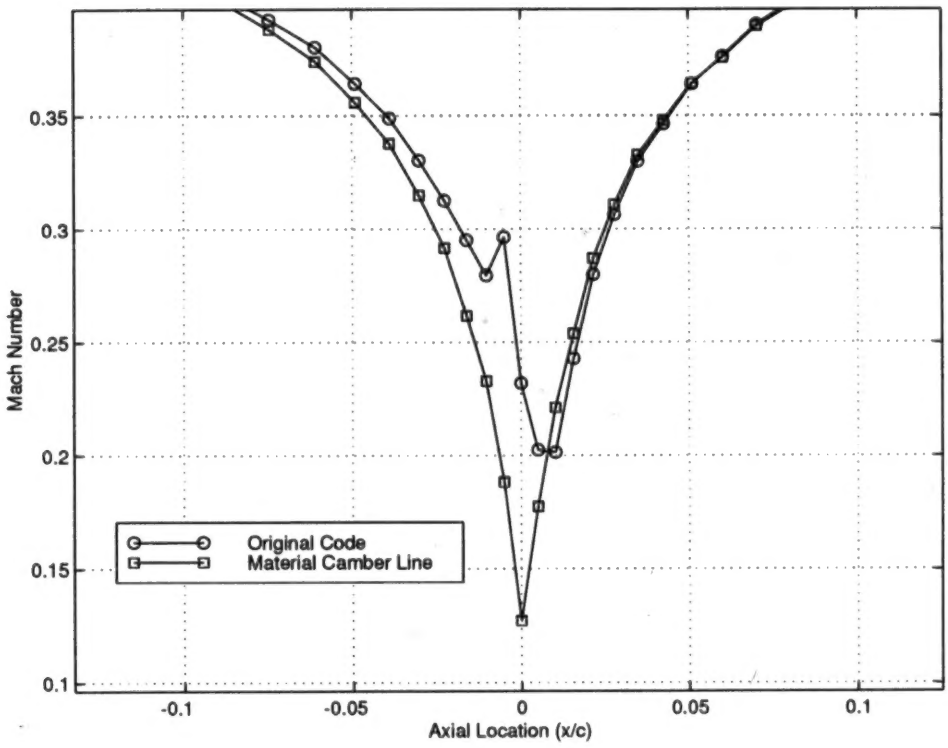

Figure 4.29: Comparison of Surface Mach Number on the Pressure Side

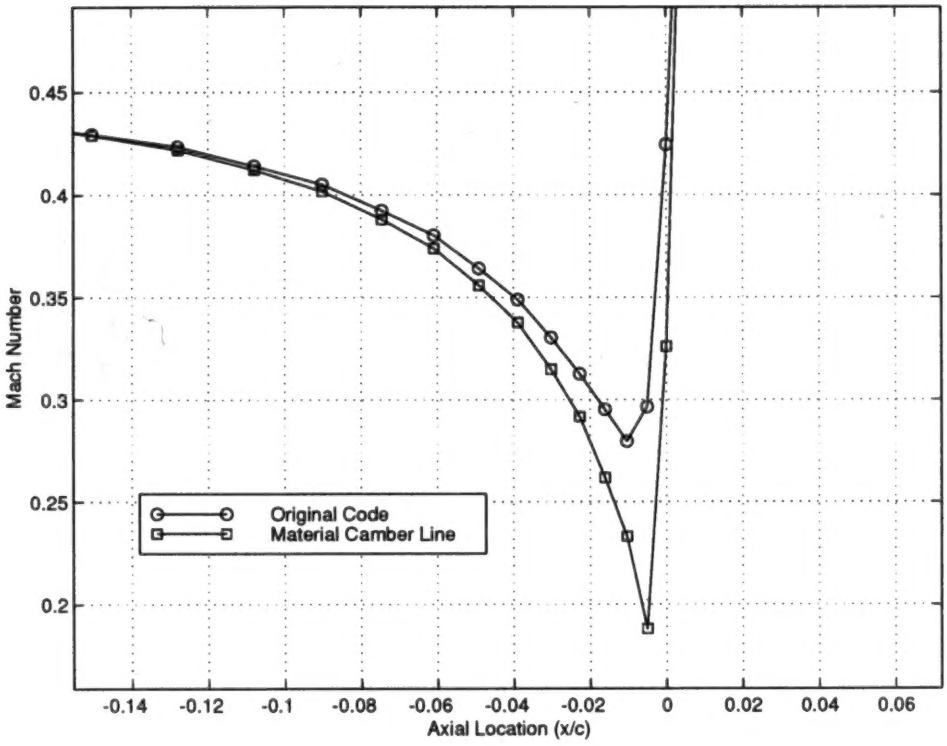

Figure 4.30: Comparison of Surface Mach Number on the Suction Side

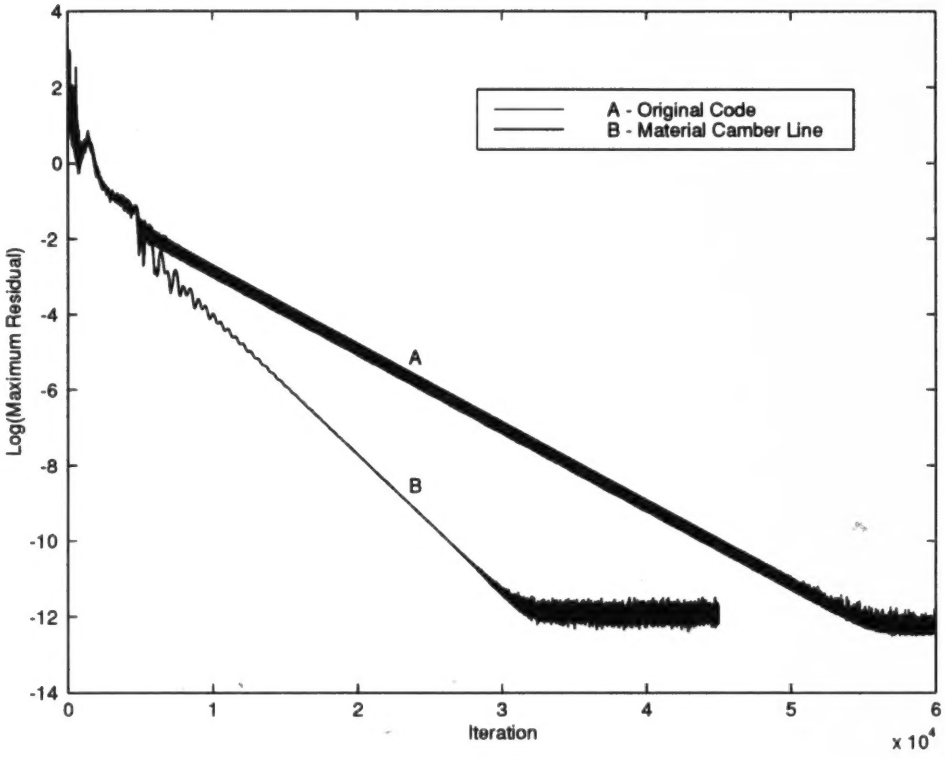

Figure 4.31: Convergence of Original and Material Camber Line Codes

4.1.4 Supersonic Testcase: Compressor Blade

The next case is a fully supersonic compressor blade designed to produce a mass flow of $\dot{m} = .147\frac{P_o C}{\sqrt{RT_o}}$ for a specified inlet Mach number of $M = 1.7$. The spacing to chord ratio is set $\frac{S}{C} = 0.35$ and the inlet flow angle at $\beta = 35°$. The turning distribution used is generated from $\frac{d\overline{v}}{dx} = Kx^m(1-x)^n$ where $m = 1$ and $n = 1$, with the total turning specified as $\Delta\overline{v} = -0.833\sqrt{RT_o}$ and is shown in Fig.(4.32). The thickness distribution used is shown in Fig.(4.33) with a maximum thickness to spacing ratio of $\frac{T_{max}}{S} = 0.15$, this blade has sharp leading and trailing edges. This turning distribution produces the converged blade shown in Fig.(4.34) which corresponds to a total turning of 29°. The converged flow field is shown in Fig.(4.35).

This case was done because there is no upstream effect in supersonic flow. To verify the previous results, both the original straight line method and the new material camber line method should produce identical results because the straight line is already the material line. The two grid lines upstream can be seen to be identical from Fig.(4.36) as was expected. The surface plots of Figs.(4.37), (4.37), (4.37) and (4.37) also show the identical results. Therefore, the convergence of the straight line method can not be improved by the new material line method. In fact the material line method took 3.5 % longer, 2900 iterations instead of 2800 iterations to reduce the error by 13 orders of magnitude.

The material camber line generator has shown to be very effective in flows where the stagnation point moves off of the geometric center of the blades leading edge. This includes both subsonic and transonic flows but excludes all supersonic flows because there is no upstream affect present to shift the stagnation point. The straight line method, in supersonic flow is already the material line upstream of the blade and can not be improved using this new technique.

Text resumes on page 106

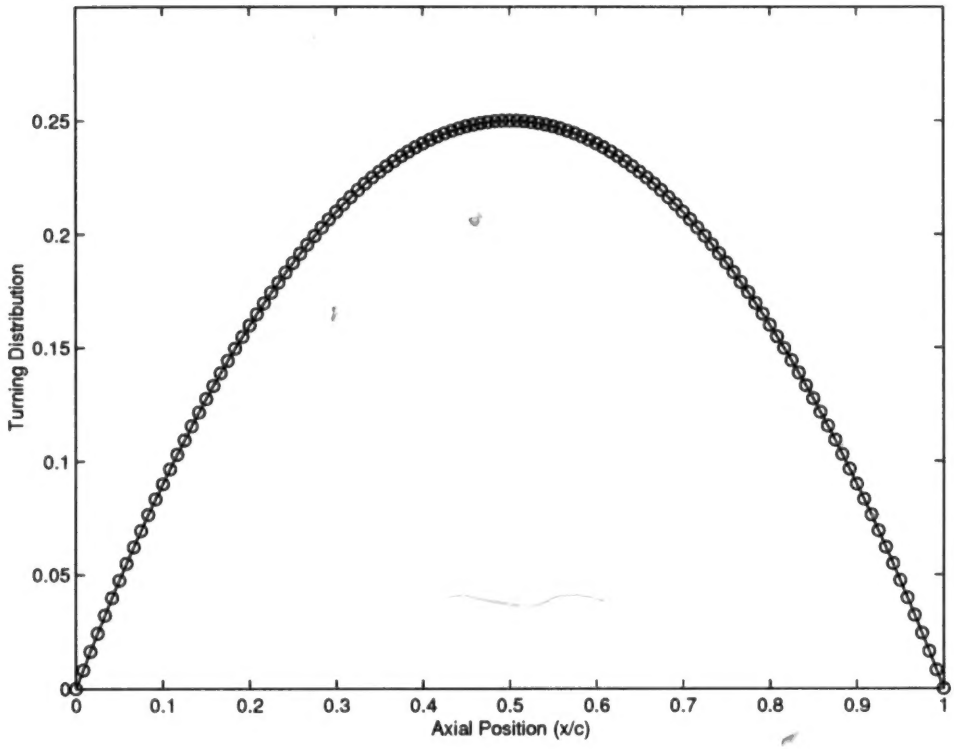

Figure 4.32: Specified Turning Distribution for the Supersonic Compressor Blade

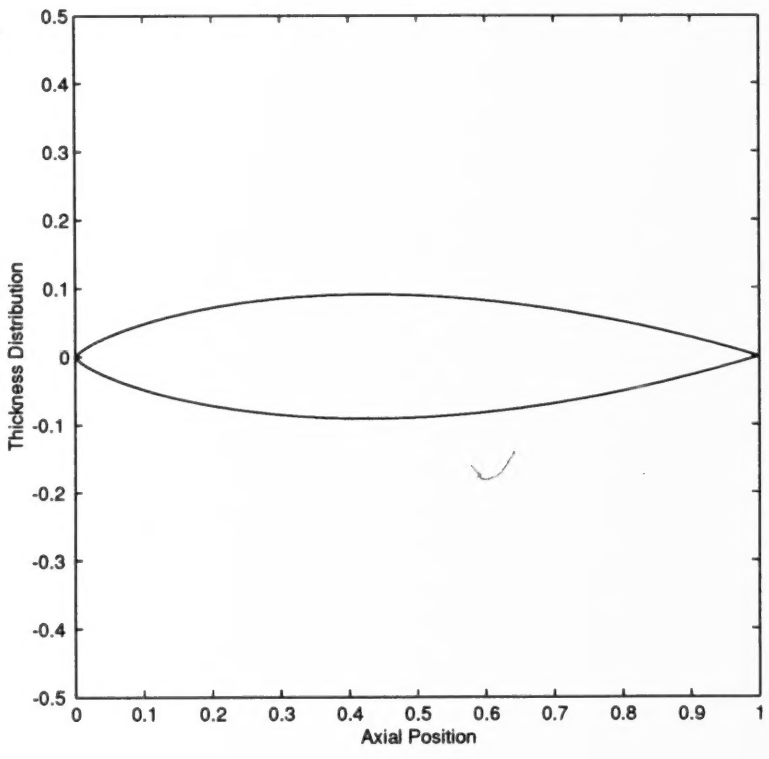

Figure 4.33: Specified Thickness Distribution for the Supersonic Compressor Blade

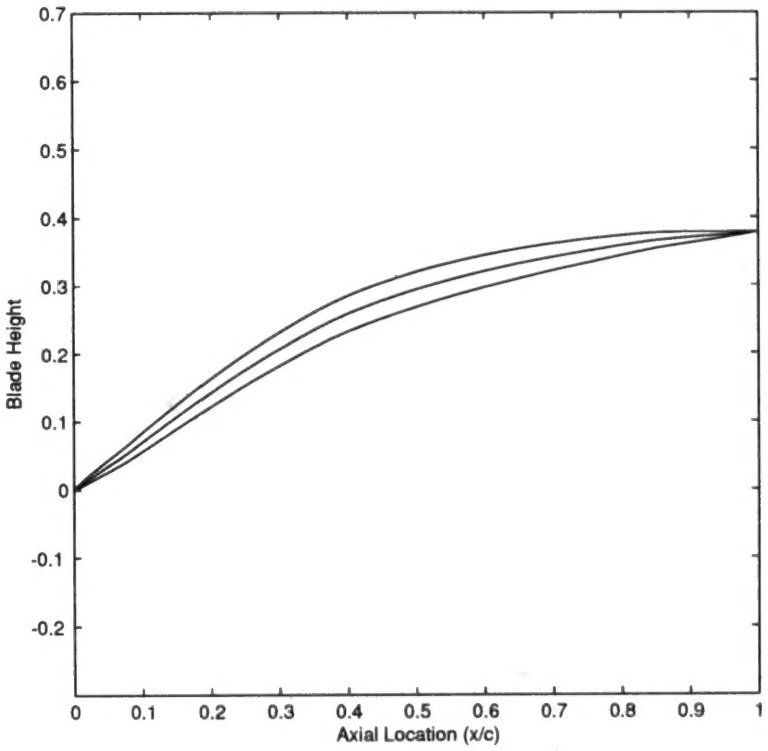

Figure 4.34: Converged Blade shape for the Supersonic Compressor Blade

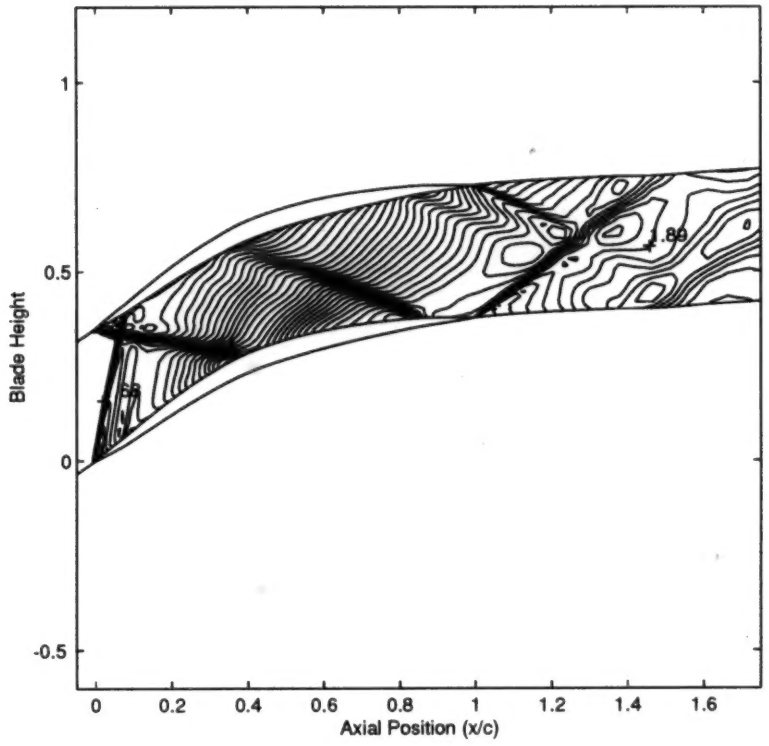

Figure 4.35: Contours of Mach Number in the Blade Passage

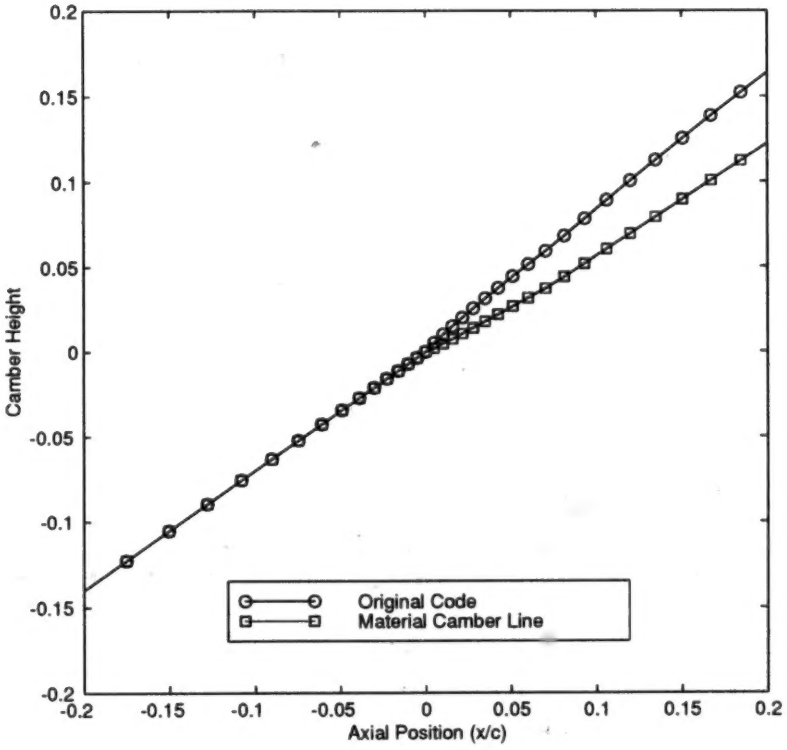

Figure 4.36: Comparison of the Upstream Grid Lines

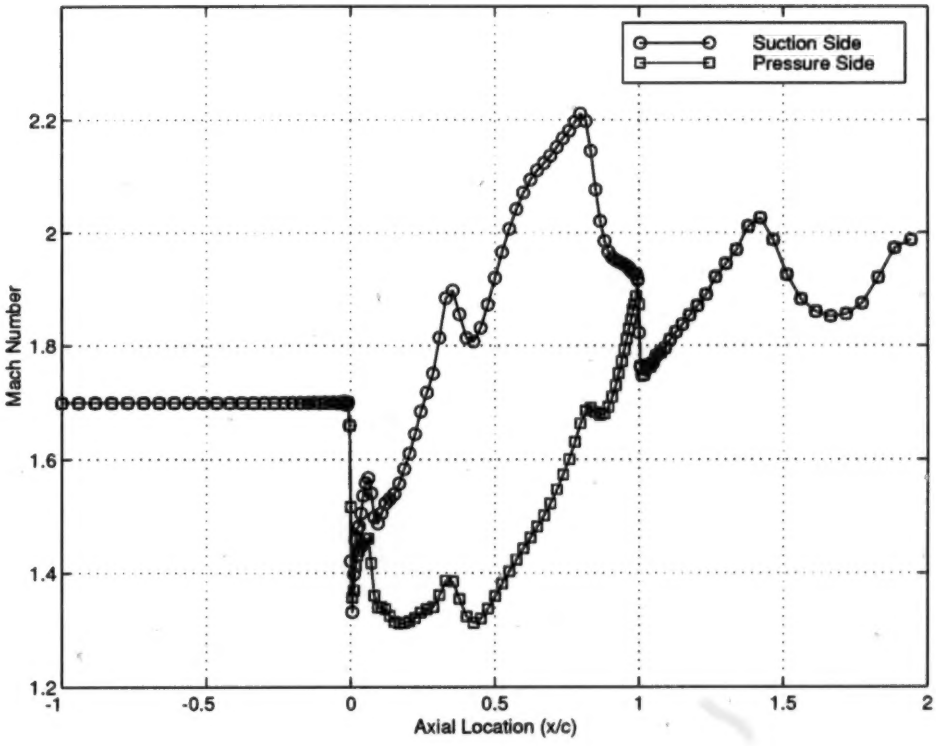

Figure 4.37: Mach Number on Blade Surfaces for the Material Camber Line

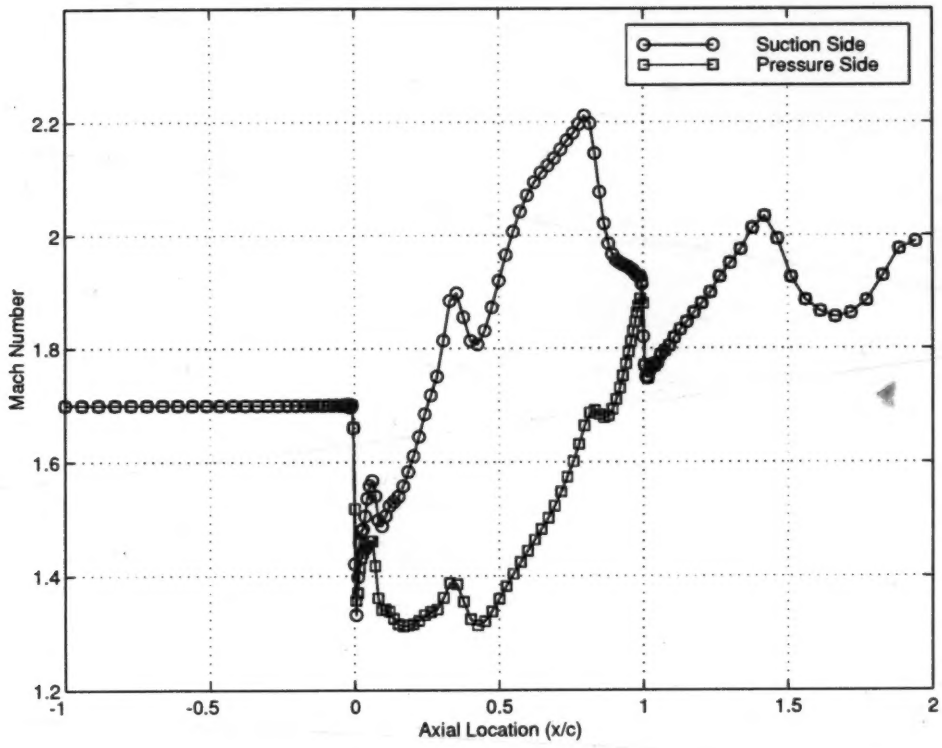

Figure 4.38: Mach Number on Blade Surfaces for the Original Camber Line

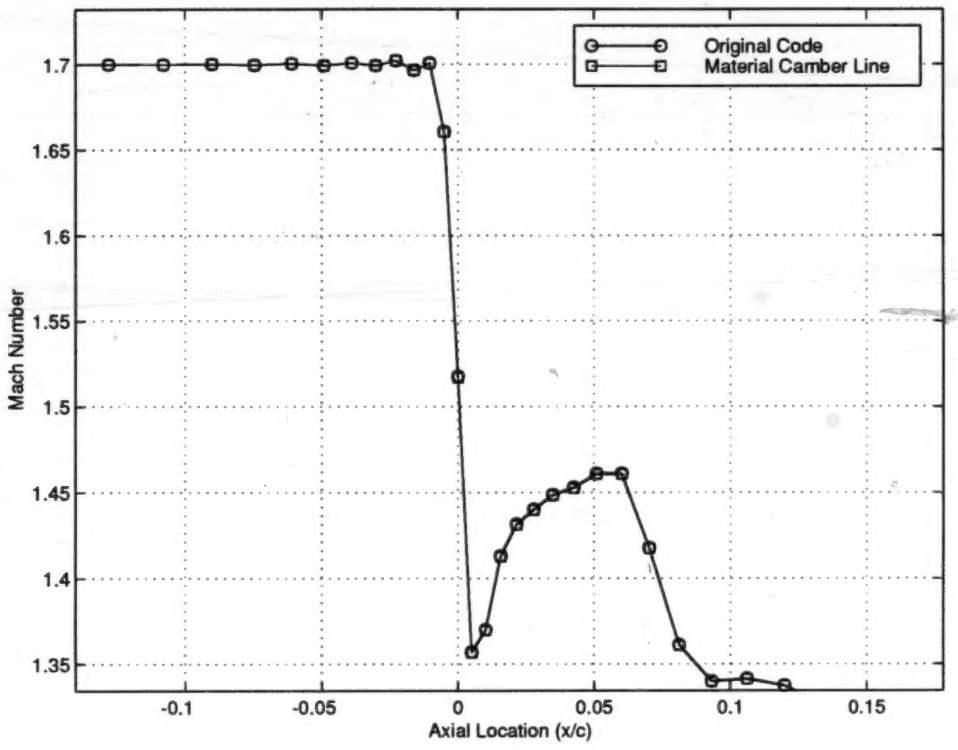

Figure 4.39: Comparison of Surface Mach Number on the Pressure Side

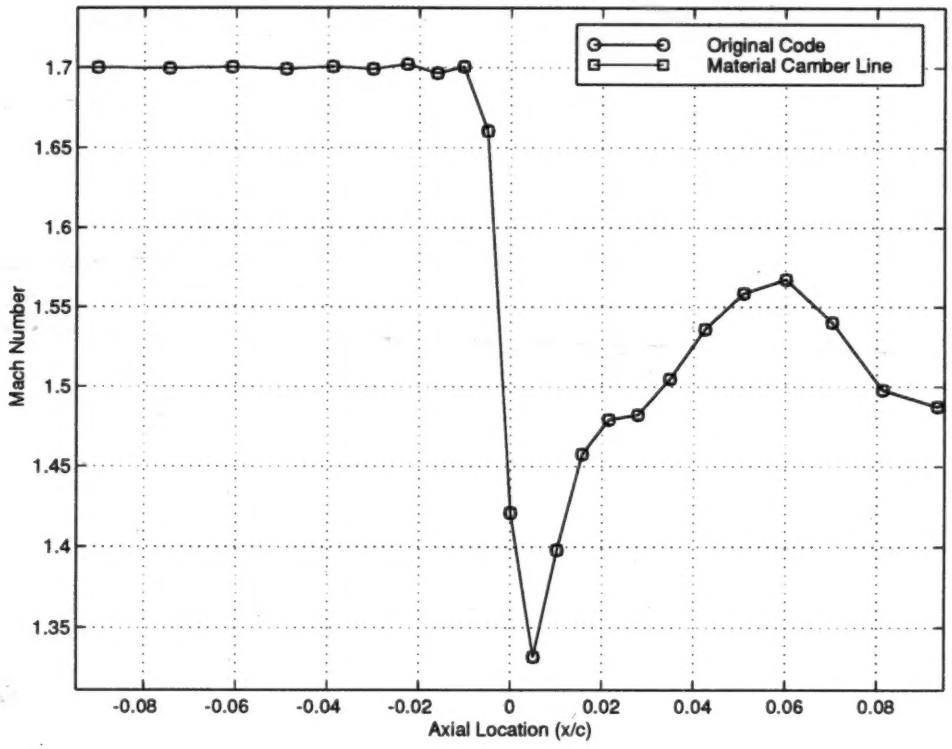

Figure 4.40: Comparison of Surface Mach Number on the Suction Side

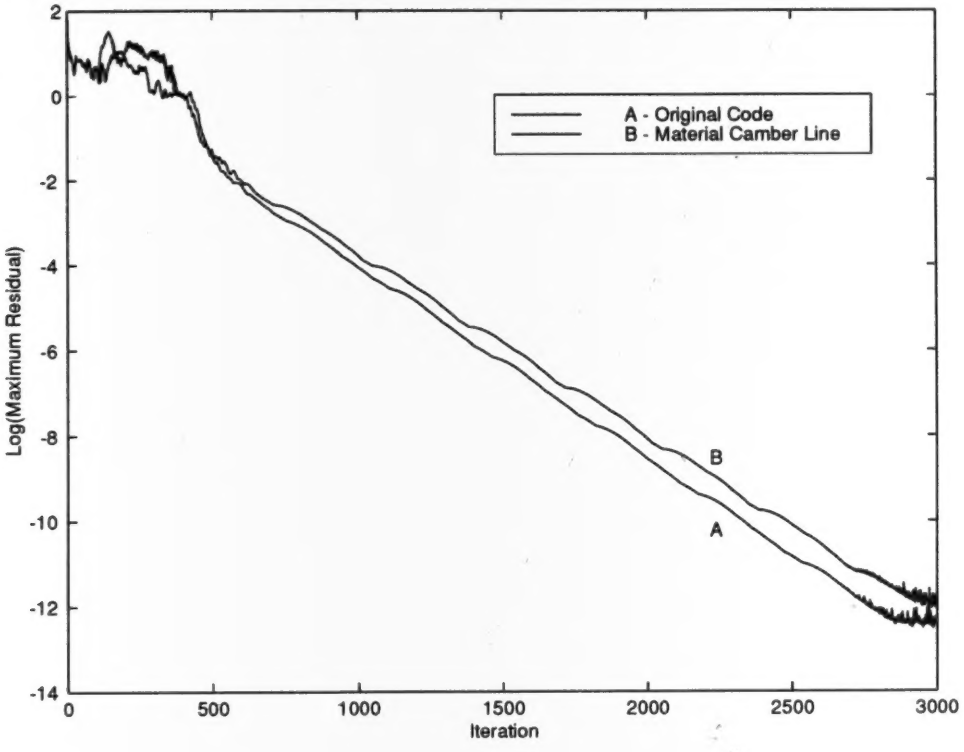

Figure 4.41: Convergence of Original and Material Camber Line Codes

4.2 Unsteady Pressure Treatment

This test case is presented as more evidence of the effectiveness of the material camber line generator and also the effect of including the unsteady pressure term in the pressure boundary condition. This calculation was also performed on a sheared H-type mesh. The numerical domain consists of 128 X 32 cells with 64 cells in the bladed region. The domain was extended one chord upstream and downstream of the leading and trailing edges, respectively. Grid lines were clustered near the leading and trailing edges in the x-direction and near the blade surfaces in the y-direction.

4.2.1 Subsonic Testcase: Turbine Blade at Mach 0.5

The next subsonic case is a low mach number turbine blade designed to produce a mass flow of $\dot{m} = .417\frac{P_o C}{\sqrt{RT_o}}$ for a specified back pressure of $P = 0.85P_o$. The spacing to chord ratio is $\frac{S}{C} = 0.9$ and the inlet flow angle is set at $\beta = 20°$. The turning distribution used is generated from $\frac{d\overline{v}}{dx} = Kcos(\frac{\pi x}{2})$, with the total turning specified as $\Delta\overline{v} = -0.4\sqrt{RT_o}$ and is shown in Fig.(4.42). The thickness distribution used is shown in Fig.(4.43) with a maximum thickness to spacing ratio of $\frac{T_{max}}{S} = 0.15$. This turning distribution produces the converged blade shown in Fig.(4.44) which corresponds to a total turning of 44°. The converged flow field is shown in Fig.(4.45).

Originally a formal derivation of the unsteady pressure boundary condition was needed to develop the transonic design pressure boundary condition. The unsteady pressure boundary, however has proven to be helpful in convergence acceleration.

This test case further supports the material camber line method in that it produces results expected from the analysis of the previous testcases. The stagnation point on this blade has not moved off of the leading edge as much as the previous test case hence, a smaller difference is expected between the upstream grid lines. This is indeed the case, as shown in Fig.(4.46). This also suggests that, because the

original grid line is closer to the material line that the error in Mach number at the leading edge is also smaller. The Mach numbers on the surfaces of the two blades are shown in Figs.(4.47) and (4.48). Again, there is a problem at the leading edge. Although, as shown in Figs.(4.49) and (4.50), the difference is much smaller than the first case presented. The convergence plot of Fig.(4.51) shows a substantial decrease in computational time, 85000 iterations down to 55000 iterations. Also, by comparing the convergence for the material camber line method and the material camber line method plus the unsteady pressure boundary condition the time was decreased further to 42000 iterations.

Text resumes on page 118

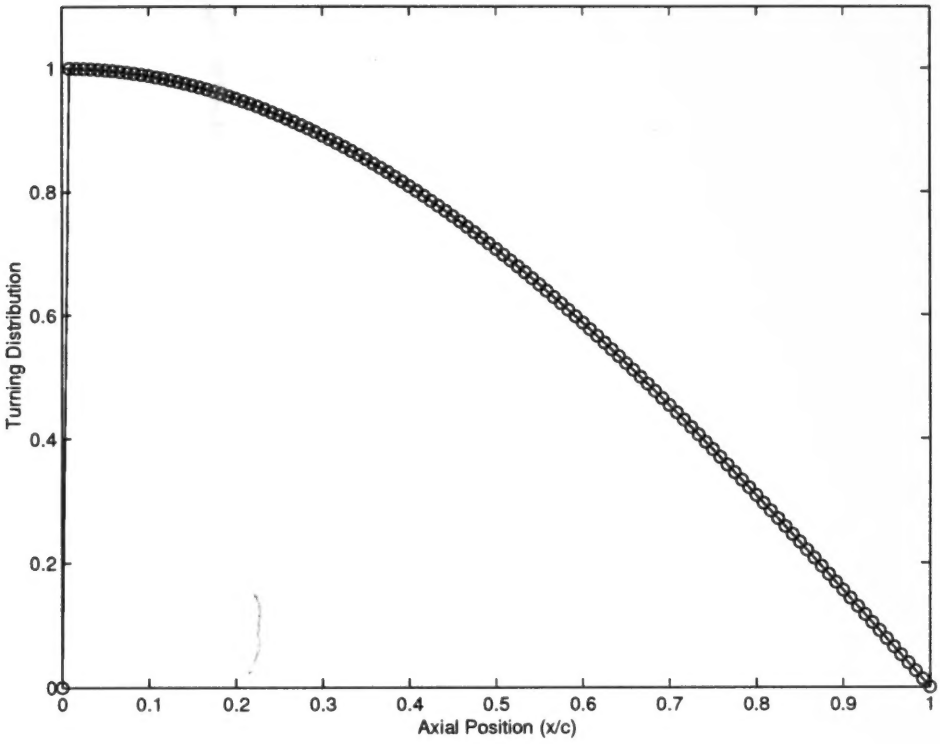

Figure 4.42: Specified Turning Distribution for the Mach 0.5 Turbine Blade

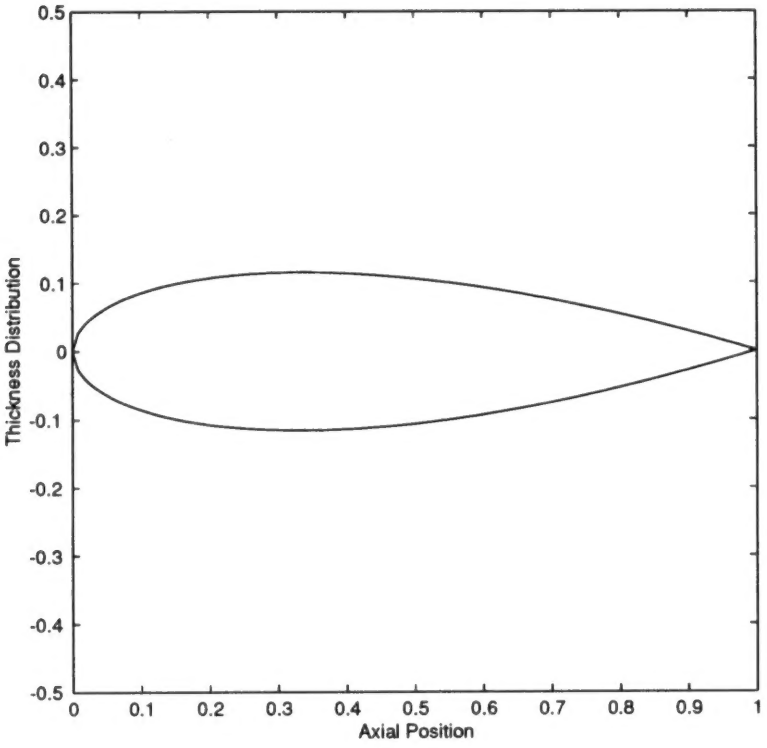

Figure 4.43: Specified Thickness Distribution for the Mach 0.5 Turbine Blade

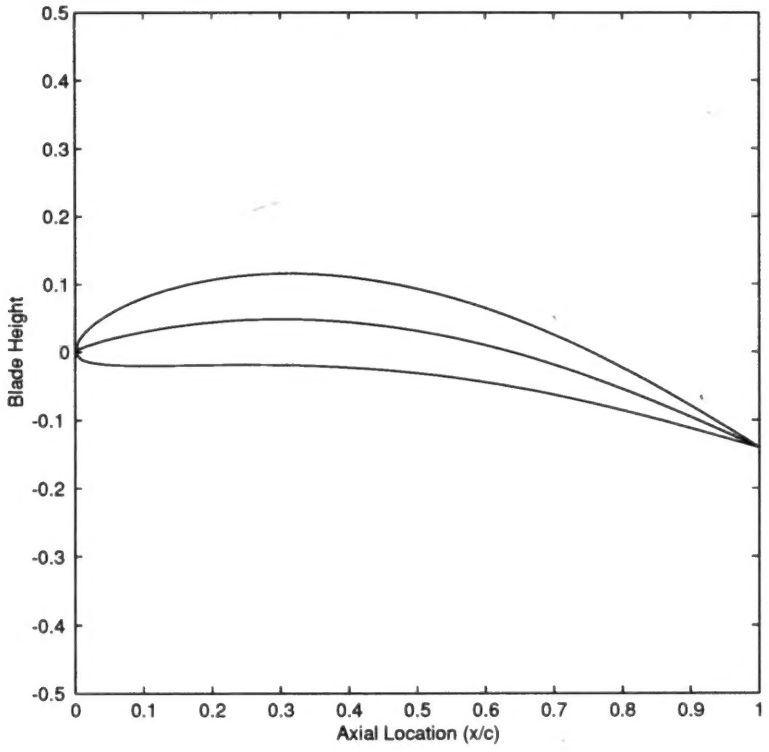

Figure 4.44: Converged Blade shape for the Mach 0.5 Turbine Blade

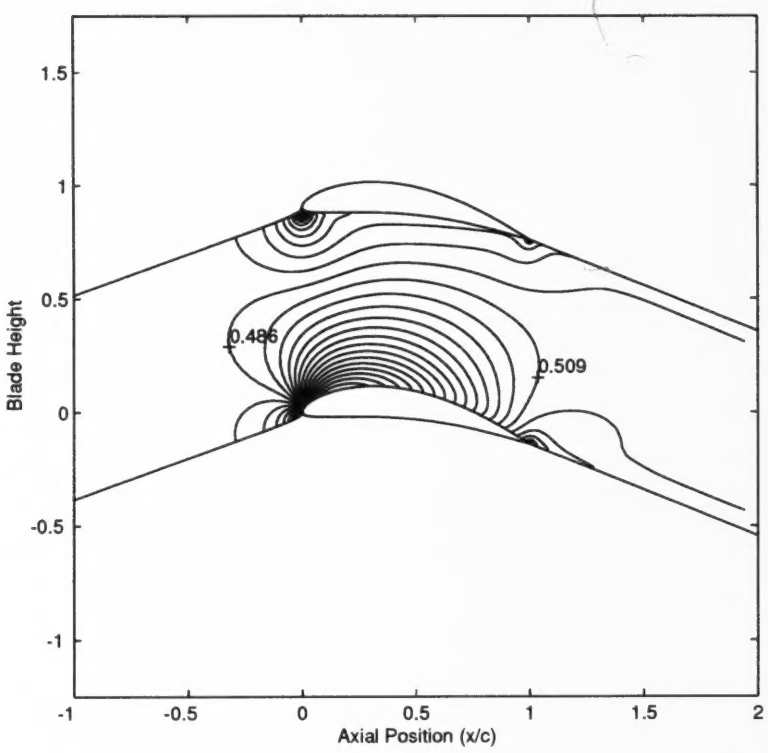

Figure 4.45: Contours of Mach Number in the Blade Passage

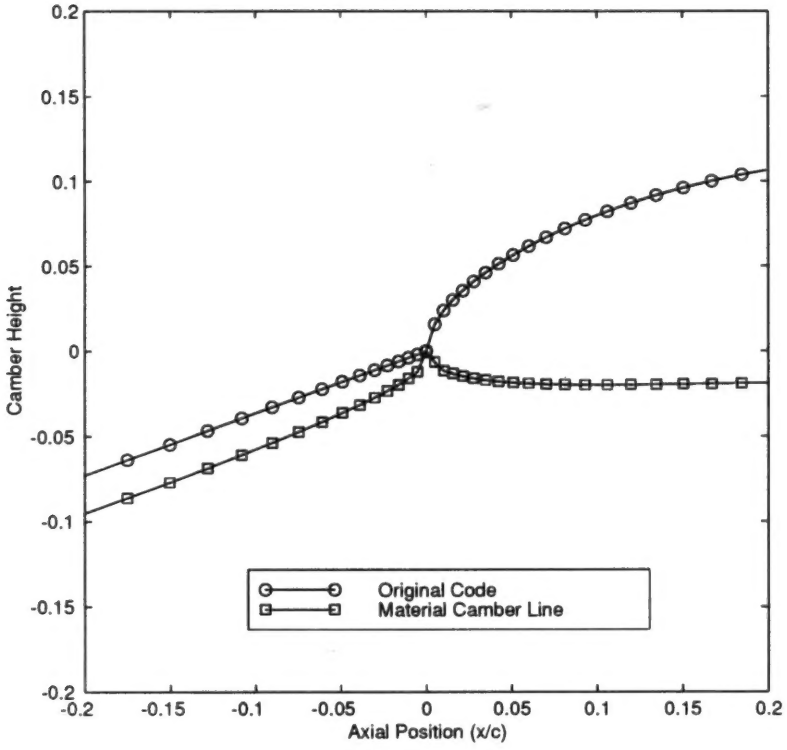

Figure 4.46: Comparison of the Upstream Grid Lines

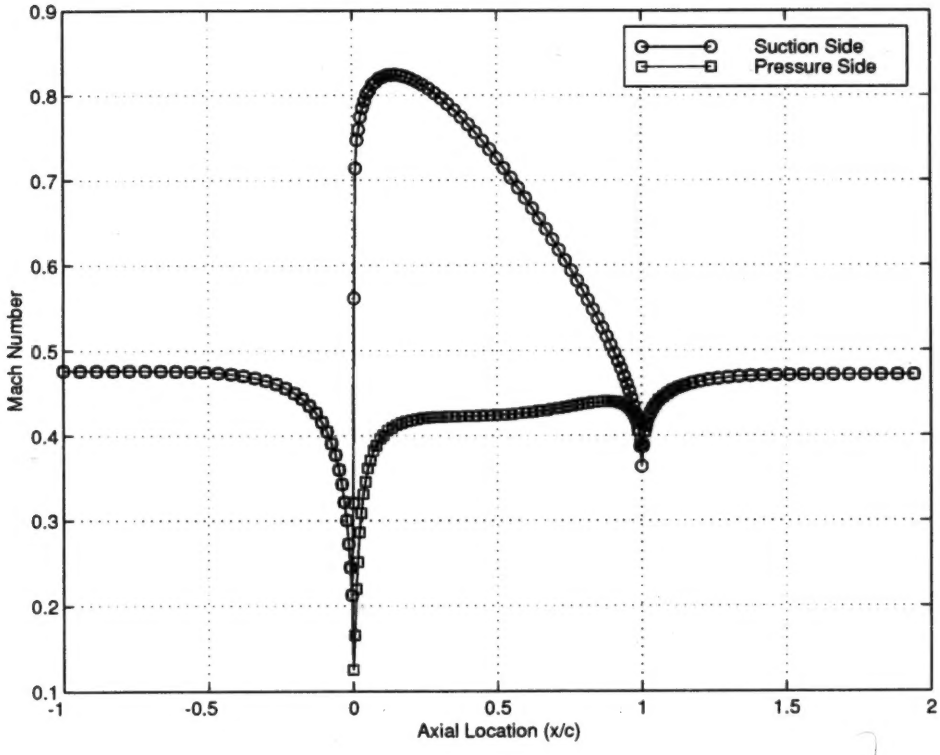

Figure 4.47: Mach Number on Blade Surfaces for the Material Camber Line

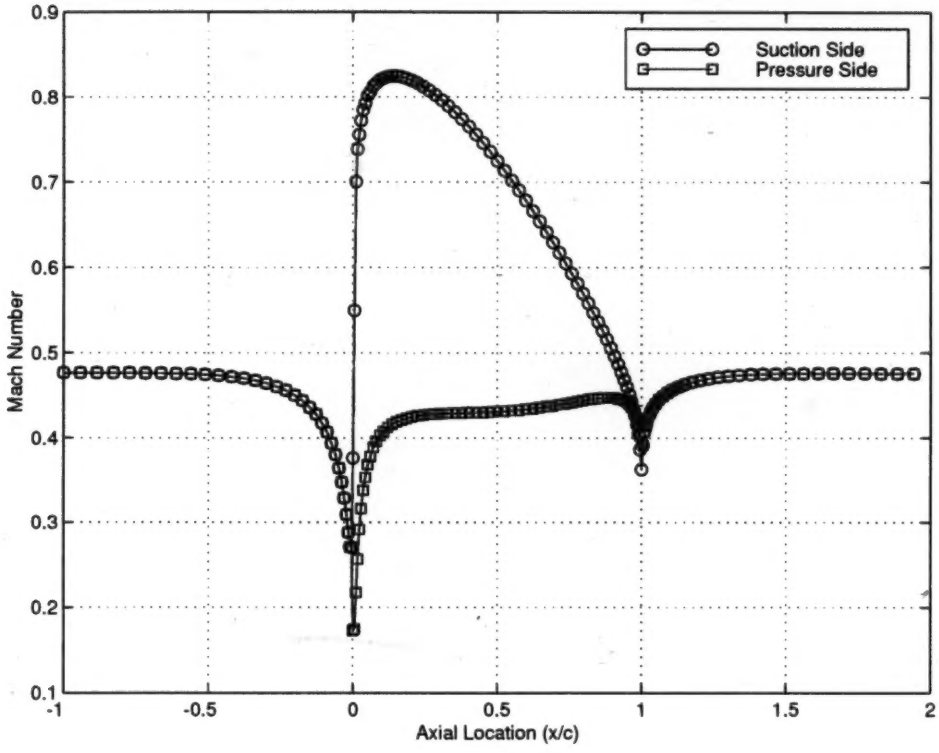

Figure 4.48: Mach Number on Blade Surfaces for the Original Camber Line

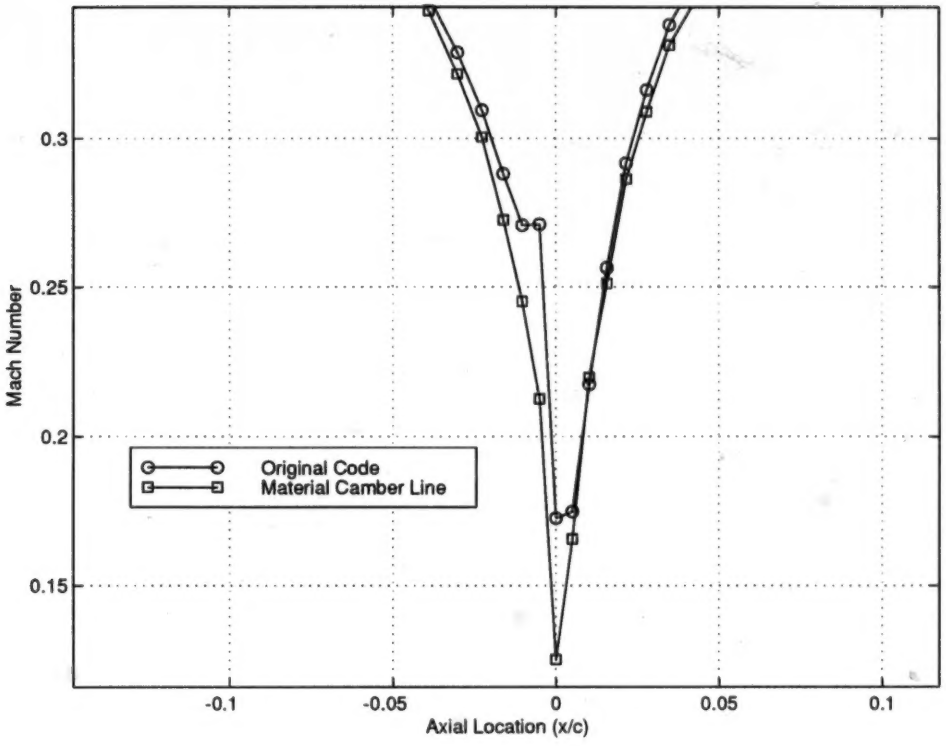

Figure 4.49: Comparison of Surface Mach Number on the Pressure Side

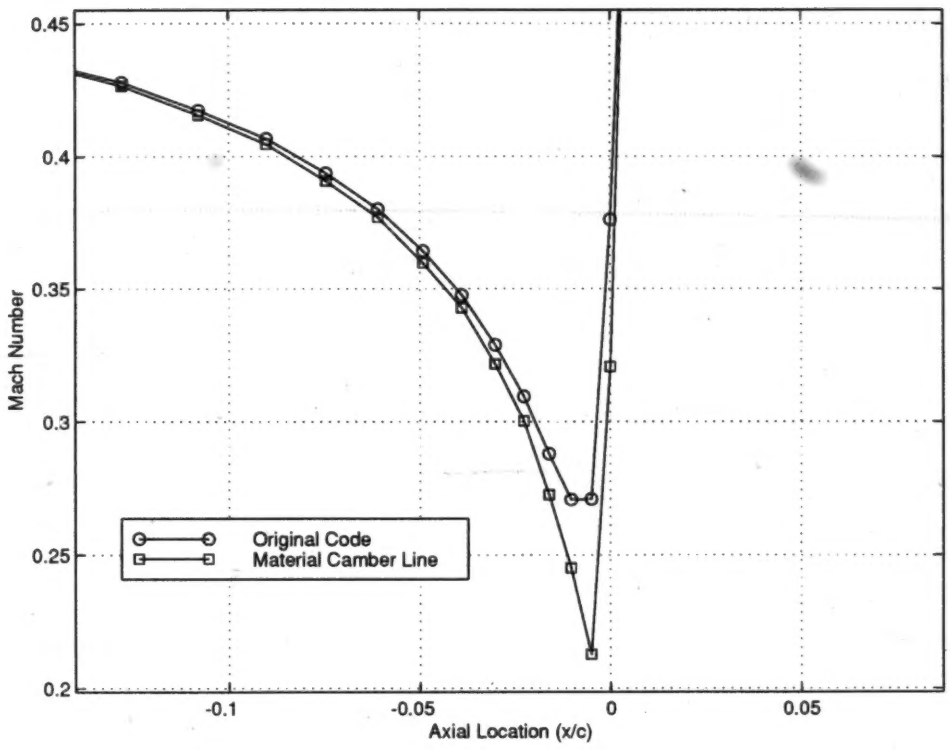

Figure 4.50: Comparison of Surface Mach Number on the Suction Side

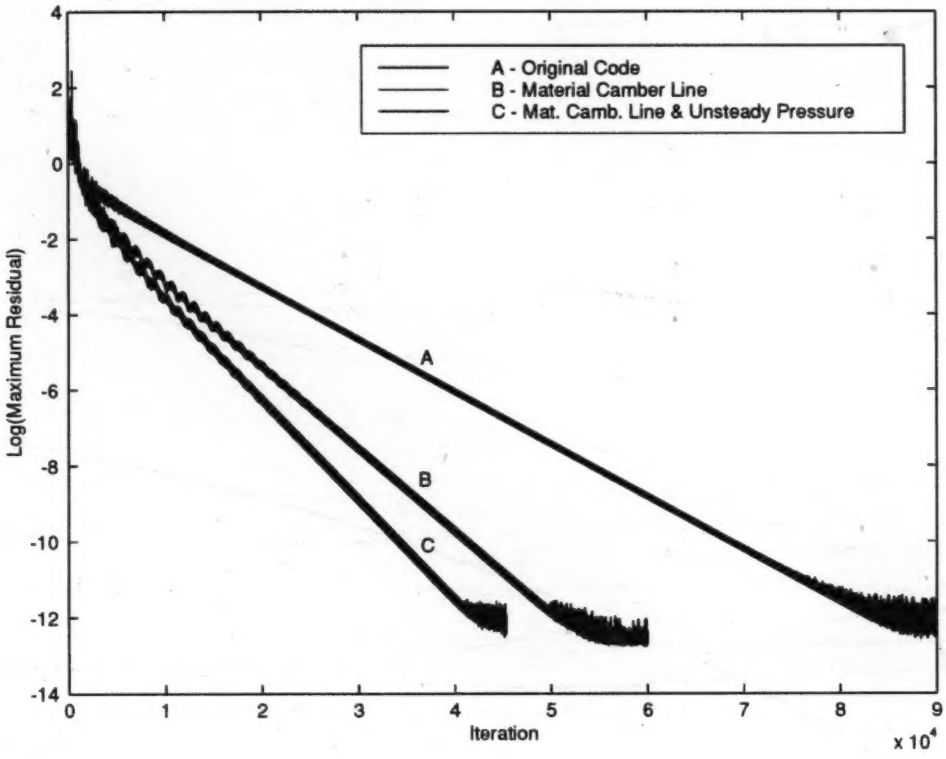

Figure 4.51: Convergence of Original and Material Camber Line Codes

4.3 Transonic Blade Design

In this next series of testcases, the use of the new transonic pressure boundary condition is shown to be effective in the design of a transonic turbine blade. With the original pressure boundary condition, having specified a continuous turning distribution, the geometry of the blade designed was discontinuous due to a strong passage shock. The result of the original method is presented first, then the option of designing the blade for the specified turning in subsonic flow and analyzing this blade in the transonic regime is presented followed by the application of the new boundary condition that is adaptive to the flow conditions which essentially specifies a discontinuous turning distribution in order to obtain a continuous blade geometry.

All test case calculations were performed on a sheared H-type mesh. The numerical domain consists of 192 X 32 cells with 128 cells in the bladed region in order to capture the shock more accurately. The domain was extended one chord upstream and downstream of the leading and trailing edges, respectively. Grid lines were clustered near the leading and trailing edges in the x-direction and near the blade surfaces in the y-direction.

4.3.1 Original Code

The transonic turbine blade was designed to produce a mass flow of $\dot{m} = .253\frac{P_o C}{\sqrt{RT_o}}$ for a specified back pressure of $P = 0.65P_o$. The spacing to chord ratio is $\frac{S}{C} = 0.55$ and the inlet flow angle is set at $\beta = 20°$. The turning distribution used is generated from $\frac{d\overline{v}}{dx} = Kcos(\frac{\pi x}{2})$, with the total turning specified as $\Delta\overline{v} = -0.783\sqrt{RT_o}$ and is shown in Fig.(4.52). A maximum thickness to spacing ratio of $\frac{T_{max}}{S} = 0.3$ is also used. This turning distribution produces the converged blade shown in Fig.(4.53) which corresponds to a total turning of 63°. The converged flow field is shown in Fig.(4.54).

Having specified the continuous turning distribution of Fig.(4.52), the blade produced from this design method is discontinuous. For an inviscid flow, as in this calculation, the actual total flow turning would be 63°, but testing of this blade in a viscous fluid, separation would most assuredly occur. The total turning would be approximately 52° with more significant losses due to the large wake produced from separation. The Mach numbers on the surface of the blade are shown in Fig.(4.55), where it can be seen that the shock hits the blade surfaces at precisely the same location due to the kink in the blade. The actual flow turning distribution produced from this blade can be seen in Fig.(4.56). For the most part the turning corresponds to the specified turning distribution except at the shock location where a large oscillation is present. This is also the location of the discontinuity in the blade.

Text resumes on page 125

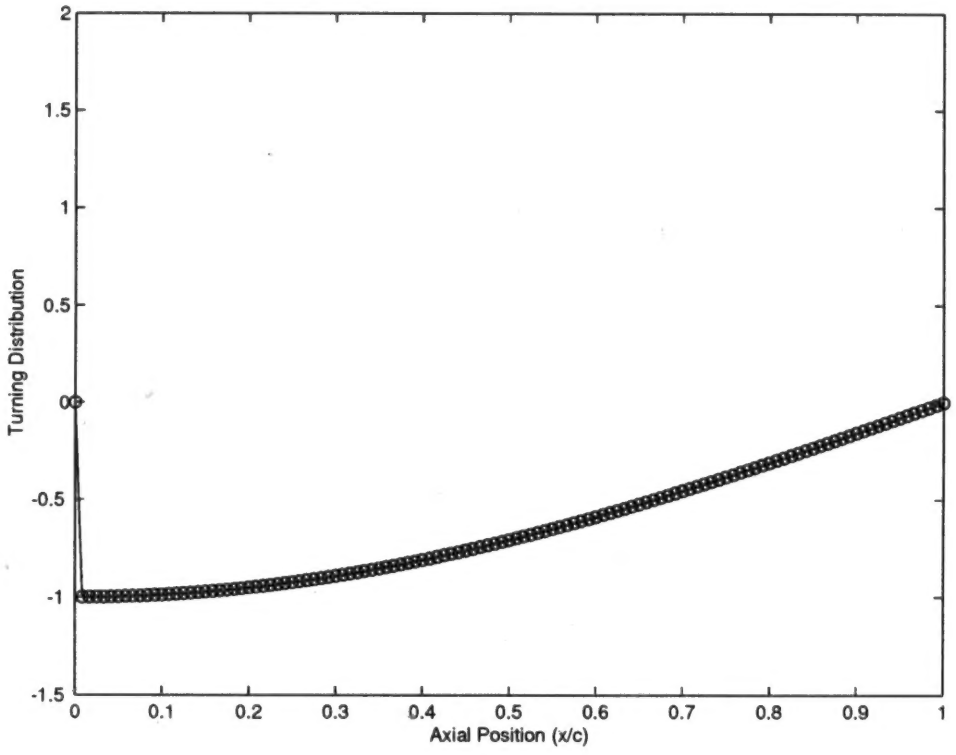

Figure 4.52: Specified Turning Distribution for the Transonic Turbine Blade

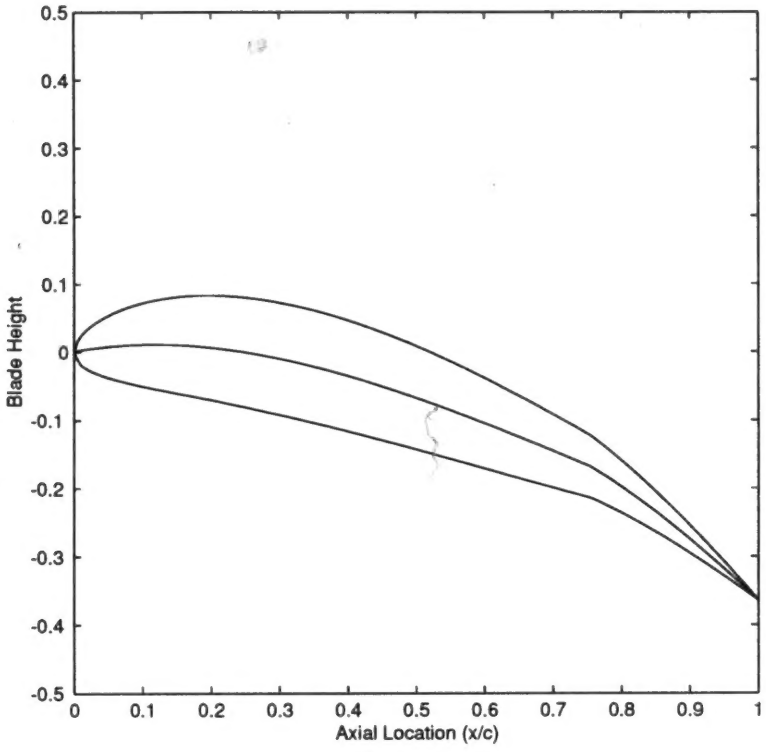

Figure 4.53: Converged Blade shape for the Transonic Turbine Blade

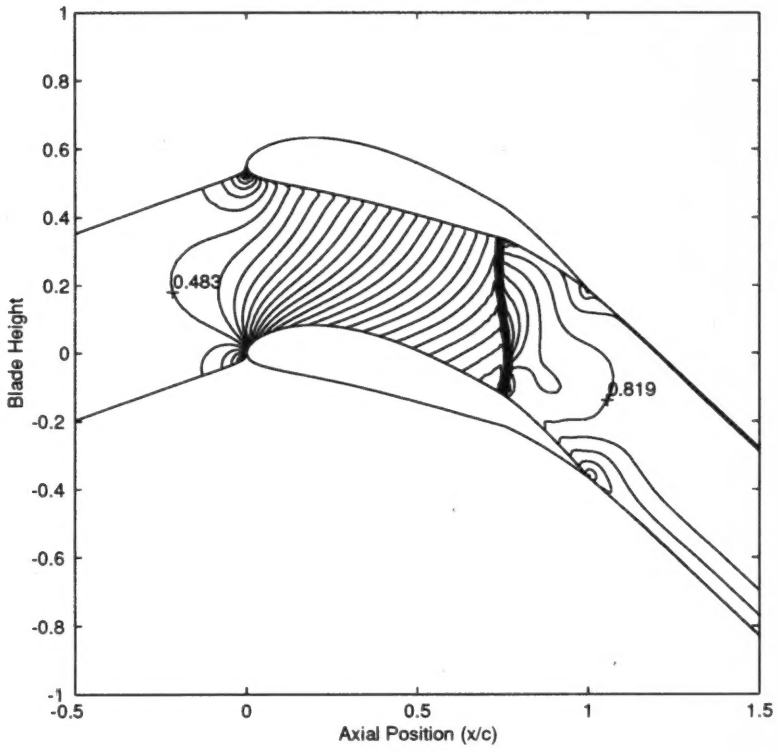

Figure 4.54: Contours of Mach Number in the Blade Passage

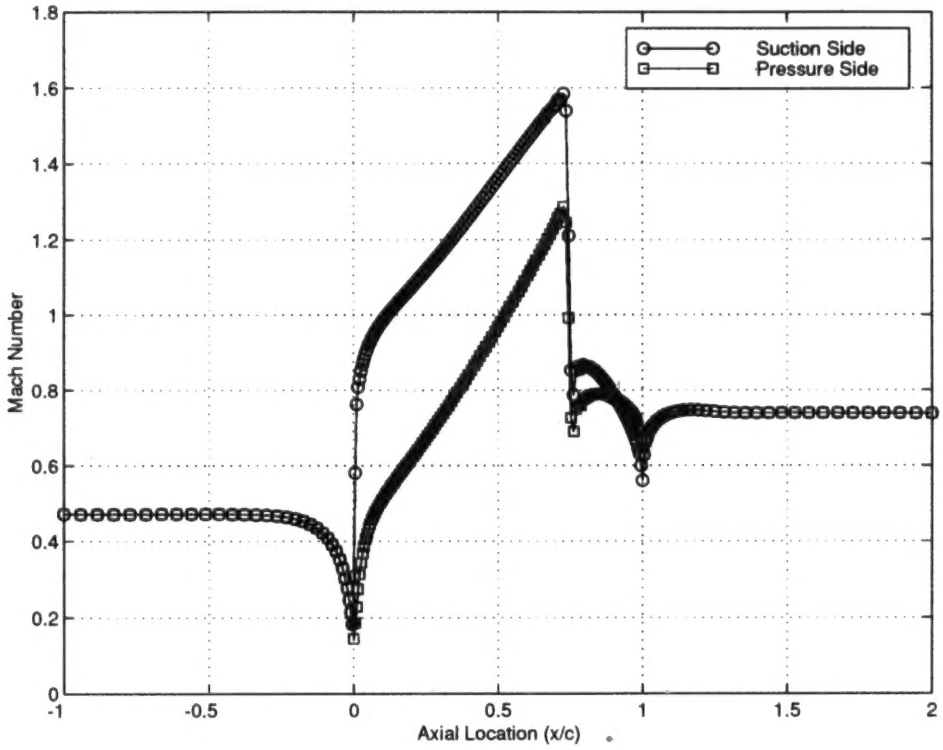

Figure 4.55: Mach Numbers on Blade Surfaces

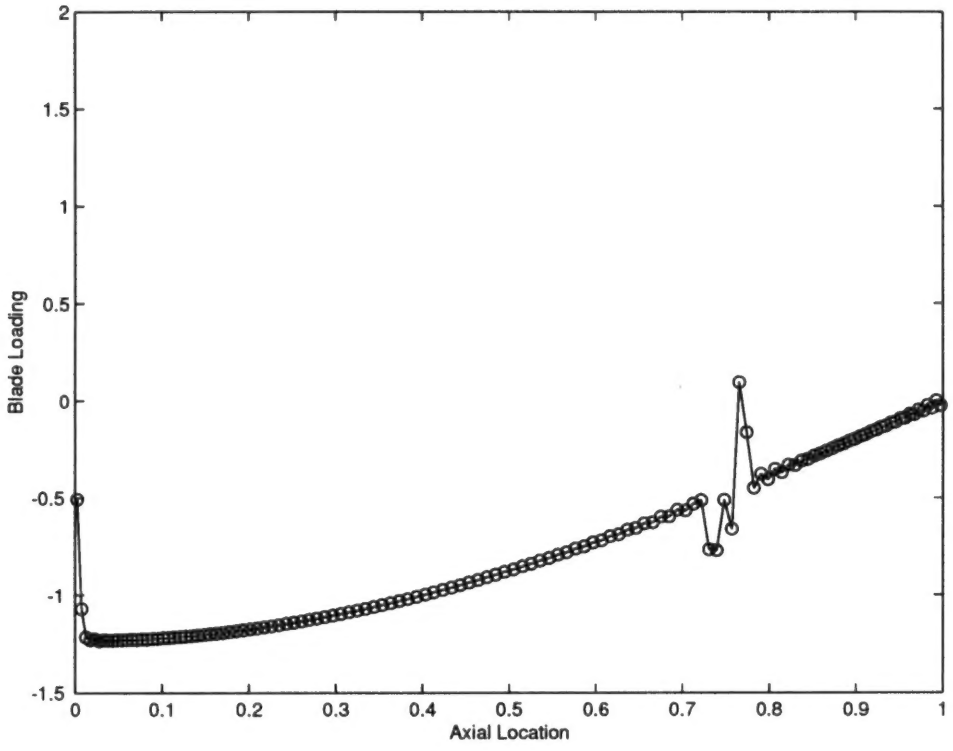

Figure 4.56: Actual Turning Distribution Generated by the Transonic Turbine Blade

4.3.2 Subsonically Designed Blade

The first option for generating a continuous blade was to raise the back pressure to $P = 0.69P_o$ in order to get a fully subsonic flow. The blade geometry is then guaranteed to be continuous. This blade profile is then analyzed in a transonic flow to produce the required flow conditions mention in the previous case. All of the specification of the previous case were used to design the blade in subsonic flow, except for the back pressure.

The converged blade can be seen in Fig.(4.57) which corresponds to a total turning of 65°. This blade was then analyzed using a back pressure of $P = 0.62P_o$ to try a match the mass flow of the previous case. The flow becomes choked and the maximum mass flow attainable from this blade is $\dot{m} = .246\frac{P_o C}{\sqrt{RT_o}}$ which is 2.8 % off the required mass flow. This choking is due to the shock that was formed in the passage seen in Fig.(4.58). The mach numbers on the blade surfaces are shown in Fig.(4.59). Along with the mass flow difficulty, there exists another problem with this design procedure: the designer has lost the control of the turning distribution. The actual turning distribution of Fig.(4.60), shows that the blade designed does not produce the required turning shape. This is a significant disadvantage in the design of turbomachine blades in that, the designer has lost control of the relation between the specified turning distribution and the one that is actually produced by the blade.

Text resumes on page 130

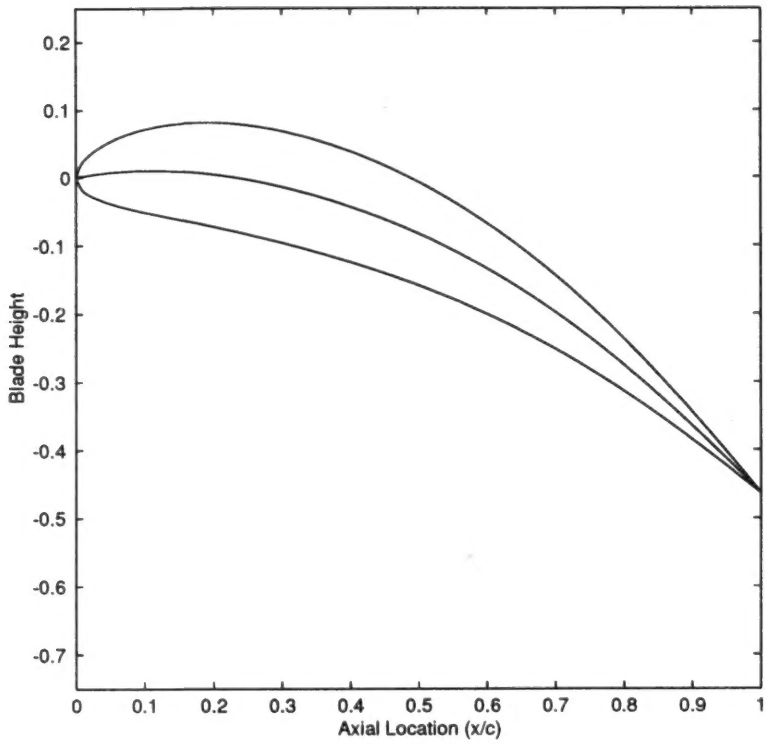

Figure 4.57: Converged Blade Generated in Subsonic Flow

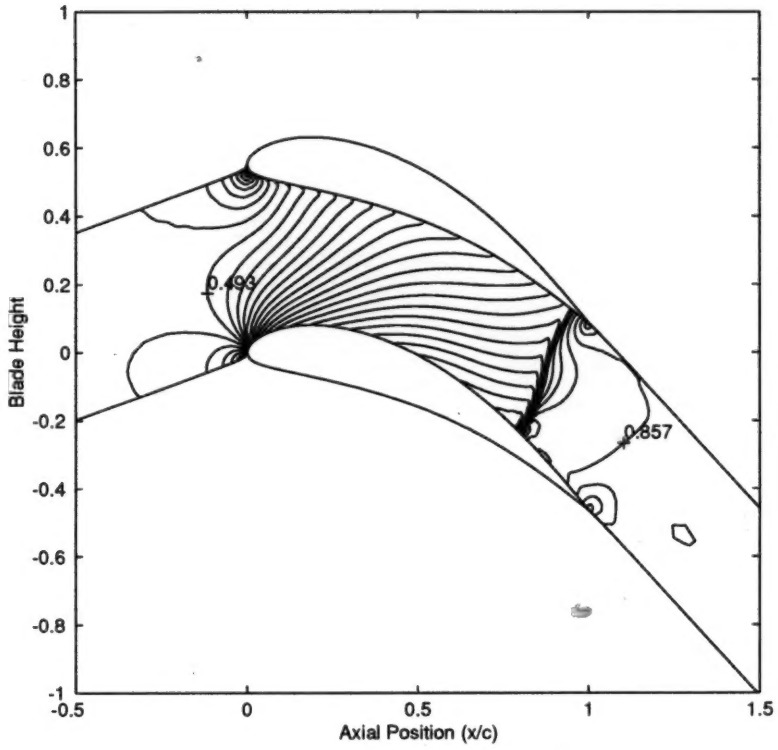

Figure 4.58: Mach Number Contours in the Blade Passage for Transonic Flow

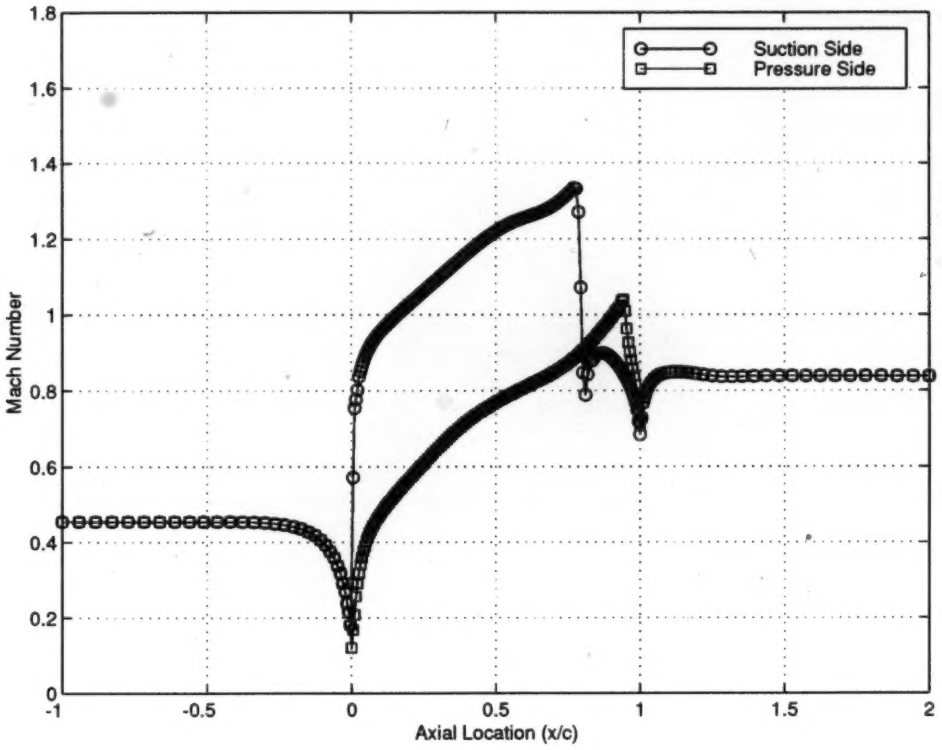

Figure 4.59: Mach Number on Blade Surfaces for the Design in Transonic Flow

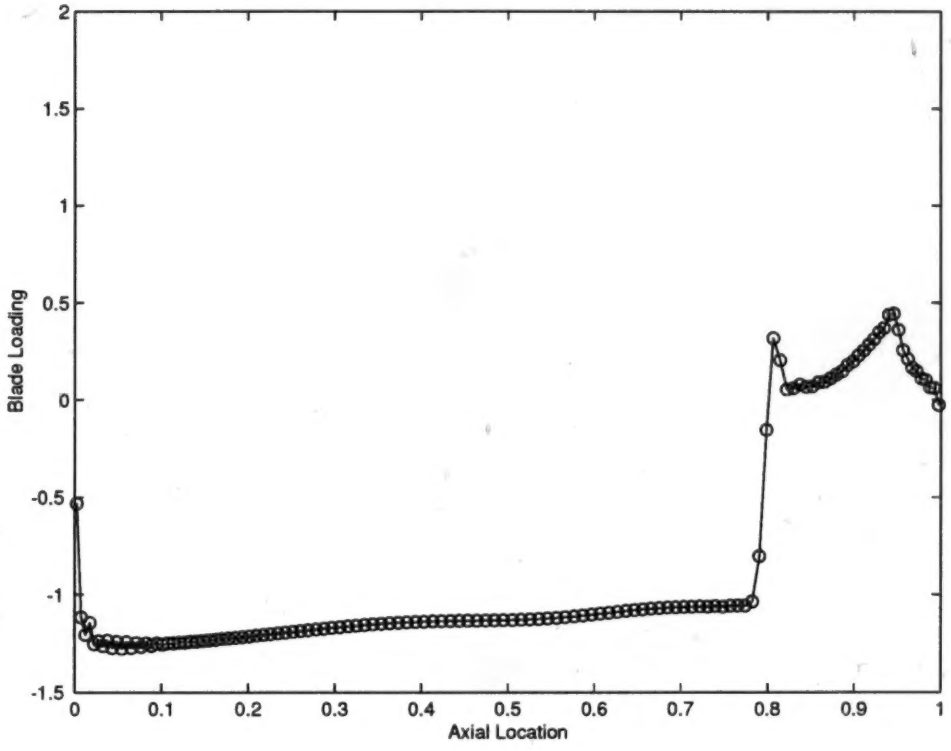

Figure 4.60: Actual Turning Distribution Generated from the Blade in Transonic Flow

4.3.3 New Treatment

With the application of the new transonic pressure boundary condition a continuous blade profile can be designed that follows the specified turning distribution. In addition to specifying the turning distribution, the constant for the modeled term must also be specified.

For this case the constant used in the model equation is chosen to be $c = 0.43$ and is applied using the Heaviside step function starting at the shock location. The combined effect of these two specifications is shown on the turning distribution in Fig.(4.61). This produces the converged, continuous blade shown in Fig.(4.62) which corresponds to a total turning of 52°. The converged flow field is shown in Fig.(4.63). The mass flow of this case matches the required mass flow of the original case, $\dot{m} = .253\frac{P_o C}{\sqrt{RT_o}}$. The total turning of this case and the original case would be approximately the same in a viscous flow. The biggest difference would be the drag losses generated from flow separation in the original case. Thus, this method would produce a blade that follows the prescribed flow turning, unlike the previous option, and have less viscous drag than the original discontinuous blade. The surface Mach numbers are shown in Fig.(4.64) where it can be seen that the passage shock is much stronger in this case. The actual turning distribution of Fig.(4.65) shows that in order to design a continuous blade with a passage shock, the turning shape must be discontinuous.

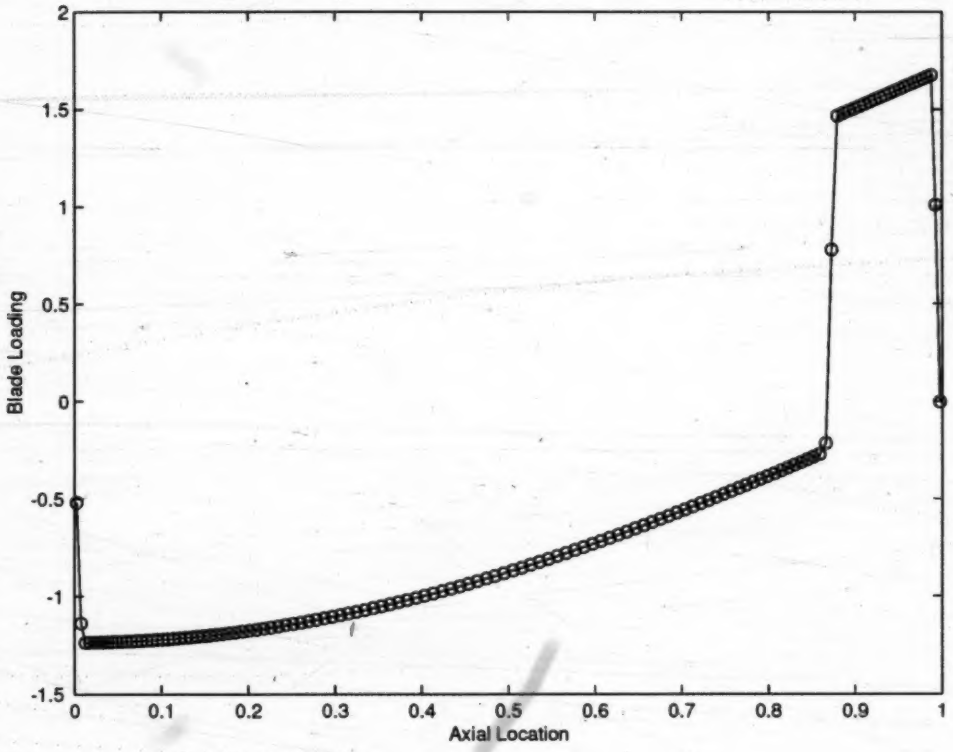

Figure 4.61: Turning Distribution Including Model of Shock Velocity Term

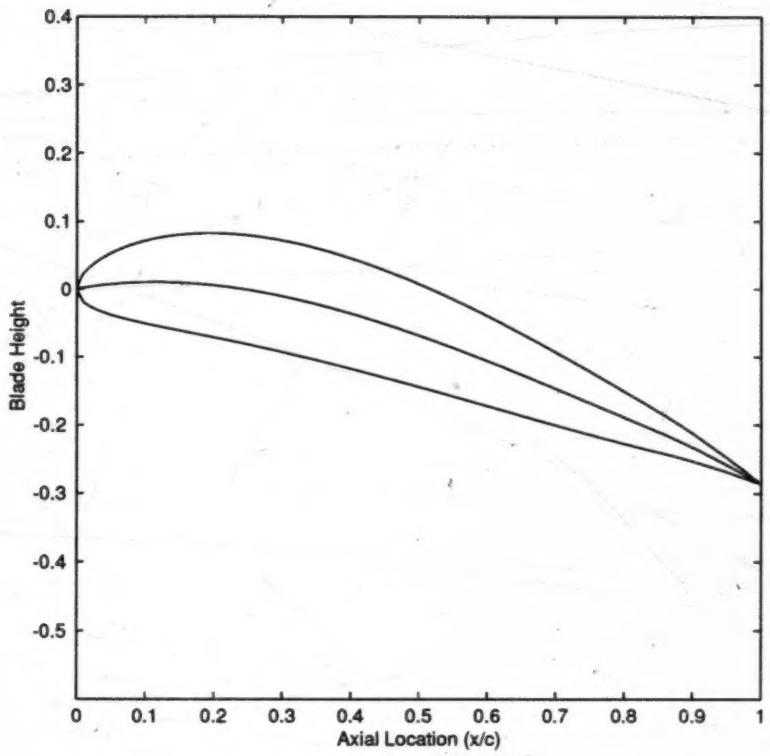

Figure 4.62: Converged Continuous Blade Shape Using Transonic Boundary Condition

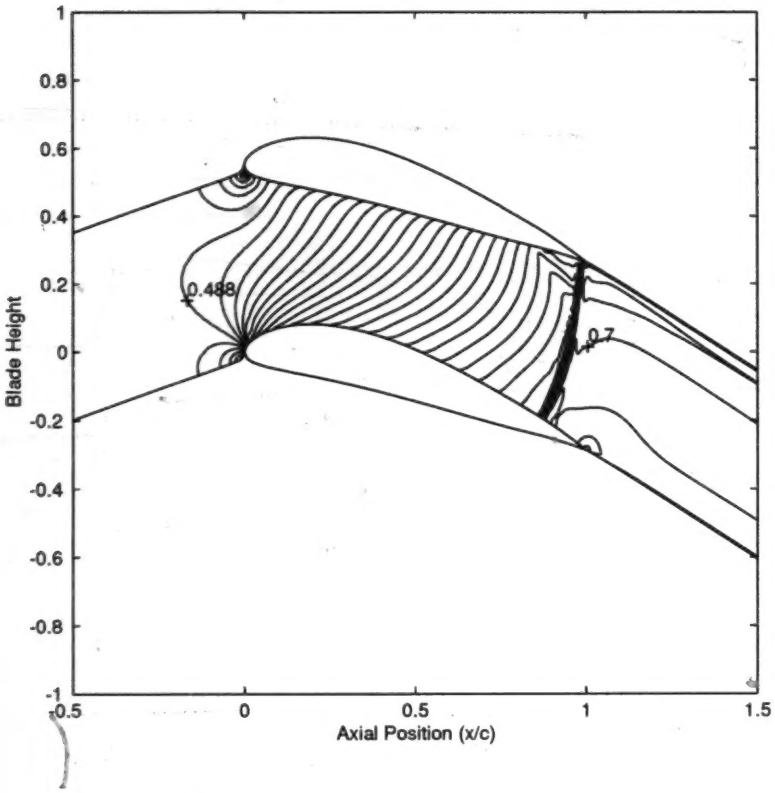

Figure 4.63: Mach Contours in the Blade Passage

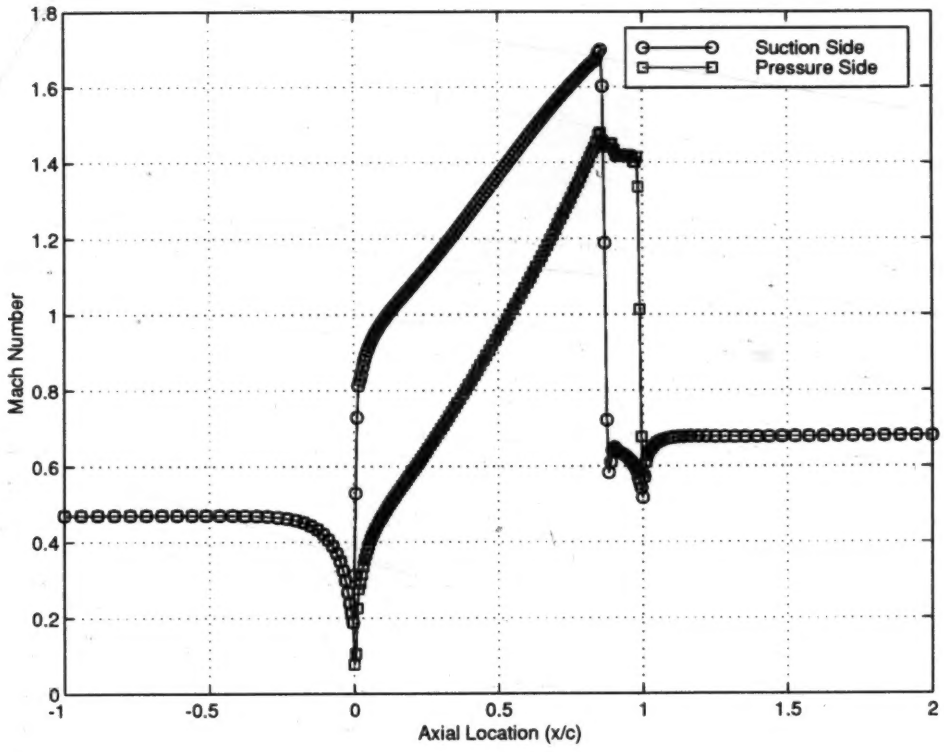

Figure 4.64: Mach Number on Blade Surfaces Using Transonic Boundary Condition

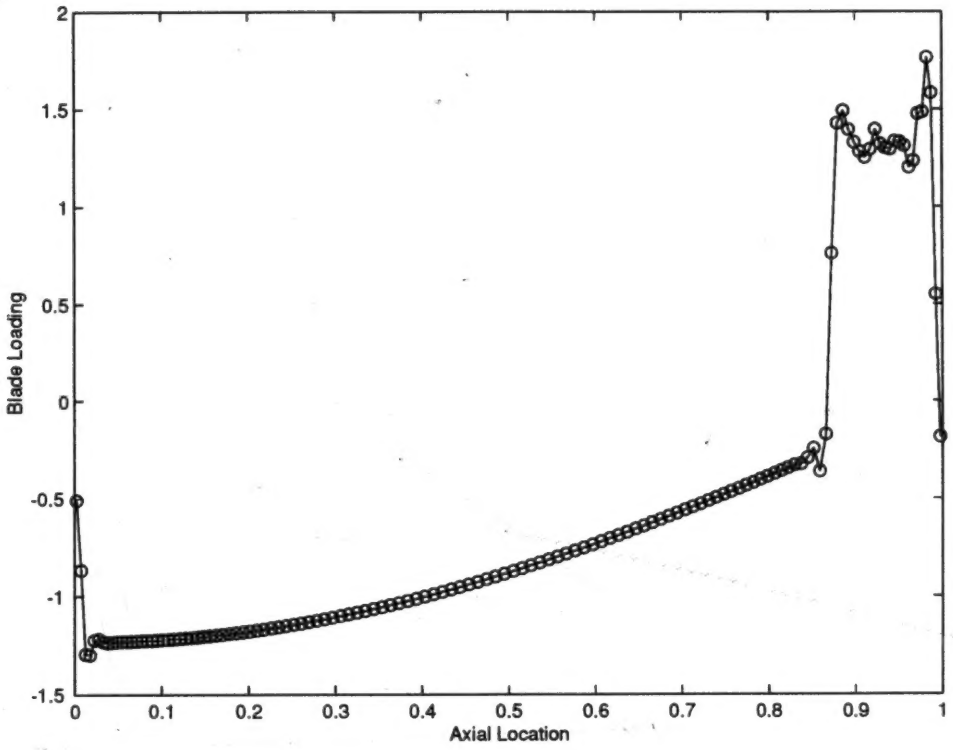

Figure 4.65: Actual Turning Distribution Generated Using Transonic Boundary Condition

Chapter 5

Conclusions

With this work, a new Lagrangian based inverse technique for constructing turbomachinery blade geometries has been presented. This method, which consists of a 2-D flow field integrator, a camber line generator and a passage averaged momentum/pressure boundary condition, generates a blade geometry in response to a prescribed flow turning distribution.

By describing a blade geometry as a mean camber line with a specified thickness distribution, it has been shown how this camber line can be obtained from a Lagrangian analysis that overlays the blade onto a material line that convects from inflow to outflow.

The first testcase presented was a blade in subsonic flow that showed a substantial difference between the straight line extrapolation method and the new material line treatment of the upstream grid line. This suggested that the stagnation point moved away of the geometrical leading edge which was indeed the case. By using the material line treatment, the convergence time was reduced to 50% of the original method and the flow field was captured more accurately at the leading edge of the blade.

The second test case was also a subsonic blade, but there was very little difference between the two upstream grid lines. This meant that the stagnation point had not moved off of the geometrical point. Since the flow was essentially coming into the

blade along the straight line, the flow field was well captured at the leading edge region. There was little improvement in the convergence rate for this case.

To show that this method was not restricted to the subsonic regime, a third testcase was presented in transonic flow. Again, it was shown that because of the differences between the upstream grid lines using the two methods, the flow field was captured more accurately at the leading edge. This testcase showed the convergence time using the material line treatment decreased to about 58% of the original method.

As a final test of the material line treatment, it was proposed that, in supersonic flow there is no upstream influence from the blade, therefore the converged upstream grid line using the material line treatment should be the same as that of the straight line extrapolation method. This is precisely what the results show. The blade geometries and the flow fields of the two methods are practically identical. The convergence times showed that the material line treatment was about 8% slower.

The next approach used, was to include the unsteady term in the pressure boundary condition. A subsonic testcase case was presented that showed two things: further support of the use of the material line treatment of the camber line and the convergence acceleration achieved using the unsteady pressure boundary condition. It was first shown that, by using the material line method alone, the convergence time was reduced to approximately 65% of the original method. Secondly, with the combination of the material line treatment of the camber line and the unsteady pressure boundary condition the convergence time was reduced to about 49% of the original treatment.

These testcases show a direct correlation between how far the stagnation point is moved away from the geometrical leading edge and the convergence acceleration that can be achieved using the material line treatment of the camber line.

Finally, a new unsteady pressure boundary condition was derived from a complex-lamellar decomposition of the flow field, and its passage average flow turning. The

need for this method was discovered when the design of certain transonic testcases was attempted. When a continuous loading distribution was specified, and a strong passage shock was present the resulting blade shape was discontinuous.

The first test case of this series showed the resulting blade shape of the original calculation. A discontinuity in the blade geometry occured at the shock location. The use of this blade in a practical application would be unrealistic because the flow would most assurdly seperate in viscous flow creating a large wake. This seperation would cause the flow to be turned less than originally specified and large viscous losses would also be present.

The next case presented is the first possible solution to eliminating the blade discontinuity. First, the back pressure is raised until the flow field is fully subsonic, the blade geometry is then obtained using the required flow turning specification. This blade is then put into the code in analysis mode where the back pressure is adjusted to match the massflow rate. A strong shock was present in the flow passage which choked the flow resulting in a massflow rate 2.8% lower than required. The entire blade row would have to be modified by increasing the spacing to chord ratio in order to match the massflow rate. The second disadvantage to using this option is that the resulting blade loading shape produced by this blade in transonic flow does not match that of the specified shape. The designer has lost the direct correlation between the input loading shape and the shape that is produced by the blade. This is a significant disadvantage in the design of turbomachinery blades.

The last case presented showed the use of the new pressure boundary condition obtained from the complex-lamellar decomposition of the flow field. In order to design a continuous blade, a discontinuous loading distribution must be specified. Without knowing the location of the discontinuity apriori there is little chance of designing a continuous blade. This method was shown to be effective by modifying the loading shape based on the development of the flow field. A continuous blade was successfully

designed by including the effects of the shock in the loading shape. The advantage this technique has over the subsonically designed method is that the designer has direct control of the loading shape obtained from the blade. The only difference occurs at the shock location. The total turning of this blade would be the same as that of the original case in viscous flow, but the flow is less likely to seperate, resulting in much lower losses.

BIBLIOGRAPHY

[1] Hawthorne, W. R., Wang, C., Tan, C. S. and McCune, J. E., "Theory of Blade Design for Large Deflections: Part 1 - Two-Dimensional Cascade,", *ASME Journal of Engineering for Gas Turbines and Power*, Vol. 106, pp. 346-353, 1984.

[2] Dang, T. Q.,"Inverse Method for Turbomachine Blades Using Shock-Capturing Techniques", AIAA Paper no. 95-2465, 1995.

[3] Dang, T. Q., "A Fully Three-Dimensional Inverse Method for Turbomachinery Blading in Transonic Flows", *ASME Journal of Turbomachinery* , Vol. 115, pp. 354-361, 1993.

[4] Dang, T. Q., "Design of Turbomachinery Blading in Transonic Flows by the Circulation Method", *ASME Journal of Turbomachinery*, Vol. 114, pp. 141-146, 1992.

[5] Tong, S. S. and Thompkins, W. T., "A Design Calculation Procedure for Shock-Free or Strong Passage Shock Turbomachinery Cascades", *ASME Journal of Engineering for Power*, Vol. 105, pp. 369-376, 1984.

[6] Giles, M. B. and Drela, M., "Two-Dimensional Transonic Aerodynamic Design Method", *AIAA Journal*, Vol. 25(9), pp. 1199-1205, 1987.

[7] Volpe, G. and Melnik, R. E., "The Design of Transonic Aerofoils by a Well - Posed Inverse Method", *International Journal for Numerical Methods in Engineering*, Vol. 22, pp. 341-361, 1986.

[8] Meauzé, G., "An Inverse Time Marching Method for the Definition of Cascade Geometry", *ASME Journal of Engineering for Power*, Vol. 104, pp. 650-656, 1982.

[9] Sanz, J. M., "Automated Design of Controlled-Diffusion Blades", *ASME Journal of Turbomachinery*, Vol. 110, pp. 540-544, 1988.

[10] Léonard, O. and Van den Braembussche, R. A., "Design Method for Subsonic and Transonic Cascade with Prescribed Mach Number Distribution", *ASME Journal of Turbomachinery*, Vol. 114, pp. 553-560, 1992.

[11] Jameson, A., Schmidt, W. and Turkel, E.,"Numerical Solution of the Euler Equations by Finite Volume Methods Using Runge-Kutta Time - Stepping Schemes", AIAA Paper 81-1259, 1981.

[12] Lakshminarayana, B., "*Fluid Dynamics and Heat Transfer of Turbomachinery*", John Wiley & Sons, Inc., 1996.

[13] Goldstein, M. E.,"*Aeroacoustics*", McGraw - Hill, Inc., 1976.

[14] Yokota, J. W.,"Vorticity Dynamics of Inviscid Shear Layers", *AIAA Journal*, Vol. 31, No.8, pp. 1430-1439, 1993.

[15] Yokota, J. W.,"A Kinematics Velocity Decomposition of Stratified Flow", *International Journal of Computational Fluid Dynamics*, Vol.9, pp.121-135, 1998.

[16] Yokota, J. W.,"Potential/Complex-Lamellar Descriptions of Incompressible Viscous Flow", *Physics of Fluids*, Vol.9, No.8, pp. 2264-2272, 1997.